Fakultät für Mathematik, Informatik und Naturwissenschaften | RWTH AACHEN UNIVERSITY

Swelling and association kinetics of linear PNIPAM-based polymers at the phase transition

Von der Fakultät für Mathematik, Informatik und Naturwissenschaften der RWTH Aachen University zur Erlangung des akademischen Grades einer Doktorin der Naturwissenschaften genehmigte Dissertation

Vorgelegt von

Joanna Michalska-Walkowiak, M. Sc.

aus

Sieradz, Poland

Berichter*:* *Professor Dr. Stephan Förster*

Universitätsprofessor Dr. rer. nat. Joachim Mayer

Tag der mündlichen Prüfung*:* *26.10.2022*

Diese Dissertation ist auf den Internetseiten der Universitätsbibliothek verfügbar.

This project was supervised under the scientific direction of Prof. Dr. Stephan Förster. The experimental work was performed from September 2017 to December 2021 at the Jülich Centre for Neutron Science, Neutron Scattering and Softmatter (JCNS-1/IBI-8) in Forschungszentrum Jülich GmbH in Prof. Dr. Stephan Förster group. The project was part of collaboration within the DFG-funded Collaborative Research Centre SFB 985 “Functional Microgels and Microgel Systems”.

Authors contribution

Parts of this thesis have been published. Parts of this thesis have been done with cooperation of others.

I synthesized and characterized the polymers and Jürgen Allgaier was involved into this part. I characterized the polymer samples.

Beate Förster and I planned, prepared, performed, and analyzed the cryo-TEM imaging.

Martin Dulle performed the SAXS experiments, I analyzed the data.

I prepared the samples and analyzed the data for SANS experiments. Martin Dulle, Vitaliy Pipich, Henrich Frielinghaus and I planned and performed the tr-SANS with stopped-flow device for temperature jump experiment. Christina Papadakis, Leonardo Chiappisi and I planned and Christina Papadakis, Leonardo Chiappisi, Pablo Alvarez Herrera, Feifei Zheng, Johannes Allwang and I performed the SANS experiments with pressure change. I analyzed the data with Martin Dulle contribution.

I prepared the samples. Igor Chizhov, Stephan Hauschild and Stephan Förster performed the Raman laser experiments. Igor Chizhov, Stephan Hauschild and I performed the Raman-thulium laser experiments. I analyzed the data.

Stephan Hauschild and I planned, performed, and developed the analysis routine for thulium laser experiments with Stephan Förster contribution.

Martin Dulle, Stephan Hauschild and Stephan Förster contributed to the scientific discussions.

The bistability and memory function section is part of the published article:
Joanna Michalska-Walkowiak[a,b], Beate Förster[c], Stephan Hauschild[a], Stephan Förster[a,b], *Bistability, Remanence, Read/write-memory and Logic Gate Function via A Stimuli Responsive Polymer*. Adv. Mater. 2108833 (**2022**).

[a] JCNS-1/IBI-8, Forschungszentrum Jülich, 52425 Jülich, Germany
[b] Institute of Physical Chemistry, RWTH Aachen University, 52074 Aachen, Germany
[c] ER-C-1, Forschungszentrum Jülich, 52425 Jülich, Germany

Abstract

Stimuli-responsive polymer systems are intensely investigated for applications in biotechnology and medicine. Temperature and pressure are among the most important regulative parameters for responsive polymers. The most significant responsiveness occurs at the volume phase transitions of polymers exhibiting a lower (LCST) or upper (UCST) critical solution temperature. Stimuli-responsive polymers offer the possibility to systematically vary chemical structure and functionality, shape, internal architecture, and crosslinking density to design the response and its kinetics. Despite its importance, there is still a lack of fundamental knowledge about polymer volume phase transition kinetics.

In the present thesis, the phase transition was examined with linear PNIPAM polymers and PS-*b*-PNIPAM block copolymers to check the influence of morphology and polymer length on the phase transition mechanism. The response of the polymers was studied in detail by light, neutron, and X-ray scattering, transmission electron microscopy, and optical transmittance, where important complementary information could be obtained about the complex behavior across the LCST. An abrupt and sharp phase transition was observed for the examined polymers, with an intrinsic hysteresis window between swollen and aggregated particles. It could be demonstrated that switching between states allows writing, reading, and storing information in polymer solutions within the hysteresis temperature range. Moreover, bistability, remanence and reversible information storage were realized. Information can be written on a thin layer backscattering device by cooled or heated metal pen tips as well as by a laser pulse. The bistability in PNIPAM-based polymers can be controlled by temperature and by pH as well, providing an AND-logic gate function. The demonstrated information encoding and storage properties for simple linear PNIPAM polymers provide new insight into responsive materials' application.

The kinetics of the phase transition for PNIPAM-based polymers over a broad time scale was investigated using two experimental methods, where the transition was induced by a rapid temperature jump above LCST. One of them is time-resolved small-angle neutron scattering with a stopped-flow device, which tracks the size evolution of the polymers. The temperature jump can be induced on the time scale from milliseconds to minutes, where the early stage of cluster formation is observed, with further aggregation of the clusters. A multi-step aggregation was observed with the variation of polymer concentration. The second method allows following changes of turbidity within nanoseconds, where the temperature jump was induced by NIR-laser pulses. The transition mechanism for heating and cooling processes is described, from microseconds to minutes. The solution was rapidly heated or heated and kept for a few seconds above LCST to distinguish the differences in kinetics mechanism. The responsiveness of polymers with different morphology shows a lot of similarities. However, within the same polymeric

system, a change of the polymer chain end-group leads to differences in the swelling process. Every step on the kinetics mechanism can be described by a characteristic time, thus that the rate constant of every process can be determined. The used methods in this thesis enable to distinguish the contributions from collapse/swelling transitions, aggregation/swelling, and phase separation/mixing processes during the volume phase transition.

Within the hysteresis temperature range, deep and shallow temperature jumps were performed for linear PNIPAM-based polymers. The conditions at which the bistable state can be kept for a long time and the minimum heating energy needed to complete the microphase separation were determined using laser pulse heating. In addition, experimental methods consisting of NIR-laser setups and a high-speed camera, allow observation of the stability of aggregates state at the heated spot and verifying a thermal diffusion distance in the polymer solution.

Kurzzusammenfassung

Stimuli-responsive Polymersysteme werden intensiv für Anwendungen in Biotechnologie und Medizin untersucht. Temperatur und Druck gehören zu den wichtigsten Regelparametern für responsive Polymere. Die signifikanteste Ansprechempfindlichkeit tritt bei den Volumenphasenübergängen von Polymeren auf, die eine untere (LCST) oder obere kritische Lösungstemperatur (UCST) aufweisen. Stimuli-responsive Polymere bieten die Möglichkeit, die chemische Struktur und Funktionalität, Form, innere Architektur und Vernetzungsdichte systematisch zu variieren, um die Reaktion und ihre Kinetik zu gestalten. Trotz ihrer Bedeutung mangelt es noch an grundlegendem Wissen über die Kinetik des Volumenphasenübergangs von Polymeren.

Der Phasenübergang wurde mit linearen PNIPAM-Polymeren und PS-b-PNIPAM-Block-Copolymeren untersucht, um den Einfluss von Morphologie und Polymerlänge auf den Phasenübergangsmechanismus zu überprüfen. Die Reaktionsfähigkeit von Polymeren wurde im Detail unter Verwendung von Licht-, Neutronen- und Röntgenstreuung, Transmissionselektronenmikroskopie und optischer Transmission untersucht, wobei wichtige ergänzende Informationen über das komplexe Verhalten über LCST erhalten wurden. Ein abrupter und scharfer Phasenübergang wurde für die untersuchten Polymere beobachtet, mit einer Hysterese zwischen gequollenen und aggregierten Partikeln. Es konnte gezeigt werden, dass das Umschalten zwischen beiden Zuständen das Schreiben, Lesen und Speichern von Informationen in der Polymerlösung innerhalb des Hysterese-Temperaturbereichs ermöglicht. Darüber hinaus wurden Bistabilität, Remanenz und reversible Informationsspeicherung ermöglicht. Mittels eines Dünnschicht-Rückstreu-Aufbaus können Informationen sowohl mit einer gekühlten oder erhitzten Metallstiftspitze, als auch mit einem Laserstrahl geschrieben werden. Die Bistabilität in Polymeren auf PNIPAM-Basis kann durch die Temperatur und auch durch den pH-Wert gesteuert werden, wodurch eine UND-Logikgatterfunktion realisiert werden kann.. Informationskodierungs- und Speichereigenschaften für einfache lineare PNIPAM-Polymere geben einen neuen Einblick in mögliche Anwendung von responsiven Materialien geben.

Die Kinetik des Phasenübergangs für PNIPAM-basierte Polymere in einer breiten Zeitskala wurde durch zwei experimentelle Methoden verfolgt, bei denen der Übergang durch einen schnellen Temperatursprung über die LCST induziert wurde. Eine davon ist die zeitaufgelöste Kleinwinkel-Neutronenstreuung mit Stopped-Flow-Gerät, bei der es möglich ist, die Größenentwicklung zu verfolgen. Der Temperatursprung kann in der Zeitskala von Millisekunden bis Minuten induziert werden und das frühe Stadium der Clusterbildung mit weiterer Aggregation der Cluster beobachtet werden. Bei der Variation der Polymerkonzentration konnte eine mehrstufige Aggregation unterschieden werden. Die zweite Methode ermöglicht es, Trübungsänderungen innerhalb von Nanosekunden zu

verfolgen. Die Temperatursprünge wurden durch NIR-Laserpulse induziert. Der Übergangsmechanismus für Erwärmungs- und Abkühlungsvorgänge wird beschrieben, von Mikrosekunden bis zu Minuten. Die Lösung wurde schnell erhitzt, oder erhitzt und einige Sekunden über LCST gehalten, um die Unterschiede im kinetischen Mechanismus zu untersuchen. Das Ansprechverhalten von Polymeren mit unterschiedlicher Morphologie weist viele Ähnlichkeiten auf. Innerhalb des gleichen Polymersystems führt jedoch die Änderung der Endgruppe in der Polymerkette zu Änderungen im Quellprozess. Jeder Schritt des kinetischen Mechanismus wird durch eine charakteristische Zeit beschrieben, so dass die Geschwindigkeitskonstante jedes Prozesses bestimmt werden kann. Die in dieser Arbeit verwendeten Methoden ermöglichen es, die Beiträge von Kollaps-/Quellübergängen, Aggregation/Quellung und Phasentrennungs-/Mischprozessen während des Volumenphasenübergangs zu unterscheiden.

Im Hysteresetemperaturbereich wurden unterschiedlich große Temperatursprünge in den Zweiphasenbereich für lineare Polymere auf PNIPAM-Basis durchgeführt. Die Bedingungen, bei denen der bistabile Zustand für eine lange Zeit gehalten werden kann, und die minimale Heizenergie, die benötigt wird, um die Mikrophasentrennung zu vervollständigen, wurden unter Verwendung von Laserimpulsheizung bestimmt. Darüber hinaus ermöglichen experimentelle Methoden, bestehend aus NIR-Laseraufbauten und einer Hochgeschwindigkeitskamera, die Beobachtung der Stabilität des Aggregatzustands an der erhitzten Stelle und den Nachweis einer thermischen Diffusionsstrecke in der Polymerlösung.

Table of contest

AUTHORS CONTRIBUTION IV

LIST OF ABBREVIATIONS: XIV

1. INTRODUCTION 1

2. FUNDAMENTALS AND THEORY 3

2.1. THE CARRIER SYSTEM 3
2.1.1. Introduction to Stimuli-Sensitive polymers 3
2.1.2. Thermo-responsive polymers 3
2.1.3. Cloud point temperature 5
2.1.4. Phase separation 6
2.1.5. Hysteresis 6
2.1.6. Polymer solution 7
2.1.7. Diffusion-limited polymer aggregation 8
2.2. POLY(*N*-ISOPROPYLACRYLAMIDE) 11
2.2.1. PNIPAM-based copolymers 12
2.2.2. Micellization 12
2.3. STUDY OF THE MORPHOLOGY CHANGES ACROSS LCST OF RESPONSIVE POLYMERS 15
2.3.1. Small angle scattering 15
2.3.2. Transmission electron Microscopy 28

3. RESULTS AND DISCUSSION 31

3.1. SYNTHESIS AND CHARACTERIZATION OF PNIPAM POLYMERS 31
3.1.1. Synthesis 31
3.1.2. Polymer characterization 33
3.1.3. Sample preparation 34
3.2. VOLUME PHASE TRANSITION 34
3.2.1. Turbidity 34
3.2.2. Hydrodynamic radius 35
3.2.3. Polymer morphologies below and above the LCST 38
3.3. BISTABILITY AND MEMORY FUNCTION 40
3.3.1. Hysteresis loop 40
3.3.2. Bistability 41
3.3.3. Cluster formation and swelling 42
3.3.4. Locally induced phase transition 45
3.3.5. Non-erasable memory 49
3.3.6. AND logic gate function 51
3.4. RESPONSIVENESS MONITORING FOR TEMPERATURE AND PRESSURE OF PNIPAM-SHELL IN THE MICELLES 53
3.4.1. PS-core size determination 53
3.4.2. PNIPAM-shell shrinking and cluster formation upon heating 54
3.4.3. Cluster swelling/deswelling upon pressure change 58
3.5. KINETICS OF THE PNIPAM-SHELL SHRINKAGE AND CLUSTER AGGREGATION AT THE TEMPERATURE JUMP 66
3.5.1. Effect of the concentration on the cluster formation 66

3.6. MECHANISM OF THE PHASE TRANSITION ACROSS LCST FOR PNIPAM-BASED LINEAR POLYMERS TRACE BY OPTICAL TRANSMISSION CHANGE 73
3.6.1. Fast temperature jump induced by NIR-laser setup 73
3.6.2. Temperature jumps in hysteresis temperature range 85

4. SUMMARY AND OUTLOOK 94

5. MATERIALS AND EXPERIMENTAL PROCEDURES 99

5.1. MATERIALS 99
5.2. SYNTHESIS OF THE POLYMERS 99
5.2.1. Synthesis of Polystyrene (PS) core 100
5.2.2. Synthesis of Poly(N-isopropylacrylamide) (PNIPAM) shell 101
5.2.3. End group modification in block copolymer PS-b-PNIPAM-C_{12} 102
5.2.4. Synthesis of Poly(N-isopropylacryl amide) (PNIPAM) homopolymer 104
5.3. SAMPLE PREPARATION 106
5.4. CHARACTERIZATION OF THE POLYMERS 106
5.4.1. Nuclear magnetic resonance (NMR) 106
5.4.2. Size Exclusion Chromatography (SEC) 106
5.4.3. Turbidity measurement 107
5.4.4. Dynamic light scattering (DLS) 107
5.4.5. Cryogenic Transmission electron microscopy (cryo-TEM) 108
5.5. STRUCTURAL CHANGES ACROSS LCST 109
5.5.1. Small-angle X-ray scattering 109
5.5.2. Small-angle neutron scattering 109
5.5.3. Fast temperature jump induced by Raman/Thulium laser setup 112
5.5.4. Temperature jump induced by Thulium laser setup 113

LIST OF TABLES 115

LIST OF FIGURES 116

BIBLIOGRAPHY: 124

ACKNOWLEDGEMENTS 136

CURRICULUM VITAE 138

DECLARATION OF AUTHORSHIP 139

List of abbreviations:

AIBN	2,2'-Azobis(2-methylpropionitrile)
Atm.p.	Atmospheric pressure
BA	n-Butyl acrylate
CCD	Charge coupled device
CMC	critical micelle concentration
CPDT	2-cyano-2-propyl dodecyl trithocarbonate
cryo	Cryogenic
CTA	Chain transfer agent
DDMAT	2-dodecylthiocarbonothoylthio)-2-methylpropionic acid
DLCA	Diffusion-limited colloid aggregation
DLS	Dynamic
EM	Electron microscopy
FTIR	Fourier-transform infrared spectroscopy
GPC	gel permeation chromatography
H	Magnetic field strength
H-bond	Hydrogen bond
HS	Hard sphere
HSC	High-speed camera
ILL	Institut Laue-Langevin
KWW	Kohlrausch-Williams-Watts
LCST	Lower critical solution temperature
M	magnetization
MLZ	Heinz Maier-Leibnitz Zentrum
NIPAM	*N*-isopropyl acrylamide
NIR	Near infrared
NMR	nuclear magnetic resonance
OD	Optical transition
OZ	Ornstein-Zernike
PDI	molecular weight distribution
PNIPAM	poly(*N*-isopropyl acrylamide)
PS-b-PNIPAM-BA	Block copolymer Polystyrene-PNIPAM with n-butyl acrylate end group
PS	Polystyrene
RAFT	Reversible addition-fragmentation chain-transfer

List of abbreviations:

RLCA	Reaction-limited colloid aggregation
RT	Room temperature
SAS	Small-angle scattering
SANS	Small-angle neutron scattering
SAXS	Small-angle X-rays scattering
SLD	Scattering length density
t	time
T	Temperature
TEM	Transmission electron microscope
T-jump	Temperature jump
TR	optical transmission
tr-SANS	Time-resolved SANS
UCST	Upper critical solution temperature
UV-Vis	Ultraviolet-visible
VPT	Volume phase transition

1. Introduction

Polymers that exhibit a temperature-induced volume phase transition are of great interest as functional, stimuli-responsive materials.[1,2,3] One of them is poly(N-isopropyl acrylamide) (PNIPAM), which shows a thermo-responsive behavior close to the physiological temperature,[4] thus can be used for biomedical applications.[2,5] Phase transition in its solution occurs by reducing the polymer solubility upon heating, which can be associated with aggregation.[4] Since 1968,[6] PNIPAM has become an excellent example to study thermo-sensitive prosperities. The chemical differentiation,[7,8] as well as the addition of e.g. surfactant[9] to the polymer solution, can change the aggregation process. Therefore, understanding of kinetics and thermodynamics of the phase transition is essential for developing and designing new functional materials. In general, two main factors determine the transition kinetics: solvent diffusion and dynamics of polymer chain relaxation, where the dynamics dependents i.a. on polymer size. Recent experiments have shown that the transition kinetics can progress through transient states with different lifetimes and characteristic chain dimension, leading to relatively complex multi-step kinetics.[10,11,12,13]

Kinetics examinations have mainly been conducted on temperature-induced swelling and collapse transitions of micro- and macrogels over time scales from seconds to hours. The relationship between the observed volume phase transition kinetics and basic molecular processes, which mainly occur on sub-micrometer and sub-second time scale, has not yet been established. Few groups have investigated the kinetics from milli- to microsecond time scales, and the interpretation of their results has been partially contradictory.[11,12,13,14]

The El-Sayed group conducted the first relevant experiment probing the kinetics across the lower critical solution temperature (LCST) on microseconds time scale for PNIPAM microgel.[15] The structural changes caused by laser-induced temperature jump were attributed to processes of polymer collapse at the periphery of the microgels and have been observed by detection of the optical transmission. Subsequently, kinetic experiments on linear PNIPAM polymers were reported using time-resolved fluorescence spectroscopy,[10,11] Raman spectroscopy,[12,16] optical transmission measurements,[13,17] and refractive index.[14] Fluorescence and refractive index indicate that the first coil collapse processes occur over time scales of 100 μs,[10,11,12] followed by further processes progressing for 0.8 – 1 ms[10,11] and 10 – 60 ms,[13] which were interpreted as a coil collapse with the onset of aggregation. Raman spectroscopy indicates that the temperature jump initially reduces the local hydrophilicity of polymer within 100 ns. This is followed by a local dehydration over the time scale up to 360 ns.[12] The structural changes of micellar PNIPAM copolymer

were followed from seconds to minutes by small-angle neutron scattering (SANS).[18,19] Slow volume changes of PNIPAM microgels were traced by video microscopy.[20,21]

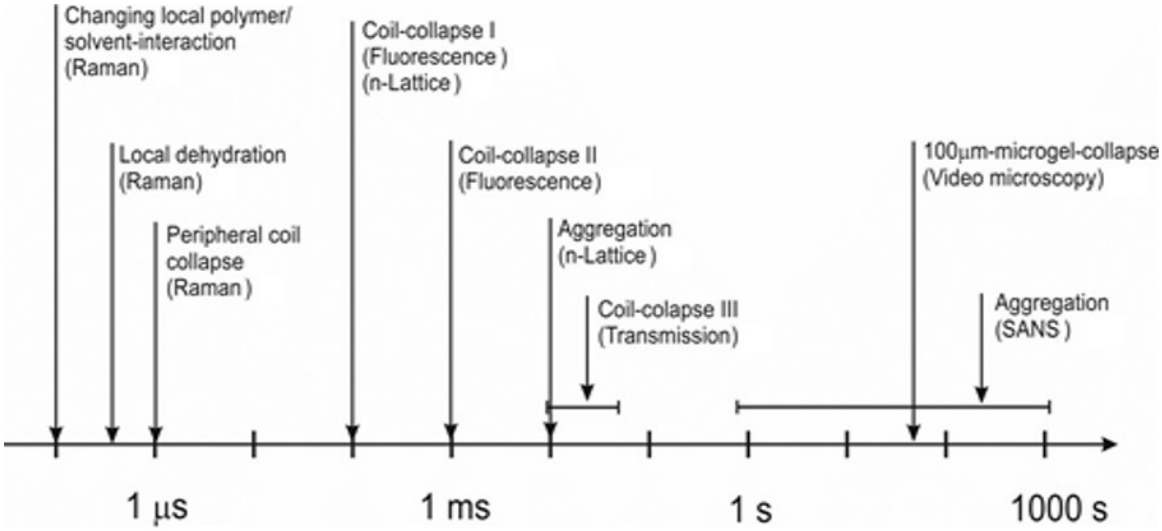

Figure 1. Schematic illustration of the literature results for the characteristic time scales of temperature-induced coil collapse and aggregation processes for PNIPAM-homopolymers, -micelles, and -microgels. Different experimental methods were used, where different relaxations were distinguished, which can be attributed to different coil collapse processes.

Reported time-resolved experiments so far show that upon crossing the LCST, structural changes are observed on time scales from 10^{-7} to 10^{2} s depending on the method and the polymer system. An overview of literature results is schematically presented in Figure 1. The graph shows an inconsistent image of the coil collapse. Moreover, the process of collapse may overlap with the onset of aggregation. Along with the formation of meta- or long-term stable mesoglobules, the analysis of observed kinetics of the volume phase transitions becomes a difficult task.

2. Fundamentals and Theory

2.1.The carrier system

2.1.1. Introduction to Stimuli-Sensitive polymers

Nowadays, “smart” materials that respond to external or internal stimuli are one of the most developing areas of science and industry. There are many possibilities of synthesis and design of stimuli-responsive polymers, serving many inspirations for creating synthetic materials which can reply to stimuli in a controllable and predictable manner. Polymers responding to their environment by changes of their physical or/and chemical properties,[22,23,24] have been studied over the years on a broad applications range. Mostly used external stimulants are: temperature,[25,26,2,3,27] pH,[28,3] light,[27,29] ionic strength,[28,30] solvent composition[31,32] and electric/magnetic fields.[3,33] The stimulants can be divided into physical and chemical ones.[3] Physical stimuli, such as light, electric/magnetic field, temperature, are related to specific parameters that change the interaction energy between molecules. A polymer, which reacts to the chemical stimuli, modifies interactions and structure by increasing/decreasing e.g., pH or ionic strength. As materials are responsive to stimuli, reaching an energy equilibrium state is indicated. Such as state preserve to network functionality and build an architecture that needed lower energy go through the phase transition. Mostly, the phase transition shows two meta-stable energy minima, which indicates energy needed for overgo from one state to another and it can be reversible. That can describe different kinds of transitions, such as disorganization of hydrogen bonding, conformational changes, aggregation-dissociation or penetration-separation transitions.[3] Stimuli-responsive behavior, of “smart” polymers, is fundamentally guided by functional groups which are in or on a polymer chain. The combination of two or more functional moieties in the polymer chain expands the responsiveness of materials and allows design for more specific application requirements.

2.1.2. Thermo-responsive polymers

Of the various possible stimuli, temperature is the most widely used in the responsive polymers field. Thermo-responsive polymers exhibit a miscibility gap in the binary diagram at upper or lower critical solution temperature, UCST or LCST, and the phase separation into polymer-rich and polymer-poor phases (Figure 2). On the phase diagram of polymer with UCST behavior, the two liquid phases are observed upon

temperature decrease, and the miscibility in all proportions is observed above the critical temperature.[34] Agarwal et al. showed that poly(*N*-acryloyl glycinamide) (PNAGA) displays UCST behavior as long as ionic groups are absent.[35] Ritter et al. synthesized a copolymer with tunable UCST based on N-vinylimidazoles[36] and Shimada group synthesized functionalizing UCST polymers by post-modification of poly(allylamine) and poly(L-ornithine).[37]

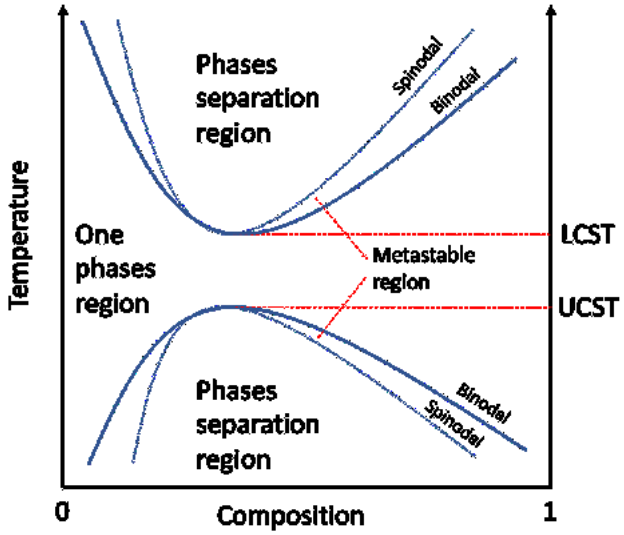

Figure 2. Phase diagram for a binary polymer-solvent mixture including LCST and UCST behavior.

Lower critical solution temperature is defined as a critical temperature below which all components in solution are miscible in all compositions. Below the critical temperature, polymer chain and solvent molecules are in uniform phase. Above the LCST, the phase separation occurs by the entropically driven process.[38]

To determine the LCST, the phase diagram is used in range of temperature and concentration for the binary system. The solution concentration at the minimum of the binodal is called a lower critical solution temperature concentration (LCSTC). The hydrophilic polymer chain creates hydrogen bonds with surrounding water molecules at low temperature. Thus, polymer is hydrated and solubilized, resulting in one-phase solution. The hydrophobicity of the polymer increases with heating, from hydrophilic to hydrophobic state. Hydrogen bonds (H-bonds) become weak at the transition temperature, and polymer chains are partially dehydrated. Further warming up leads to polymer aggregation. Breaking down the H-bonds between polymer and water molecules at high temperature is caused by turning into the Gibbs free energy of mixing (*Eq.1.*) to a positive value due to varying the entropy and enthalpy contributions.

$$\Delta G = \Delta H - T\Delta S \qquad \textit{(Eq.1.)}$$

Bonds between water molecules and polymer chains result in a favorable enthalpy of mixing (ΔH). However, the orderliness increases in the solution, which adversely affects the entropy of mixing. The entropy term ($T\Delta S$) becomes predominant with temperature increase, and the Gibbs free energy turns to positive, what results to a phase separation.[39] In the solution below critical temperature, hydrated polymer chains are in coil conformation. Contact between polymer and surrounding water molecules is minimized above LCST, which leads to a globular conformation of polymer. Hence, the coil-to-globule transition (Figure 3) can be describe as first order phase transition due to its entropy-driven by the water molecules that raise the system's entropy by dehydration of the polymer chains above LCST.

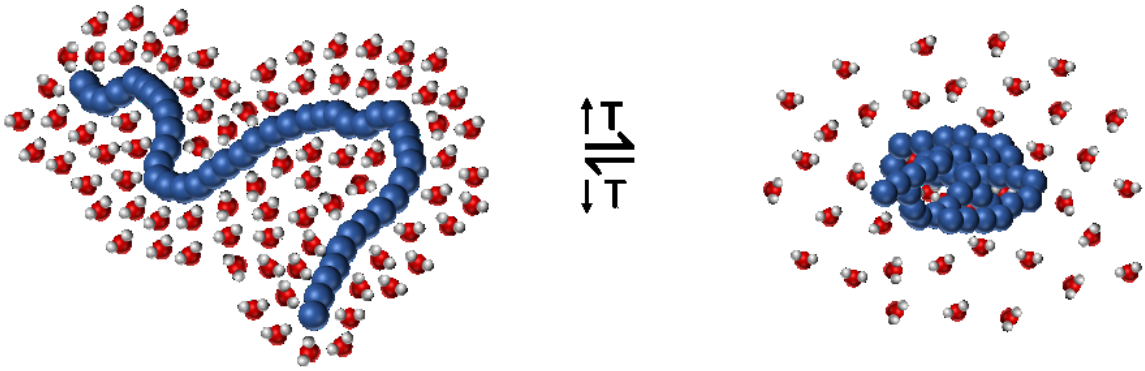

Figure 3. Coil-to-globule transition in polymers with LCST behavior.

One of the most well-known and extensively studied polymer that exhibits an abrupt volume change above LCST is poly(*N*-isopropylacrylamide).[4] Nevertheless, there are many other polymers that display the LCST, such as: poly[*N*-[2-(diethylamino) ethyl]acrylamide] (PDEAEAM),[40] poly(*N,N*-diethylacrylamide) (PDEAAM),[41] poly(oligoethylene glycol)methacrylate (POEGMA)[42,43] and poly(2-(N-morpholine)ethyl methacrylate) (PMEMA).[44]

2.1.3. Cloud point temperature

Second important parameter of thermo-responsive polymers is cloud point temperature (T_{cp}). This parameter refers to temperature at which the polymer solution occurs the coil-to-globule transition in a particular concentration and becomes turbid. The cloud points of solution at different concentrations can be located on the binodal curve on the phase diagram (Figure 2). Consequently, T_{cp} is a characteristic parameter for a polymer solution at a given concentration. LCST is at the minimum on the binodal curve for a specific polymer, and it is the lowest value of T_{cp} in the phase diagram. The cloud point of the polymer solution can be controlled and varied by copolymerization,[45,46,47] end-group functionalization,[48] tacticity,[46] concentration[49] or ionic strength[50] changes.

2.1.4. Phase separation

Berghmans and van Mele proposed the classification of the polymer solution phase separation to three types of polymers depending on their miscibility with water:

- Type I → polymers follow Flory-Huggins behavior, that means the minimum of the binodal curve in their phase diagram can be shifted by change of the polymer molecular weight or solution concentration. An example of type I polymer is poly(*N*-vinylcaprolactam).[51]
- Type II → polymers which the minimum of the demixing curves is barely shifted by change of the molecular weight, concentration, or architecture of the polymer. The example of type II polymer is poly(*N*-isopropylacrylamide),[52] for which the phase transition temperatures of star-shaped polymers and linear polymers are similar,[53] however there are exceptions in case of copolymerization with hydrophobic/hydrophilic group,[54,55] or densely grafted star-shaped polymer.[56]
- Type III → polymers show bimodal phase diagram, where two critical points are observed at low and high concentrations of the polymer. The minimum at low concentration has limited critical concentration for infinite molar mass, which correspond to Type I behavior. The second minimum at higher concentration is independent of the molar mass, which corresponds to behavior of Type II. An example of Type III polymer is poly(methylvinylether).[57,58]

2.1.5. Hysteresis

Hysteresis is defined as a dependence of the system state on its history. The hysteresis effect occurs for example in ferromagnetic and ferroelectric materials,[59] shape-memory alloys[60] or thermo-responsive polymers.[4] For ferromagnetic materials, there is a hysteresis curve for the magnetization, *M,* as a function of the applied magnetic field *H*, scheme of the magnetic hysteresis loop is shown in Figure 4a. It is characterized by a magnetic saturation, a remanence M_R, and a coercivity H_C.[61] In analogy, for thermo-responsive polymers there is a thermal hysteresis for specific properties such as the hydrodynamic radius, R_H, the optical transmittance, *TR*, or the backscattering intensity, I_{BS}, as a function of temperature. The example of the optical transmission is shown in Figure 4b to define a hysteresis window of width ΔT with a central transition temperature, T^*, which defines the remanence optical transmittance, TR_R^+ and TR_R^- as well as the coercive temperatures, T_C^+ and T_C^-, for the volume phase transition.[62]

The swelling/collapse or coil/globule transition of the polymer is related to polymer/water and polymer-polymer hydrogen bond formation. In the swollen coil state,

there are stable polymer-water hydrogen bonds between the polymer carbonyl (-C=O) and the polymer amine group (-N-H) and water, mediating good solubility of the polymer chain and water.[63,64] Upon the volume phase transition the polymer-water hydrogen bonds are split, and the polymer form polymer-polymer hydrogen bonds between the amine group and the carbonyl group (-C=O···H-N-),[64] structurally similar to polypeptides. Only at a sufficiently low temperature below LCST, at T_c^-, the polymer-polymer hydrogen bonds break, and the polymer chains return to their swollen coil solution state. The hysteresis effect, upon cooling from the collapse state to the swollen state, can be explained by the persistence of the polymer-polymer hydrogen bonds acting as cross-linking points.[63,65] This explanation is supported by the fact that LCST-polymers which do not have a -N-H groups, such as poly(*N,N'*-diethylacrylamide) (PDEAM), do not show any hysteresis.[66,67]

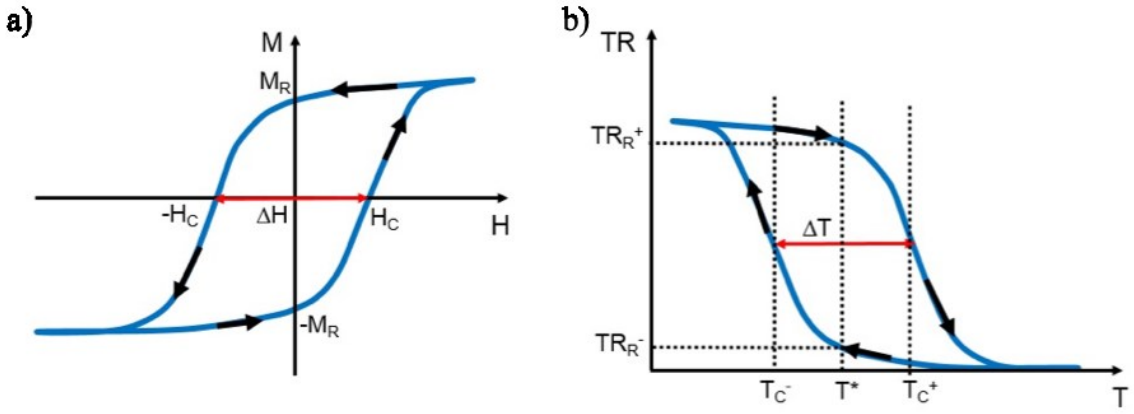

Figure 4. a) Scheme of a magnetic hysteresis loop with magnetization, M, and applied magnetic field strength, H, for a typical ferromagnetic material. H_C is coercive magnetic field strengths, M_R is the remanent magnetization, and ΔH is the width of hysteresis window. (b) Scheme of a thermal hysteresis loop with the optical transmission, RT, and temperature, T, for a thermo-responsive polymer. T_C represents coercivity temperatures, TR_R is the remanent optical transmission, and ΔT is the width of thermal hysteresis window.[62]

2.1.6. Polymer solution

Conformation of the diluted polymer chain depends on the interactions between them, thus the quality of the solvent. In a good solvent, dissolved polymer enlarges the chain to maximize the polymer-solvent contact, and for a poor solvent, the contact is minimized and interactions between polymer segments are preferable. In the case of the theta solvent, the chains are inert to solvent and to themselves, which means that interactions between polymer-solvent and polymer-polymer are the same. The size of the

polymer chains, end-to-end distance, is related to the number of the segments in polymer chain, and to solvent quality, $R_g \sim N^{\nu}$. The Flory exponent ν is equal to $\nu = 3/5$ for a good solvent, $\nu = 1/2$ for a theta solvent and $\nu = 1/3$ for a poor solvent.[68,69]

The solution concentration has influence on the interaction between polymer molecules. In dilute solution, the polymer coils are separated enough that there is no interaction between them. Overlap concentration (c^*) is define as the concentration at which the polymer coils start to overlap, and it separates dilute and semi-dilute solution. This concentration can be calculated according to *Eq.2.*, where M_w represents the molecular weight of the polymer chain, R_g is an end-to-end distance in polymer chain and N_A is an Avogadro's number.[70]

$$c^* = \frac{M_w}{\frac{4}{3}\pi R_g^3 N_A} \qquad \textit{(Eq.2.)}$$

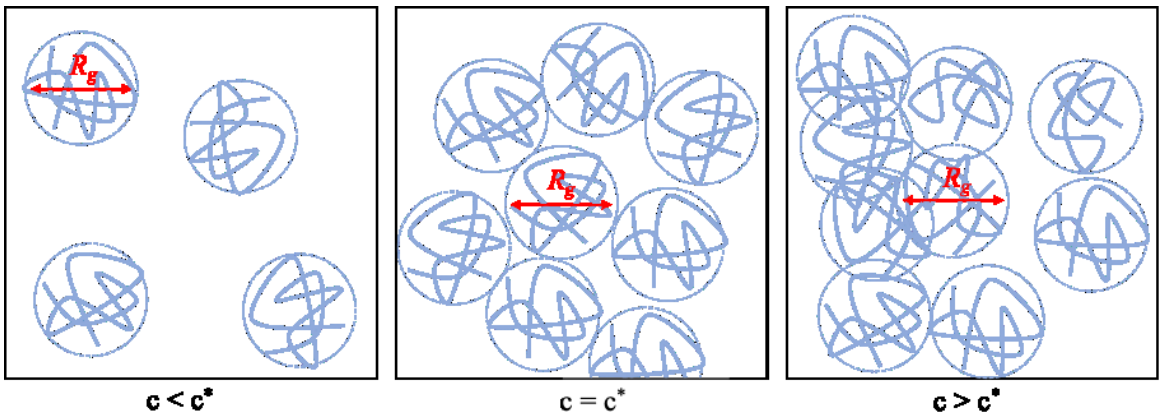

Figure 5. Scheme of polymer chain arrangement in solvent at different concentrations: in dilute solution (left), in overlap concentration (center) and in semi-dilute concentration (right).

2.1.7. Diffusion-limited polymer aggregation

The aggregation occurs by collision of particles due to their Brownian motions. When the repulsive energy barrier between two particles decreases significantly below thermal energy, k_BT,, reaction between connection points make bindings during collision. The energy of such binding is higher than thermal energy, thus a rigid cluster is formed. This is a diffusion-limited aggregation. In time, clusters can collide, thus larger aggregates are formed, and this process of kinetic growth is called the cluster-cluster aggregation with high polydispersity. Therefore, two time-regimes can be distinguished, fast and slow aggregation and both can be described by aggregation rate, τ. The first regime is called the

diffusion-limited cluster-cluster aggregation (DLCA), and its aggregation rate is limited by time between particles/clusters collisions due to diffusion. Next regime appears when time at which reaction rate is higher between clusters than the contacting time at collision, thus the aggregation rate is higher as well. The regime is called reaction-limited cluster-cluster aggregation (RLCA).[71,72]

Formed cluster by diffusion-limited aggregation can be characterized as a fractal with mass M_f, which is proportional to cluster's radius of gyration, $M_f \propto R_g^{d_f}$.[72] Mass fractal dimension is described in detail at section 2.3.1.4. II. The Smoluchowski's equation of coagulation (*Eq.3.*),[73,74] can be used to describe the cluster mass distribution in time, where N_n in the number concentration of aggregates with n size, and k is a rate constant.

$$\frac{dN_n}{dt} = \frac{1}{2}\sum_{i+j=n} k_{ij} N_i N_j - N_n \sum_{i=1}^{\infty} k_{in} N_i \qquad \textit{(Eq.3.)}$$

First term of *Eq.3.* represents every possible collision, which causes aggregates formation with size *n.* Second term describe the rate of aggregates with size *n* decay by aggregation with domains of any size. In general, from the Smoluchowski equation the rate constant can be calculated from *Eq.4.,* where the η is a dynamic viscosity of solvent, k_B is a Boltzmann's constant and T is a temperature of solution.

$$k_{ij} = \frac{2}{3}\frac{k_B T}{\eta}\left(i^{1/3} + j^{1/3}\right)\left(i^{-1/3} + j^{-1/3}\right) \qquad \textit{(Eq.4.)}$$

Consider the rate constant aggregation of particles with the same size, i.e., $k_{ij} = k_{11}$, then the *Eq.4.* can be expressed by *Eq.5.*

$$k_{11} = \frac{8}{3}\frac{k_B T}{\eta}\left[m^3/_s\right] \qquad \textit{(Eq.5.)}$$

After fast heating, polymer coil or micelle first collapsed thus, their size is equal for monodisperse polymers. Therefore, knowing the number of these particles in solution, time needed to initiate the aggregates is time of rapid coagulation, τ_{RC}, that can be calculated from *Eq.6.,* where N_0 is number concentration of particles with initial size.

$$\tau_{RC} = \frac{2}{k_{11} N_0} = \frac{3\eta}{4 k_B T N_0} \qquad \textit{(Eq.6.)}$$

The temperature dependence of the chemical or physical process rate that correspond to rate constant k, can be expressed by Arrhenius law (*Eq.7.*), where A is the preexponential (frequency) factor, which is related to collision frequency, R_{GC} is the gas constant and E_a is the activation energy.

$$k(T) = Ae^{-E_a/R_{GC}T} \qquad (Eq.7.)$$

Value of the activation energy can be estimated from slope of Arrhenius plot, *ln(k)* vs. *1/T*, and intercept gives the value of preexponential factor. E_a demonstrate a sensitivity of the process rate on temperature, thus the larger energy, the bigger difference in rate constant k with temperature.[75] Due to the phase transition is complex process, experimentally the correct activation energy can be distorted, thus the apparent E_a is more accurate. The apparent activation energy describes the overall energy that is needed for the transition from one to another state[76,77] and high value can be caused by effect of back reactions which corresponds to thermodynamic inhibition.[78] In the case of the phase transition, the values of activation energy were obtained high such us 110-140 kJ/mol for linear PNIPAM solution,[79] 300 kJ/mol for growth reaction of nitroamine high explosive HMX compound[78] or even more than 1000 kJ/mol for thermal denaturation of collagen.[80]

2.2. Poly(*N*-isopropylacrylamide)

One of the most commonly and successfully studied thermo-responsive polymers is Poly(*N*-isopropylacrylamide)[81,82,83] (PNIPAM, Figure 6). Its responsiveness is related to a miscibility gap detected above LCST in aqueous solution where sharply reduced solubility upon heating contributes to conformational transition in polymer chain. PNIPAM is of great interest in pharmaceutical and biotechnological applications because its LCST occurs near physiological conditions ($T_{LCST} \simeq 32$ °C).[84] On the molecular level, PNIPAM can be used as single polymer chains, block copolymer micelles, micro- and macroscopic gels,[83] thin films,[85] membranes,[86] fibers,[87] coatings or latexes.[88] Applications can use both reactions on temperature fluctuation, collapse or precipitation. Hence, collecting cell sheets applies the collapse transition from PNIPAM brush,[89] while bioseparation of PNIPAM-conjugated proteins uses demixing.[90] Pioneering work on the PNIPAM and its phase separation is the Heskins and Guillet article from 1968 year.[6] For the first time, they investigated in detail the phase transition of PNIPAM aqueous solution with LCST at 31.0 °C and a monomer volume fraction of $\phi_{LCST} \simeq 0.16$. Below the transition temperature, PNIPAM chains exist as coils due to hydrogen bonding between amide groups and water molecules. Above the LCST, the polymer chains are dehydrated by breaking down H-bonds between polymer and water, and form H-bonds between amide groups in PNIPAM chains lead to sharp and abrupt phase transition[91] compared to other responsive polymers. However, even at the temperature above the phase transition, PNIPAM chains still can contain 20 % - 50 % water[92] and hydrogen bonds between the amide group and water molecule were detected by FTIR spectroscopy at 40.0 °C.[64] Over years, PNIPAM was examined in detail by different groups however, they met with large deviations in phase diagram mapping due to the physical forms, used techniques and the methods of polymerization.[81] Nevertheless, the minimum of the mixing curves of pure PNIPAM solution is barely affected by changing the chain length or polymer concentration, which corresponds to Type II behavior of the phase transition.

The hydration properties of PNIPAM solution depends not only on temperature but the phase transition can be caused as well by pressure,[93] pH[94] or solvent composition.[95,96] In the case of pressure increase above LCST, dehydration of the polymer chain change and such hydrophobic interactions plays an important role. They are assigned to entropic term in Gibbs free energy (*Eq.1.*) and results from the difference in density between disorder water structure in bulk and tetrahedral structure close to nonpolar surface. At the atmospheric pressure, the water molecules form a tetrahedral structure around the hydrophobic groups. Therefore, the entropy increases, thus making hydration of the groups more difficult. For pressure increase, the water structure change from (low-density) open tetrahedrical to (high-density) compact hexagonal structure. That means the hydrophobic effect is weakened. Additionally, the volume of the system decreases due to change of

water density in the hydration shell around hydrophobic groups and penetration of water molecule to these groups, which in the case of proteins causes denaturation[97] or for linear PNIPAM chains swelling of the mesoglobules.[93]

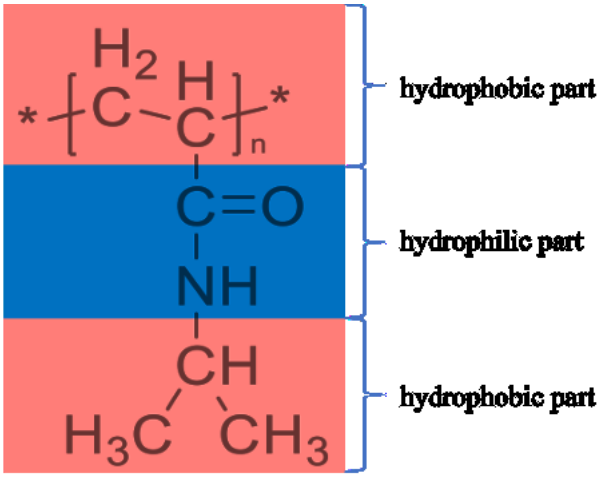

Figure 6. PNIPAM structure.

2.2.1. PNIPAM-based copolymers

Thermal responsiveness of PNIPAM-based polymer can be tuned by choice of comonomer, its hydrophobicity or its fraction,[98] the molecular weight of PNIPAM chain, or the functionalization of end groups.[99] Addition of hydrophilic block to PNIPAM polymer chain raise the LCST of the copolymer and slower down the phase transition. The hydrophilic group in thermo-responsive polymer chain causes enhancing an interaction between polymer and water molecules what increase in the enthalpy of hydrogen bonding between the polymer chain and water.[100,101] In the contrast, hydrophobic block in copolymer causes shifting of the PNIPAM phase transition PNIPAM to lower temperatures compare to pure PNIPAM polymer. At LCST the transition is clear and sharp. Copolymers with PNIPAM and hydrophobic block has a critical concentration of hydrophobic moiety above which polymer is no longer soluble in water.[101] Additionally, hydrophobic block contribution in PNIPAM copolymer can cause a self-assembly in aqueous solution, PNIPAM copolymer with hydrophobic block can self-assembly by hydrophobic interactions in different structures like micelles, cylinders or rods-like.

2.2.2. Micellization

The block copolymers consist of two or more different blocks in one polymer chain can form among others a radial arrangement due to microphase separation. The simplest

structure with this arrangement is star-shaped micelles, where *n* blocks from polymer chains are linked to one point.[102] In the case of hydrophobic-hydrophilic block copolymer, in solvent chains can assembly to hydrophobic "rigid" micellar core and hydrophilic "soft" micellar shell. The structure can be extended to rod-like or ellipsoidal shape by changing the packing number of the chains.[68]

To describe the thermodynamic of the micelle formation can be used the approach as phase separation model. The Gibbs energy of the micellization is expressed in *Eq.* 8. (R_{GC} is a gas constant and *CMC* in a critical micelle concentration) and can be used for nonionic block copolymers. In most of cases, the CMC in lower than c = 1M, thus the ΔG_{mic} is negative indicate on the spontaneous process.

$$\Delta G_{mic} = R_{GC} T \, ln(CMC) \qquad (Eq.8.)$$

The formation of the micelles is caused by two factors. First, the transfer of the hydrophobic polymer blocks to oil-like interior in order to limit the contact with water (hydrophobic effect). The water molecules are highly ordered surrounding the hydrocarbon groups, and the entropy increases, thus this process in entropically driven. The second factor is a repulsion of polar groups in copolymers by getting closer to each other in micelle. Additionally, the steric effect reduces their mobility and decrease of entropy causes the repulsion.[103]

In the case of the micelles assembled by block copolymers, the length of individual blocks can influence on the type of these micelle. The correlation between the molecular parameters of micelles, such as the radius of the core (R_c), the shell thickness (R_{shell}) or the aggregation number (*Z)* used to establish model based on scaling theory. Considering the block copolymer, two types of micelles can be described (Figure 7) for *AB* block copolymers based on the ratio of monomer units number *N* of individual blocks in chain.[102] Symbol *A* represents hydrophilic block, and *B* hydrophobic block. For $N_A \ll N_B$ the type of micelle is "crew-cut" micelle, thus the radius of the core is larger than the shell thickness, $R_{shell} \ll R_{core}$. To express the relations of scaling parameters for this type of micellar system, can be used the theory for polymer brush. The relationship between the core radius and aggregation number to the number of hydrophobic segments can be describe as $R_{core} \sim \gamma^{1/3} N_B^{2/3} a$ and $Z \sim \gamma N_B$, where γ is a *A/B* interfacial surface tension and a is a length of one segment. In the case that the hydrophilic block is longer than the hydrophobic block, $N_A \gg N_B$ indicates "hairy" micelle type and the Daoud and Cotton theory of star-like polymer can be used. Their model predicts the radius of the star-polymer structure and can be express as $R \sim N_A^{3/5} \nu^{1/5} f^{1/5} a$, where ν is a monomer excluded volume and f is the number of arms.[104]

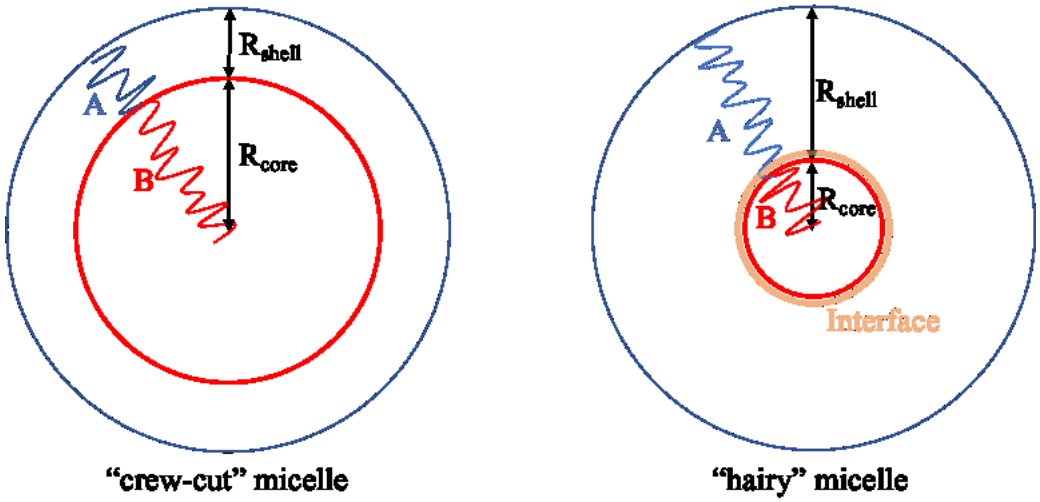

Figure 7. Scheme of AB block copolymer micelles depends on the length of individual blocks in polymer chain.

2.2.2.1. Critical micelle concentration

Critical micelle concentration (*CMC*) is a concentration at which micellization occurs thus the polymer chains self-assembly to the micelle at given temperature. Below this concentration is observed only dissolved chains (unimers) in solution. Considering the hydrophobic effect, with increase of the hydrophobic block length, the CMC decrease. To establish the CMC of the polymer can be used many techniques such as dynamic light scattering, surface tension measurement or turbidimetry. Micellization can also be observed by change of temperature for given concentration above or below critical micelle temperature (*CMT*), which depends on whether the self-assembly process is endo- or exothermic.[68]

2.3. Study of the morphology changes across LCST of responsive polymers

2.3.1. Small angle scattering

Small-angle scattering (SAS) of neutron (SANS) or X-ray (SAXS) is a powerful technique that is used to study, e.g. the morphology of the polymer in solution at different conditions, like temperature or pressure. SAS aims at a length scale from nano- to micrometers. Therefore, the structural information and interactions of investigated systems can be determined. For neutrons, the scattering is determined by interaction with atomic nuclei and with magnetic moments for magnetic materials. While the incident radiation with electrons can be determined by X-rays scattering.[105] SANS/SAXS are noninvasive techniques, and the physical quantities like a radius of gyration, fractal dimension and volume are averaged over the macroscopic volume. Then, the size of the basic structural units can be obtained at different compositions or size of the fractals. Technique can be used for kinetics experiments to follow changes of the investigated polymer systems after fast conditions changing from milliseconds to minutes time range in real-time as well.

2.3.1.1. Theoretical background

In the SAS experiment, a neutron/X-rays beam is emitted from a source with a wave vector $\overrightarrow{k_i}$ and hits the sample. A part of the incident beam passes through the sample, although a small fraction is scattered from the sample with the wave vector, $\overrightarrow{k_s}$, by a certain angle, 2θ, and recorded by the detector. Scheme of the small-angle scattering is presented in Figure 8. With consideration of elastic scattering, thus the energy change for radiation is negligible, and the neutron/X-rays source emits monochromatic radiation, which means that the radiation has one given energy, the magnitudes of wave vector $\overrightarrow{k_i}$ and $\overrightarrow{k_s}$ are equal (*Eq.9.*).[106]

$$k = |\overrightarrow{k_i}| = |\overrightarrow{k_s}| = \frac{2\pi}{\lambda} \qquad (Eq.9.)$$

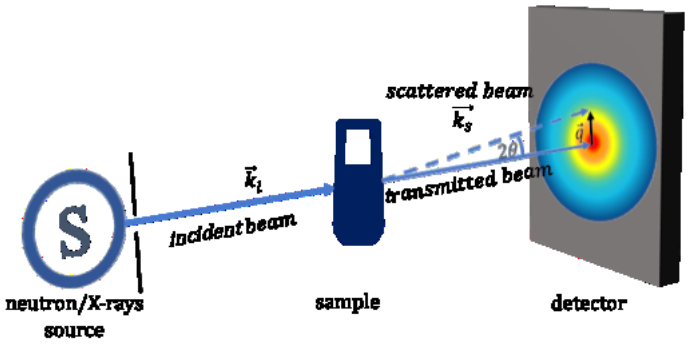

Figure 8. Scheme of the small angle scattering experiment.

Further, the magnitude of scattering vector, q, can be defined as a subtraction of incident wave vector from scattered wave vector and can be estimated from the scattering angle, 2θ, and wavelength of the radiation, λ, (*Eq.10, Eq.11.*).

$$\vec{q} = \overrightarrow{k_s} - \overrightarrow{k_\iota} \qquad \textit{(Eq.10.)}$$

$$q = |\vec{q}| = \frac{4\pi}{\lambda} sin\theta \qquad \textit{(Eq.11.)}$$

The scattering length density distribution $\rho(\vec{r})$ is defined as the scattering length, b_j, of particles per unit volume and it is used to describe the scattering from assemblies of the particles (*Eq.12.*, where $\vec{r}$ is a relative position of the particle). Using the Fourier transform of $\rho(\vec{r})$, the total scattering amplitude, $A(\vec{q})$, can be described as in *Eq.13.*, where v is the total volume of sample irradiated by beam, and $\vec{q}\vec{r}$ is the phase shift between scattered waves from different particles.

$$\rho(\vec{r}) = \sum_j b_j(\vec{r} - \vec{r_j}) \qquad \textit{(Eq.12.)}$$

$$A(\vec{q}) \equiv \int_v \ \rho(\vec{r})\, e^{i\vec{q}\vec{r}} d^3r \qquad \textit{(Eq.13.)}$$

Consider that the solvent, at which the particles are dissolved, is a featureless matrix (ρ_s), the difference in scattering amplitude from the particle relative to equivalent solvent volume, and the contrast of scattering length density, $\Delta\rho(\vec{r})$, can be define according to *Eq.14*.

$$\Delta\rho(\vec{r}) = \rho(\vec{r}) - \rho_s \qquad \textit{(Eq.14.)}$$

Amplitude of scattered wave is not measurable, thus the spherically averaged scattering intensity, *I(q),* from a single particle in monodisperse and dilute sample can be calculated by multiplication of $A(\vec{q})$ by its complex conjugate $A^*(\vec{q})$ as it is described in *Eq.15*. In the equation, $\vec{r}_j - \vec{r}_k$ is a distance vector between two, j[th] and k[th], scattering particles.[107]

$$I(q) = A(\vec{q}) * A^*(\vec{q}) = |A(\vec{q})|^2 = \int_V \ \int_V \ \rho(\vec{r}_j)\, \rho(\vec{r}_k) e^{i\vec{q}(\vec{r}_j - \vec{r}_k)} d\vec{r}_j d\vec{r}_k \qquad \textit{(Eq.15.)}$$

Considering that $\langle e^{i\vec{q}\vec{r}} \rangle = \frac{\sin qr}{qr}$ and integrating the *Eq.15.* in spherical coordinates, the scattering intensity can be described as in *Eq.16*. D_{max} is the largest particle diameter,

$\gamma(r) \equiv \rho(\vec{r}) * \rho(-\vec{r})$ is the correlation function of the particle, with $\gamma(r) = 0$ for $r > D_{max}$. For that, the correlation function can be defined as averaged self-convolution of density distribution due to the symbol *, used as convolution.

$$I(q) = 4\pi \int_0^{D_{max}} r^2 \gamma(r) \frac{\sin qr}{qr} dr \qquad \textit{(Eq.16.)}$$

The relationship between *I(q)* and distance correlation, *r*, can be describe as a real-space scattering-pair distance distribution, $p(r) = \gamma(r)r^2$. Then the *Eq.16.* can be express as in *Eq.17.*

$$I(q) = 4\pi \int_0^{D_{max}} p(r) \frac{\sin qr}{qr} dr \qquad \textit{(Eq.17.)}$$

With reverse transformation of *Eq.17.*, the real-space scattering-pair distance distribution in relation to scattering intensity can be express as in *Eq.18.*

$$p(r) = \frac{r^2}{2\pi^2} \int_0^{\infty} q^2 I(q) \frac{sin(qr)}{qr} dq \qquad \textit{(Eq.18.)}$$

Then, the scattering intensity, which is associated form factor amplitudes of particle in reciprocal space, relates to frequency of atom-pair distances in the particle in real-space by a Fourier transform.

In general, the scattering intensity can be described as in *Eq.19*, where ϕ is a volume fraction, $\Delta\rho$ is a scattering length density contrast, *V* is a volume, *P(q)* is a form factor, which is related to the distribution of scattering material in particle, and *S(q)* is a structure factor, which depict the spatial distribution of the scattering particles in the solvent.

$$I(q) = \phi\ (\Delta\rho)^2\ V\ P(q)\ S(q) \qquad \textit{(Eq.19.)}$$

2.3.1.2. Form factor

The scattering from a single particle can be described by the form factor *P(q)*. The scattering intensity can be expressed with *Eq.20.,* where *N* is the particle numbers in solution, V_p is the volume of one particle and $\Delta\rho$ is the difference in electron density between scattering length density (SLD) of particle, ρ_p, and SLD of solvent ρ_s. Thus, the form factor can be determined by *Eq.21.*

$$I(q) = \frac{N}{V} (\Delta\rho)^2 V_p^2 \left| \frac{1}{V_p} \int \Delta\rho(r) e^{iqr} dr \right|^2 \qquad \textit{(Eq.20.)}$$

$$P(q) = \left|\frac{1}{V_p}\int \Delta\rho(r)e^{iqr}dr\right|^2 \qquad \textit{(Eq.21.)}$$

2.3.1.2.1. Guinier approximation

Guinier approximation is widely used for determination of radius of gyration, R_g, and molecular weight, M_w, of the particle in studied sample. At low scattering vector ($q < \frac{2\pi}{D_{max}}$), substituting the McLaurin series at $\frac{\sin(qr)}{qr} \simeq 1 - \frac{(qr)^2}{3!} + \cdots$ to *Eq.16.* gives the Guinier equation *Eq.22.*, where $I(q = 0)$ is a forward scattering intensity.

$$I(q) = I(0)\left(1 - \frac{q^2R_g^2}{3} + \cdots\right) \qquad \textit{(Eq.22.)}$$

$$R_g = \frac{1}{2}\int_0^{D_{max}} \gamma(r)r^4dr \Big/ \int_0^{D_{max}} \gamma(r)r^2dr \qquad \textit{(Eq.23.)}$$

$$I(0) = 4\pi\int_0^{D_{max}} \gamma(r)r^2dr = \frac{N}{V}\left(V_p^2\Delta\rho^2\right) = \frac{cM_wV}{N_a}(v\Delta\rho^2) \qquad \textit{(Eq.24.)}$$

The Guinier plot, $\ln\big(I(q)\big)\ vs.\ q^2$ (Figure 9b, *Eq.25.*), should give a linear function in case of the monodisperse system, and with the slope, $R_g^2/3$, the radius of gyration value of the particle in solution can be obtained. The radius of gyration (*Eq.23.*) is defined as the radial distance from the center of the particle to the point where the moment of inertia is the same as the actual mass distribution of the object. However, the Guinier approximation is valid for small angle range $qR_g < 1$. From the plot, additionally the intercept yields the value of *I(0)* which is related to the molecular mass of the particle.[107,108]

$$ln\big(I(q)\big) = ln\big(I(0)\big) - \frac{R_g^2}{3}q^2 \qquad \textit{(Eq.25.)}$$

Also, from the Guinier plot the molecular weight can be determined. The forward scattering is expressed in *Eq.24.*, where c is a concentration of sample $c\left[{}^{mg}/_{mL}\right] = \frac{NV_p}{vV}$, M_w is a molecular weight $M_w = \frac{V_pN_a}{v}$, v is specific volume of the particle and N_a is Avogadro's number.

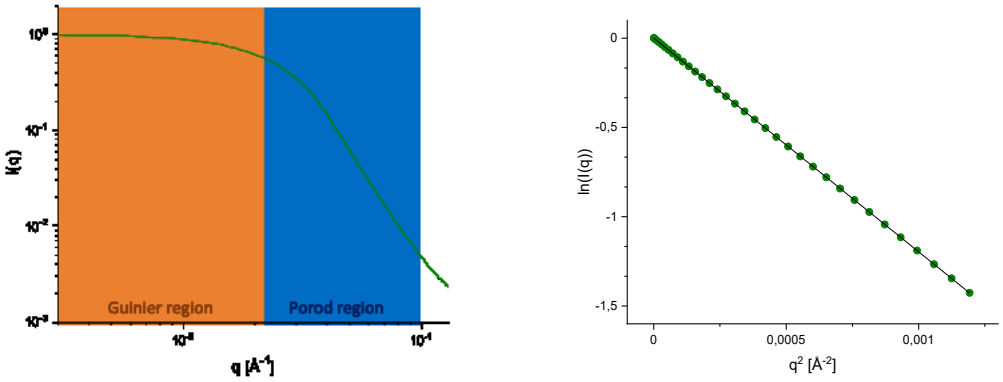

Figure 9.a) Simulated SAS profile and b) Guinier plot for particle with R_g = 50 Å and Porod exponent d = 4.

2.3.1.2.2. Porod law

The Porod region can be assigned for the higher scattering vector $\left(q > \frac{2\pi}{D_{max}}\right)$, where the local structure of the particles can be designated. The Porod law (*Eq.26.*) applies to any scattering systems with a sharp SLD interface between sample and matrix. In the equation, *F* represents the amplitude of the Porod scattering and express the surface to volume ratio, $F = 2\pi(\Delta\rho)^2 \frac{S_{tot}}{V_{tot}}$, where S_{tot} is a total surface area and V_{tot} is the total volume of the solution. With a decrease of the surface to volume ratio, the larger radius of the particle is. According to the Porod's law, the scattering intensity increases monotonically with decreasing of *q*-value, and it is not defined for $q = 0$.

$$I(q) = Fq^{-d} \qquad \textit{(Eq.26.)}$$

The slop of the Porod form factor at the high *q*-range is determined only by the structure surface and in that region, it provides information about the fractal dimension, *d*, of the scattering particles. The slope of -1 is assigned to rigid rods, although a Porod slope -4 is obtained for smooth surface of the scattering particle and slope between -3 and -4 characterizes the rough interface of fractal dimension *D* with 6-*D* and it is called a surface fractal. In the case of polymer coils, the slope -2 indicate a Gaussian chain in dilute solution, -5/3 indicates a fully swollen coils and -3 is for collapsed coils. A slope between -2 and -3 is for co-called mass fractals such as networks or branched systems. In the case of spherical particles, the slope of form factor is -4 (Figure 9a) and the Porod law is described by *Eq.27.*, where *S* is the surface volume of the particle.[109,110]

$$I_{PL}(q) = \frac{2\pi S}{q^4}\Delta\rho^2 \qquad \textit{(Eq.27.)}$$

2.3.1.2.3. Sphere

The form factor for monodisperse sphere with uniform SLD is described in *Eq.28*. *R* represents a radius of the sphere and V_s as a sphere volume $V_s = \frac{4\pi}{3}R^3$.[111] The simulated SAS curve is presented in Figure 10. From the SAS curve, the first minimum of the form factor describes the size of the homogenous spherical particle in solution, and the slope for high *q*-range is to the power of -4, which is characteristic for spheres. Well visible maxima and minima on the SAS curve indicate low polydispersity of the spheres.

$$P_S(q) = \frac{1}{V_s}\left[3V(\Delta\rho)\frac{(sin(qR)-qRcos(qR))}{(qR)^3}\right]^2 \qquad \textit{(Eq.28.)}$$

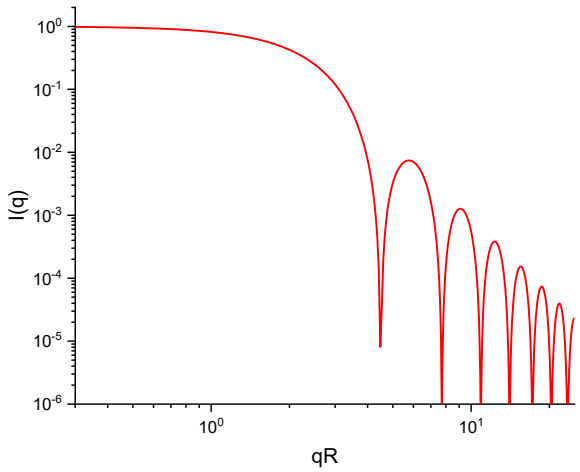

Figure 10. Simulated form factor for a spherical particle with radius R = 60 Å.

In dilute solution, spheres are separated, therefore, the correlation between them is not observed and the forward scattering can be obtained. In that case, and when the particle concentration and electron density are known, the molecular weight of the sphere can be calculated.

2.3.1.2.4. Core-shell sphere

In the case of the spherical particles with the core-shell structure, the form factor can be expressed as in *Eq.29*. Block copolymer micelles have a different SLD for core

(ρ_{core}) and shell (ρ_{shell}) thus, the contrast between them should be included in the form factor. The volume of the whole sphere is represented as V_s and volume of the core as V_{core}. Assuming that, the core and shell have homogenous SLDs, *P(q)* of core-shell sphere can be described as two spherical form factors with different contrast.

$$P_{CS}(q) = \frac{1}{V_s}\left[3V_{core}\,(\rho_{core} - \rho_{shell})\,\frac{(sin(qR_{core}) - qR_{core}cos(qR_{core}))}{(qR_{core})^3} + 3V_s\,(\rho_{shell} - \rho_s)\,\frac{(sin(qR_s) - qR_s cos(qR_s))}{(qR_s)^3}\right]^2 \qquad \textit{(Eq.29.)}$$

Model provides information about the radius of the micellar core, R_{core}, and shell thickness, R_{shell}=$R - R_{core}$. Due to the core having contact with shell, the scattering length density contrast is expressed as $(\rho_{core} - \rho_{shell})$. Further, the shell has a contact with solvent from another side, and the SLD contrast is $(\rho_{\text{shell}} - \rho_s)$. In Figure 11 on the left side, the simulated curve for core-shell spere form factor is presented, and two kinds of oscillation can be distinguished due to different size of micellar core and shell.

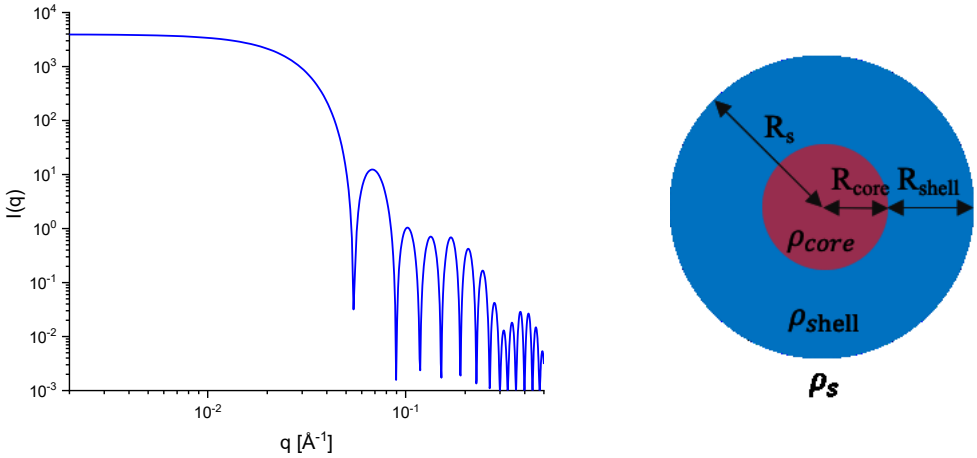

Figure 11. On the left side, the simulated SAS curve of core-shell sphere with radius of the core R_{core} = 60 Å and shell thickness R_{shell} = 150 Å. On the right side is a model of core-shell micelle with marked form factor parameters. On the right side, the scheme of core-shell micelle is presented with marked size of the micelle, core, and shell, as well as SLDs of every component.

Model is designed for a spherical particle with homogeneous core and shell densities, and can be used e.g. for polymer brush grafted on the spherical surface.[112,113] In the case of core-shell micelles self-assembled from block copolymers, this assumption is usually correct for micellar core. However, in most cases the shell is swollen, although the SLD decreases to outer end of sphere. For that, the form factor can be described with core-multishell sphere model, where the SLD contrast between SLD shell and solvent,

decreases from core to the outer end with $r^{-\alpha}$ decay (*Eq.30.*).[114] In the case of starlike profile, when polymer shell is swollen, the decay factor $\alpha = 4/3$, with decrease of the α to 0, the SLD of the shell become constant through the whole shell thickness.

$$\rho_{shell}(r) \propto r^{-\alpha} \qquad \textit{(Eq.30.)}$$

2.3.1.3. Fluctuation

In the liquid system with single component-rich particles, the characteristic correlation length of the inhomogeneities within the particle can be determined by Ornstein-Zernike equation *Eq.31*.[115] The scattering intensity is modelled by a Lorentzian function according to the Ornstein-Zernike theory.[116,117] The fluctuation can be visible in high *q*-range, where form or structure factor no longer influences on the SAS profile.

$$I_{OZ}(q) = \frac{I_{OZ}(0)}{1+q^2\xi^2} \qquad \textit{(Eq.31.)}$$

In *Eq.31.*, ξ represents the correlation length that characterizes the spatial extension of the SLD fluctuation, and $I_{OZ}(0)$ describes the scattering intensity at $q = 0$, which can be derived from domains with different SLDs due to density and concentration fluctuations.

2.3.1.4. Structure factor

Structure factor, *S(q)*, describes the spatial arrangement of the particles relative to each other in solution, thus the correlations between them. In the dilute solution, where the distance between particles is large enough that the orientation or position correlation is not observed, then *S(q)* = 1, and it has not affected the total scattering intensity. In the case of more concentrated solution, the correlation between particles in sample increases and interference effect between them cannot be neglected. In the low *q*-range, S(q) strongly depends on the interaction potential between particles, and for *q=0, S(0)* is equal to normalized osmotic compressibility. The repulsive interactions indicate the homogenous distribution of particles, *S(0)<1*, although with attractive interaction, fluctuations in particle distribution are observed, *S(0)>1*.[118] The structural factor can be calculated with *Eq.32.*, where *g(r)* is a pair correlation function to describe the probabilities to find particle at the distance r to another particle at *r = 0* .

$$S(q) = 1 + \phi \int_V (g(r) - 1)e^{iqr}dr \qquad \textit{(Eq.32.)}$$

Considering the scattering intensity of sample, which is composed of form and structure factors, the *I(q)* can be described as in *Eq.33.,* where R_{HS} is a hard sphere radius which can be define as the half distance between correlated particles.

$$I(q) = (\Delta\rho)^2 \phi_s V_s \left(\frac{3\,sin(qR_{HS}) - qR_{HS}cos(qR_{HS})}{(qR_{HS})^3}\right)^2 S(q) \qquad \textit{(Eq.33.)}$$

Due to adding the *S(q)* to the equation of *I(q)*, the intensity at the low *q*-value can be reduced by repulsive interactions. Additionally, the possible fluctuations of the particles are reduced as well by limited freedom.

2.3.1.4.1. Percus – Yevick equation

In the case of uncharged spherical particles with potential as in *Eq.34.*, the structure factor can be calculated by Percus–Yevick equation with parameters of R_{HS} and ϕ,[119] where R_{HS} is a half distance between the centers of correlated particles and ϕ is a volume fraction of particles which is an approximation that applies to monodisperse spheres.

$$U_{HS}(r) = \begin{cases} \infty for\ 0 < r < 2R_{HS} \\ 0\ for \quad r > 2R_{HS} \end{cases} \qquad \textit{(Eq.34.)}$$

The *S(q)* of the hard sphere can be expressed as in *Eq.35.*,[120,121] where $C(\phi, A)$ is defined in *Eq.36.* with $A=2qR_{HS}$, $\alpha = \frac{(1+2\phi)^2}{(1-\phi)^4}$, $\beta = -6\phi\frac{(1+\phi/2)^2}{(1-\phi)^4}$ and $\delta = \frac{\phi\alpha}{2}$. The simulated hard sphere structure factors are presented in Figure 12, with half distance between correlated particles of R_{HS} = 60 $\dot{A}$ and series of volume fractions ϕ = 0.05 (blue line), 0.2 (red line) and 0.4 (green line). Position of the first peak, so-called correlation peak, indicates the radius of the hard sphere $R_{HS} = \frac{2\pi}{q_{cp}}$, where q_{cp} is a *q*-value for which is the maximum of the correlation peak. Increase of the ϕ-value causes increasing the amplitude of oscillation at a high *q*-value, thus the distribution of the nearest neighbor become narrower, and the maximum of the peak is slightly shifting to higher *q*-value.

$$S_{HS}(q) = S(q, R_{HS}, \phi) = \frac{1}{1+24\phi\frac{C(\phi,A)}{A}} \qquad \textit{(Eq.35.)}$$

$$C(\phi, A) = \alpha \frac{sin(A) - Acos(A)}{A^2} + \beta \frac{2Asin(A) + (2 - A^2)\, cos(A) - 2}{A^3} + \delta \frac{-A^4\, cos(A) + 4[(3A^2 - 6)\, cos(A) + (A^3 - 6A) sinA + 6]}{A^5}$$

(Eq.36.)

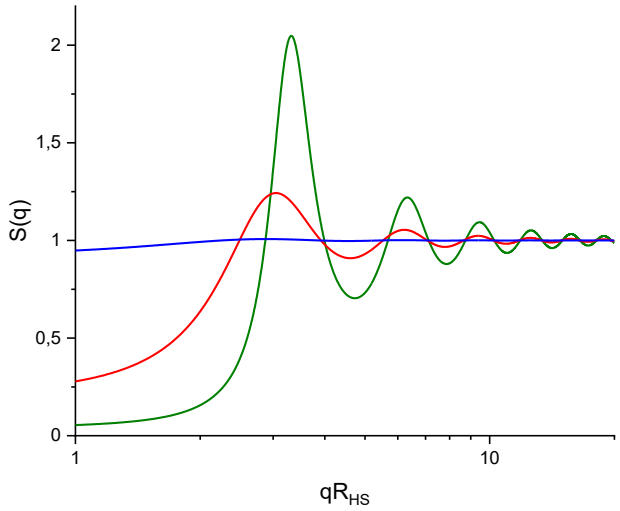

Figure 12. Simulated structure factor for system with R_{HS} = 60Å and three different volume fractions ϕ= 0.01 (blue line), ϕ= 0.2 (red line) and ϕ= 0.4 (green line).

2.3.1.4.2. Fractals

System that contains domains composed of interacting particles, can form a mass fractal structure by e.g., clustering. The mass fractal object creates a 3D network by brunching or crosslinking and can be describe by a Hausdorff dimension, d_f, so-called mass fractal dimension. It is defined as the exponent of linear dimension, r, which accounts for the mass distribution, $M(r) \sim (r/r_0)^{d_f}$, where M represents the mass and r_0 represents the size of the individual particle in the fractal. For a stimuli-responsive block copolymer micelles, value of the d_f, indicates swollen/collapsed state of the polymer. The structure factor for the fractal object can be defined by pair correlation function, which describe the number of particles within the object with a radius r (*Eq.37.*).[122]

$$S(q) = \phi \int_0^r 4\pi r^2 g(r) dr \qquad \textit{(Eq.37.)}$$

Additionally, the fractal object can be characterized by spatial distribution of the individual scattering particles *Eq.38.*, which is a generalization of the Porod law to the

fractal mass dimension, d_f. r_0 relates to characteristic particles dimension and determines the intersection of the extrapolated Porod region with 1, indicates the region where the particle structure becomes important.

$$S(q) = \left(\frac{r}{r_0}\right)^{d_f} \qquad \textit{(Eq.38.)}$$

With description of *g(r)* as in *Eq.39.*, and next performing the Fourier transform, the structure factor of fractal system can be defined as in *Eq.40.*

$$\bar{S}[g(r) - 1] = \frac{d_f}{4\pi r_0^{d_f}} r^{d_f - 3} e^{-r/R_{cluster}} \qquad \textit{(Eq.39.)}$$

Fractal mass dimension is smaller than the dimension of the space where the fractal object is ($d_f < 3$), thus *g(r)* goes to zero for $r \to \infty$, what is unphysical. Therefore, for the large scale of *g(r),* a cut-off function is added $\left(f_{cut-off} = e^{-r/R_{cluster}}\right)$, where $R_{cluster}$ is a cut-off distance for describing the behavior of *g(r)* for a large distance.[122]

$$S_F(q) = 1 + \frac{d_f \Gamma(d_f - 1)}{1 + \left[1/(qR_{cluster})^2\right]^{(d_f-1)/2}} \frac{sin[(d_f - 1)tan^{-1}(qR_{cluster})]}{(qr_0)^{d_f}} \qquad \textit{(Eq.40.)}$$

In general, $R_{cluster}$ represents the characteristic distance above which the mass distribution in the sample is no more described by the fractal law. In practice, it gives the value of the aggregate size or a correlation length in the disordered system.

2.3.1.5. Polydispersity

Choice of the synthesis method for polymer influences on the polydispersity of the final product, and some deviation can be observed from the average length of the polymer chain. Consequently, the size of the particles in the sample will have a distribution of the size, which affect the suppression of the oscillations (smearing) in scattering curve. Therefore, to model the scattering curve with the form factor of sample, such as micelles, the size distribution of the object should be taken, e.g., normal distribution with standard deviation, σ. In Figure 13 is presented the simulated scattering curve for sphere with size R = 60 $\dot{A}$ and three standard deviations, σ = 0.0 (green line), σ = 0.05 (red line) and σ = 0.3 (blue line). As it is shown in Figure 13, with an increase of σ, the minima become smeared, and the forward scattering shifts to higher intensity because of the broader size

distribution of the sphere. The increase of the forward scattering intensity is due to a larger influence on the scattering have larger particles than smaller in the size distribution.

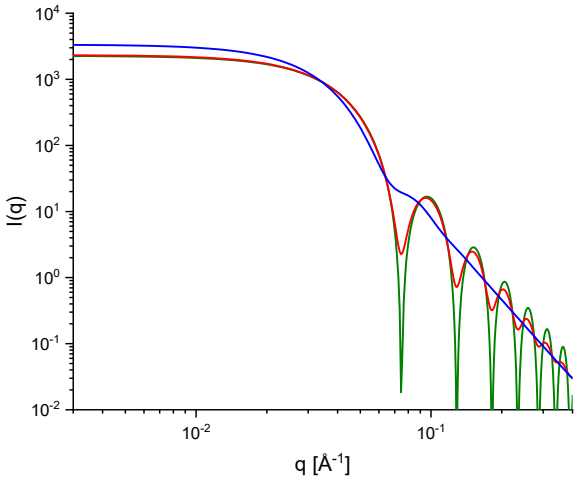

Figure 13. Simulated scattering curve for homogenous sphere and R = 60Å with different standard deviation of the size: σ = 0.0 (green line), σ = 0.05 (red line) and σ = 0.3 (blue line).

2.3.1.6. Kratky analysis

The Kratky analysis is an excellent tool to evaluate sample folding, and the Kratky plot, $I(q)q^2$ versus q, can be calculated directly from the scattering curve. Shape of the curve is used to identify the conformation of polymer chain or protein. For unfolded polymer chain (random coil) or unfolded protein, the shape of the curve does not show any characteristic peak and is observed a rise to plateau at the high q-range (Figure 14, blue line). In the case of folded domains, curve at the Kratky plot gives a characteristic peak, roughly parabolic shaped (Figure 14, purple and red lines). The position of the peak can provide some information about the size of the domain. However, due to dependence on the shape of peak, information about the molecular weight cannot be provided.[123] As shown in Figure 14, the folding density of the polymer domain can be described by curve behavior at the high q-range. For polymer chain, when the curve decreases close to zero, it means that domains are compact, and the difference in SLD between polymer and solvent is sharp. While, for curve that decreases slowly and does not reach zero in $I(q)q^2$, that indicates the polymer domains are partially collapsed. Thus, it contains a lot of solvent. The shape of the characteristic peak can be used to describe the shape of the particles, such as the globular domain shows a narrow bell-shaped peak with a well-defined maximum. Random polymer chain shows a plateau or increase in $I(q)q^2$ at a high q-range, depends on the local rigidity of the chain. The intermediate shape such as worm-like chain can be observed by peak broadening.[124]

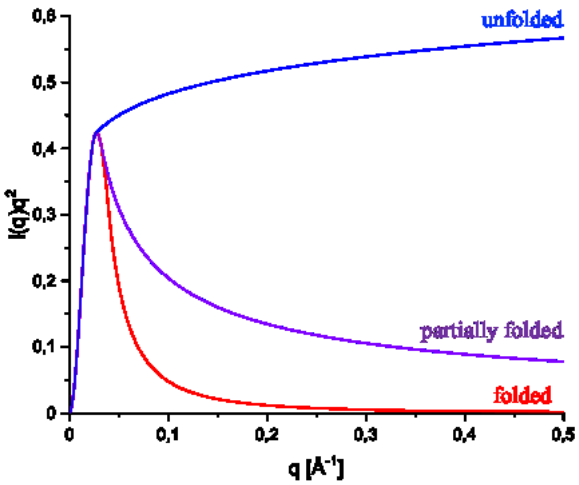

Figure 14. Simulated scattering intensity plotted as a Kratky plot, $I(q)q^2$ vs. q, for swollen polymer (blue line), Gaussian polymer chain (purple line) and dense polymer structure (red line).

Globular object contains smaller particles or different domains can be distinguish with Kratky plot as well. For monodisperse homogenous sphere, the bell-shaped peak is observed at the low *q*-range, and for higher *q*, the oscillations go to zero (Figure 15, red line). For spherical particle contains two different domains, such as core-shell micelle or cluster assembled by partially collapsed sphere, have a characteristic peak at low *q*-range and weak shoulder at higher *q*-range. The bell-shaped peak indicates the object shape and size, however the additional shoulder indicates present of smaller domains with different SLD, such as the micellar core or small spheres in cluster. The position of the shoulder can shift depends on the size of additional domain.

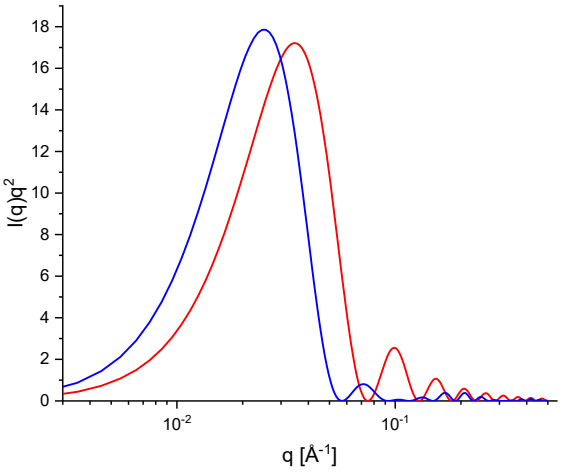

Figure 15. Simulated scattering intensity plotted as the Kratky plot for homogenous sphere (red line) and core-shell sphere (blue line).

2.3.2. Transmission electron Microscopy

Microscopy is one of the methods widely used to characterize small particles with size of micrometers and below this range, to visualize them. Cryogenic transmission electron microscopy (cryo-TEM) is used for characterization of i.a. biological systems,[125,126,127] monodyspersity and morphology of polymeric systems like microgels[128,129,130] and micelles.[131,132,62] This technique allows examining the aqueous samples near to native condition in a frozen state. The sample is directly observed by transmission electron microscope at the temperature of liquid nitrogen.

Transmission electron microscopy is an imaging technique with high resolution, in which the image is produced by passing a beam of electrons through the thin sample. The interaction between electrons and atoms can be used to observe features in sample. TEM works on the same basic principles as optical microscope, but instead of light (photons) electrons are used. The advantage of electron microscopy (EM) compared to light microscopy, is due to the wavelength of electrons. It is shorter than for light thus, the resolution for EM is a few orders of magnitude better.

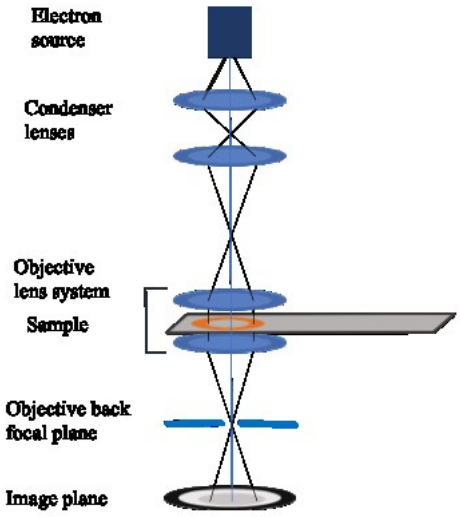

Figure 16. Schematic diagram of transmission electron microscope. The electrons' beam path from electron source (electron gun) through sample to screen (CCD camera or fluorescent screen), where magnified image can be seen.

The electron source creates an electron beam, which is focused into thin, coherent beam by condenser lenses. Condenser apertures eliminate the high-angle electrons. Next, the beam hit the sample and part of the electrons are transmitted further. The amount of them depends on the sample thickness and transparency. The objective lens system is used to focus the transmitted electrons to a magnified image on CCD camera (charge coupled device camera) or on fluorescent screen. Additionally, the objective system can be used to enhance the contrast between features and solvent by eliminating of the high-angle

diffracted electrons. Schematic diagram of the beam path through the microscope is presented in Figure 16. When the electrons pass through the sample, they are scattered by the electrostatic potential created by sample's components. Next, the scattered electrons from one point on the sample are focused on electrostatic objective lens to one point on the image plane.

Preparation of the sample for cryo-TEM imaging is performed by rapid cooling (vitrification) to get as close as possible to the physiological state. A thin film of frozen sample is prepared by solution applying on usually holey carbon-coated EM grid. This can be done by plunge freezing of the aqueous solution to cryogen with good heat-transfer properties, like liquid nitrogen cooled liquid ethane.[133] The thickness of the film should be less than 200 nm.[134] The cooling process of thin sample is rapid, 10^5 °C/s, that ice crystals should not be created thus the vitreous ice layer is amorphous and the structure of the polymer/protein can be analyzed close to their native environment.

3. Results and discussion

3.1.Synthesis and characterization of PNIPAM polymers

3.1.1. Synthesis

3.1.1.1. Linear PNIPAM homopolymers

Linear PNIPAM polymers with controlled molecular weight and narrow molecular weight distribution (PDI) were synthesized by reversible addition-fragmentation chain transfer (RAFT) polymerization. RAFT polymerization engages a conventional free radical polymerization of a monomer in the presence of suitable chain transfer agent (CTA/RAFT-agent).[135] Homopolymer of PNIPAM and copolymer PS-*b*-PNIPAM were synthesized according to the procedure given by Kampermann et al.[136] The synthesis of linear PNIPAM homopolymers were done by one reaction with 2-cyano-2-propyl dodecyl trithocarbonate (CPDT) or 2-dodecylthiocarbonothoylthio)-2-methylpropionic acid (DDMAT) as a RAFT-agent and 2,2'-Azobis(2-methylpropionitrile) (AIBN) as an initiator. The reaction was performed at the temperature of 65.0 °C in 1,4-dioxane for 3h. The polymerization reaction is schematically shown in Figure 17.

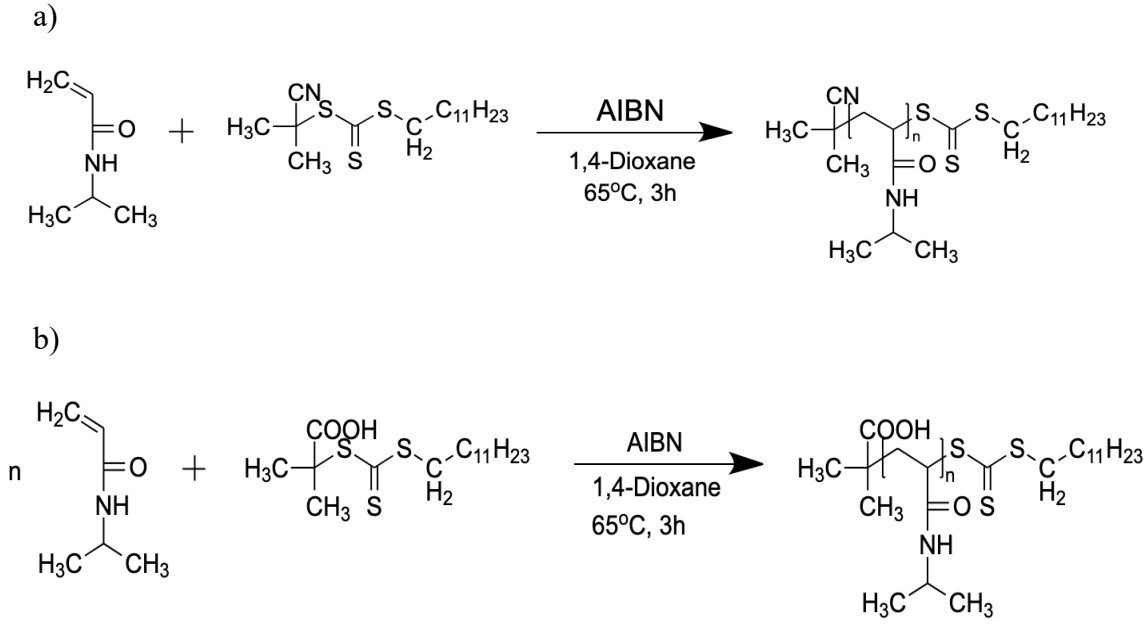

Figure 17. Scheme of PNIPAM synthesis by RAFT polymerization with a) 2-cyano-2-propyl dodecyl trithocarbonate (CPDT) or b) 2-(dodecylthiocarbonothoylthio)-2-methylpropionic acid (DDMAT).

3.1.1.2. Linear PS-b-PNIPAM block copolymers

PS-*b*-PNIPAM-C_{12} block copolymers were synthesized in two-steps. The order of constructing the blocks, in the copolymer, can have influence on the polydispersity of the polymer chain. For the first block formed in RAFT polymerization, the propagating radical should be selected with a good homolytic leaving group with respect to the second block.[137,138] To follow this rule, styrene (St) was polymerized as macro chain transfer agent, with DDMAT as a RAFT-agent, and AIBN as the initiator at 65.0 °C in 1,4-dioxane for 20 h. The second polymeric block, PNIPAM, was added in next reaction where polystyrene with RAFT-agent was used as a macro-CTA and AIBN as the initiator. Solution was prepared in 1,4-dioxane and reaction was proceeded for 3h at 65 °C. The ratio of NIPAM monomer to macro-CTA was 190:1. Both steps are presented on Figure 18.

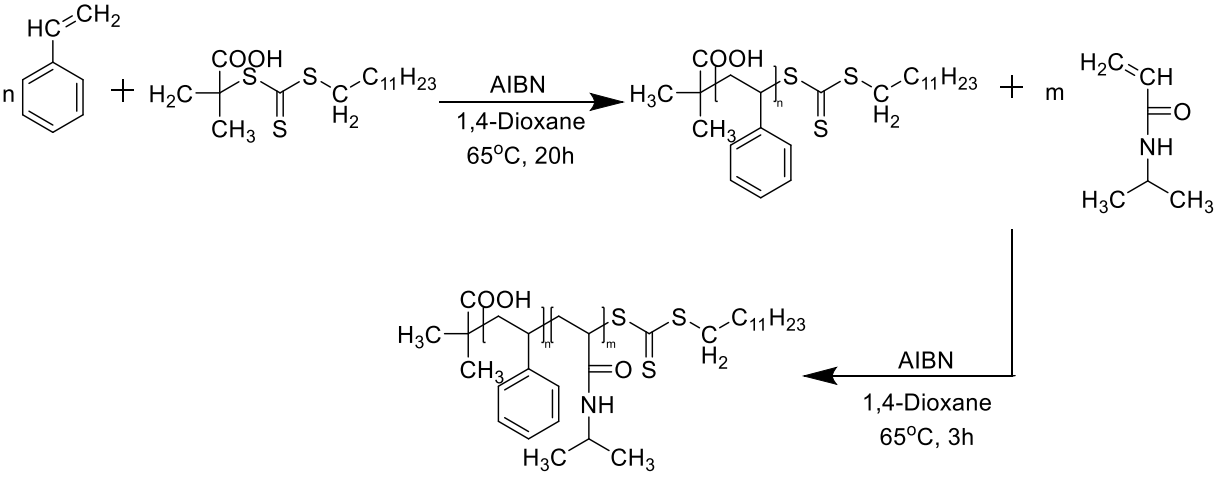

Figure 18. Scheme of block copolymer PS-b-PNIPAM-C_{12} synthesis in two steps by RAFT polymerization.

PS-*b*-PNIPAM-C_{12} aggregats to a gel in aqueous solution with concentration $c \geq 5$ wt % at room temperature. Due to this reason, the n-dodecane chain as an end group in the copolymerchain was substitited by n-butyl acrylate. The substitution was done by amylolysis and Michael addition reaction (Figure 19). The reactions proceed in one pot in two steps. Amylolysis is used to convert the trithiocarbonyl groups into thiols. In the second step, the thiols are transformed into thioesters by conjugate addition with α,β-unsaturated esters.[139] The end group in PS-*b*-PNIPAM-**C_{12}** was changed to n-butyl acrylate (PS-*b*-PNIPAM-**BA**).

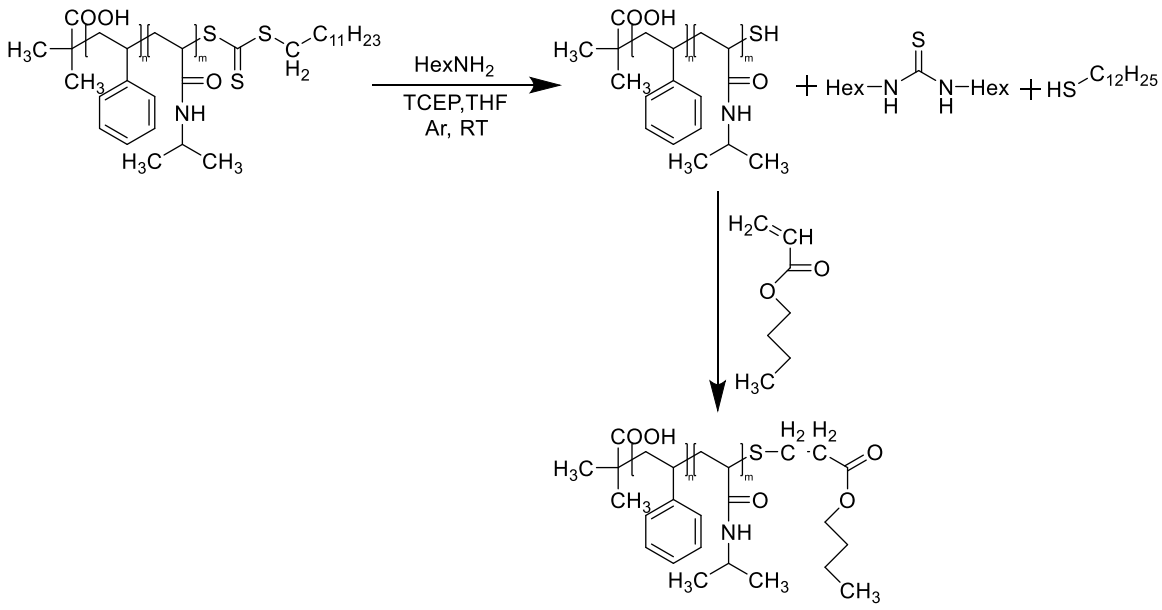

Figure 19. Scheme of substitution reactions in polymer end group by amylolysis and Michael addition reaction.

3.1.2. Polymer characterization

After every step of synthesis, the molecular weight and the distribution of molecular mass were determined by gel permeation chromatography (GPC) and adding individual blocks to polymer chain or changing the end group was checked by nuclear magnetic resonance (^{1}H NMR). The molecular weights of linear PNIPAM-based polymers are presented in Table 1.

Table 1. The molecular weight of polymers.

Name	PNIPAM-97	PNIPAM-95-TTC	PNIPAM-36	PNIPAM-8	PS-*b*-PNIPAM-C_{12}	PS-*b*-PNIPAM-BA
Molecular weight [kg/mol]	96.70	95.60	36.80	8.20	17.0	17.0

3.1.3. Sample preparation

Aqueous solutions of PNIPAM-based polymers were prepared in MilliQ-water (or in deuterated water for SANS experiments) by stirring dried polymer powder with solvent on magnetic stirrer in condition of iced-water in 5–7 days. Later, samples were stored in the fridge (+4.0 °C). Samples were kept at room temperature (T_{RT} = 25.0 °C) at least 30 min before measurements.

3.2. Volume phase transition

3.2.1. Turbidity

The temperature responsiveness of homo- and copolymers were examined by UV-Vis spectroscopy of optical transmission changes, *TR*, for solution with concentration of 10 mg/mL. The measurement performed in temperature range 25.0 °C – 35.0 °C. Figure 20 presents the results for linear PNIPAM homopolymers with two molecular weights, and Figure 21 for PS-*b*-PNIPAM copolymers with different end groups. Turbidity measurement was performed starting from temperature at which PNIPAM is fully swollen (transparent solution) to the temperature, at which is fully collapsed (turbid solution). The polymer with the lowest molecular weight (M_n = 8.2 kg/mol) has a cloud point, $T_{cp,}$ at 30.0 °C, and for polymer, with the highest molecular weight synthesized by RAFT polymerization (M_n = 96.7 kg/mol), T_{cp} is observed at 33.0 °C. Increase of molecular weight causes shifting of T_{cp} by approx. 3.0 °C, and the transition is sharp and abrupt in all cases.

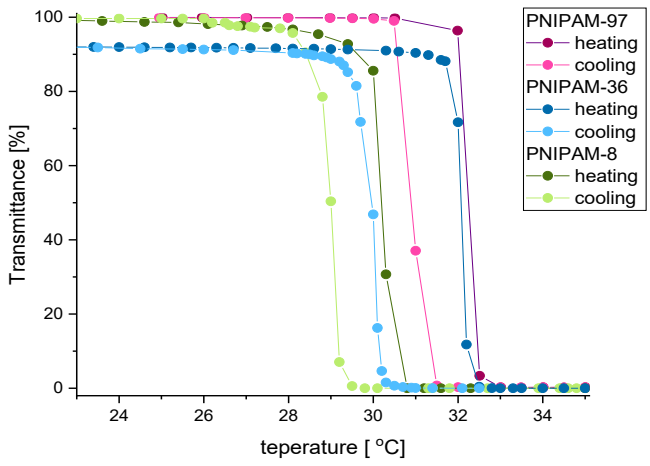

Figure 20. Optical transmission changes as a function of temperature for linear PNIPAM polymers with molecular weight (green) 8.2 kg/mol, (blue) 36,0 kg/mol and (violet) 96.7 kg/mol for heating and cooling process.

The addition of hydrophobic block to polymer chain, changes the responsiveness on the temperature as well, e.g., by shifting T_{cp} below 32.0 °C or influencing the structural changes across LCST. PS-*b*-PNIPAM self-assemble to micelles in aqueous solution. Due to two hydrophobic ends in the polymer chain, short Polystyrene (PS) block and a dodecyl group (-C_{12}), micelles can assemble into clusters with swollen PNIPAM-shell, at the higher concentration. Therefore, the solution is slightly turbid at room temperature. Gradual increase of the temperature in the solution causes slow release of the water from the micellar shell starting at approx. 28.0 °C. Above 32.0 °C, collapsing is more pronounced, thus large domains clouding the solution (*TR* = 0% at 33.0 °C). For copolymer with n-butyl acrylate end group instead of dodecyl group, the solution is transparent below the LCST. Phase transition is observed at 31.0 °C and it is sudden. At 31.5 °C, the solution is turbid and optical transmission is equal to 0%. Modification of the end group in the polymer chain caused self-assembly to single micelles at the higher concentrations, thus networks between them in the swollen state cannot be created, in contrast to copolymer with dodecyl end-group.

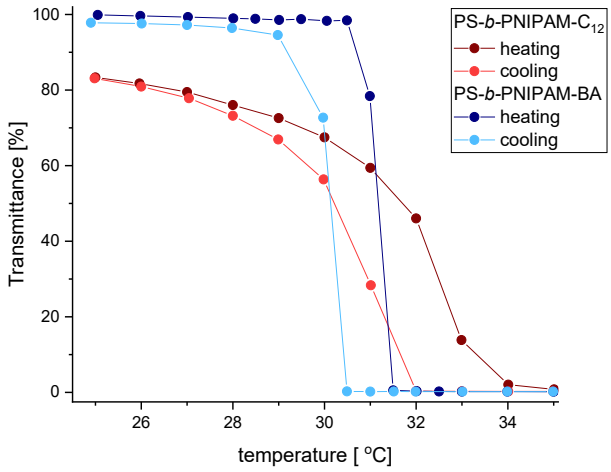

Figure 21. Optical transmission changes as a function of temperature for linear PNIPAM copolymers (red) PS-b-PNIPAM and (blue) PS-b-PNIPAM-BA for heating and cooling process.

3.2.2. Hydrodynamic radius

Monitoring of hydrodynamic radii changes as a function of temperature was done with dynamic light scattering, DLS. The solution was prepared with a concentration of 0.01 mg/mL, to limit the interaction between particles, although for copolymers it was above critical micelle concentration (CMC).[140]

Figure 22 presents the changes of hydrodynamic radii as a function of temperature for linear PNIPAM polymers with different molecular weights, 96.7 kg/mol (purple) and 36.0 kg/mol (blue). At the room temperature, where the polymer is, polymer coils are monodispersed with size of R_h = 45 nm and R_h = 24 nm for PNIPAM-97 and PNIPAM-36, respectively. Upon heating, the size of the coils for PNIPAM-36 stays constant and above 32.0 °C, sharp coil-to-globule transition is observed with further aggregation of the polymer chains (T_{VPT} = 32.0 °C). Size of the globules increases to R_h = 80 nm at T = 35.0 °C and stays constant with further heating. Upon cooling, the globule's size decreases from T = 30.5 °C and at T = 25.0 °C, the coil size returns to the initial value of R_h = 24 nm, where the polymer is fully swollen. In the case of longer PNIPAM chain (PNIPAM-97), when temperature increase, first the coil size decreases from R_h = 45 nm at T = 25.0 °C to R_h = 37 nm at T = 32.5 °C due to water release. Above T = 33.0 °C polymer aggregates (T_{VPT} = 33.0 °C). Upon cooling, two-step de-aggregation is observed. From 33.0 °C to 31.0 °C, the size of the globules increases, by aggregates swelling and, with further cooling, large domains fall apart to single polymer coils. At 28.0 °C the R_h is approx. 45 nm, similarly to the initial point. The longer the polymer chain, the more complex behavior across phase transition temperature and wider hysteresis window.

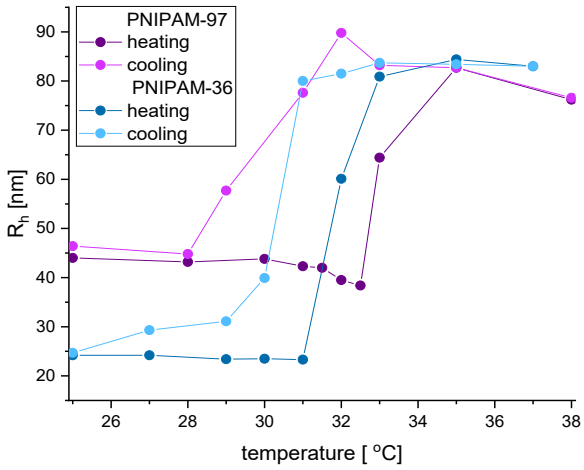

Figure 22. Changes of hydrodynamic radii as a function of temperature for linear PNIPAM polymers with molecular weight (purple) 96.7 kg/mol and (blue) 36.0 kg/mol.

Figure 23 shows the influence of temperature to hydrodynamic radius for PS-*b*-PNIPAM-BA micelles. Single micelles with swollen PNIPAM corona have a R_h = 30 nm. Above T = 28.0 °C, hydrodynamic radius of micelles decreases (R_h = 24 nm) caused by deswelling of the micellar corona. Next, the collapsed micelles form clusters (R_h = 60 nm) due to the volume phase transition (T_{VPT} = 30.2 °C). An increase of the size corresponds to cluster formation by collapsed micelles and next, small decrease of R_h at higher temperature, indicates the further dehydration of the PNIPAM-shell. Upon cooling,

the cluster size first grows significantly from R_h = 60 nm to R_h = 76 nm, due to swelling of the PNIPAM-shell. Subsequently, the hydrodynamic radius gets smaller to R_h = 35 nm at T = 27.0 °C, that means in solution the micelles are at swollen state again.

The cluster formation by collapsed micelles between 30.2 °C and 32.0 °C is a gradual process. Additional experiments at the temperature range 25.0 °C – 30.8 °C (Figure 23a, orange dots) show that the cluster size can be controlled. Equilibration time in the polymer solution is approx. 20 – 30 min after the temperature in the toluene bath reached the set temperature. To estimate the needed time for equilibration of cluster size, the measurement was performed at T = 30.4 °C for 5 h and at T = 30.9 °C for 7 h (Figure 23b). At the first hour, the cluster size increases rapidly, from R_h = 27 nm to R_h = 34 nm at T = 30.4 °C and from R_h = 42.5 nm to R_h = 47 nm at T = 30.9 °C, then the growth of R_h value is negligible. At T = 32.0 °C, the size of the cluster is R_h = 60 nm, thus the maximum size of clusters is not reached for T = 30.9 °C or T = 30.4 °C, even after a few hours. Furthermore, in equilibrium these two temperatures, the hydrodynamic radius of clusters is R_h = 35 nm and R_h = 50 nm. This confirms the stepwise aggregation of collapsed PS-*b*-PNIPAM-BA micelles with a small temperature increase (ΔT = 0.2 °C).

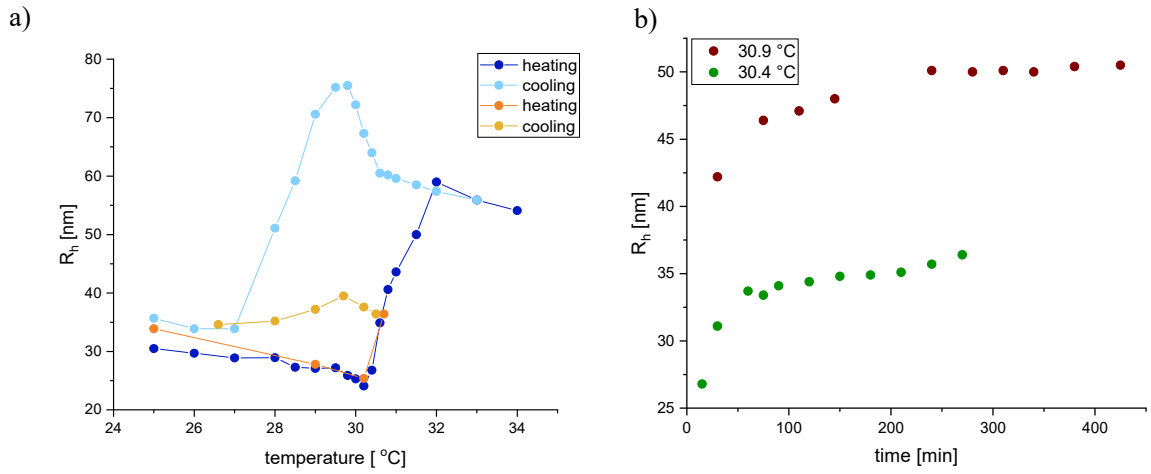

Figure 23. a) Changes of hydrodynamic radii as a function of temperature for linear copolymer PS-b-PNIPAM-BA for temperature range (blue) 25.0 °C – 34.0 °C and (orange) 25.0 °C – 31.0 °C. b) Changes of hydrodynamic radii in time for linear copolymer PS-b-PNIPAM-BA kept at 30.9 °C (dark red points) and 30.4 °C (green points).

The cooling process from a temperature between 30.2 °C and 32.0 °C shows 2-steps behavior: the first, swelling of PNIPAM-shell in the cluster and the second, falling apart into single, swollen micelles. To breakdown the cluster into single micelles, the solution temperature has to decrease a few degrees below T_{VPT}. Therefore, significant hysteresis is observed, ΔT_H = 3.0 °C.

PS-*b*-PNIPAM-C_{12} micelles show similar behavior as PS-*b*-PNIPAM-BA with temperature change across LCST. However, due to the possibility of chemical crosslinking between micelles, R_h of the object in solution is significantly higher than for PS-*b*-PNIPAM-BA in swollen and collapsed states, even in low concentration (Figure 24). In the swollen state at $T = 26.0$ °C, R_h is 40 nm and upon heating, the micelles size slightly decreases to R_h = 29 nm at T = 31.0 °C. Above the volume phase transition temperature (T_{VPT} = 31.0 °C), collapsed micelles form clusters with the size of R_h = 197.5 nm. With further temperature increasing, the hydrodynamic radius stabilizes, and at $T = 38.0$ °C R_h is 209 nm.

In cooling process, the cluster size first increases to R_h = 260 nm at T = 33.0 °C, next between T = 33.0 °C and T = 31.5 °C, hydrodynamic radius significantly grows, indicate cluster swelling. Subsequently, the R_h decreases from R_h = 360 nm at $T = 28.0$ °C to $R_h = 65$ nm at $T = 26.0$ °C. For PS-*b*-PNIPAM-C_{12} broad hysteresis is observed as well, $\Delta T_H = 4.0$ °C, and the larger ΔT_H can be caused by bigger domains form above T_{VPT}, thus lower temperature is needed to breakdown the hydrogen bond between amide group within clusters.

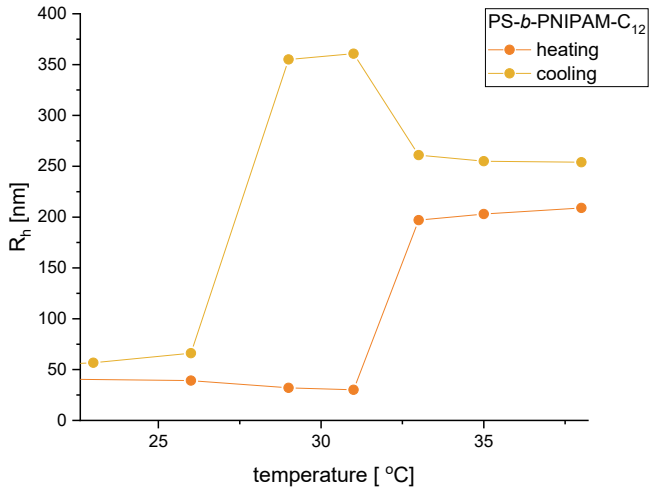

Figure 24. Changes of hydrodynamic radii as a function of temperature for linear copolymer PS-b-PNIPAM-C_{12}.

3.2.3. Polymer morphologies below and above the LCST

The cryogenic transmission electron microscopy (cryo-TEM) was used to determine the morphologies of PNIPAM-based polymers in water below and above the T_{LCST}.

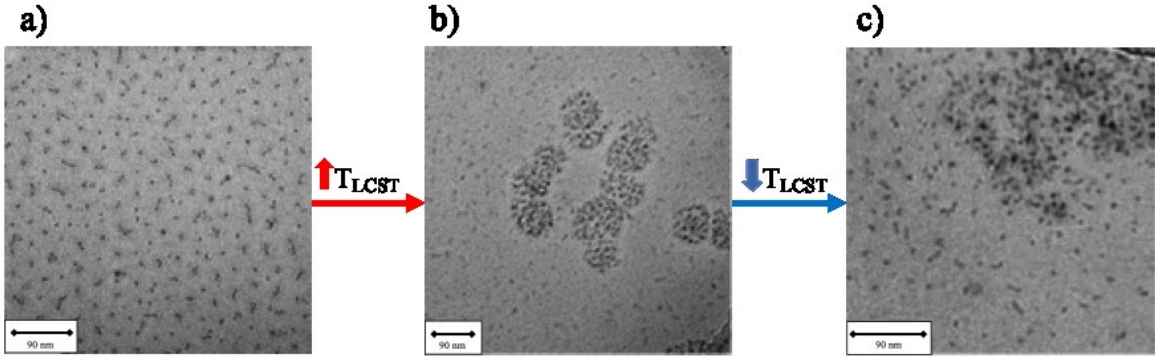

Figure 25. Cryo-TEM images of PS-b-PNIPAM-BA solution at one phase region (a), two-phase region (b) and at the hysteresis range (c).

Figure 25a shows the swollen PS-*b*-PNIPAM-BA micelles in the one-phase state (T = 25.0 °C). The polystyrene micellar core is visible as dense dark grey dots with a diameter of several nanometers (~7 nm). The swollen PNIPAM-shell is less visible than the core, due to the low electron density contrast with water, therefore it is seen as a grey shadow around the PS-core. Clusters formed by collapsed micelles (two-phase state, T = 33.0 °C) are shown in Figure 25b, and partially swollen clusters with irregular shapes close to phase transition point (T = 31.0 °C ± 1.0 °C) are shown in Figure 25c.

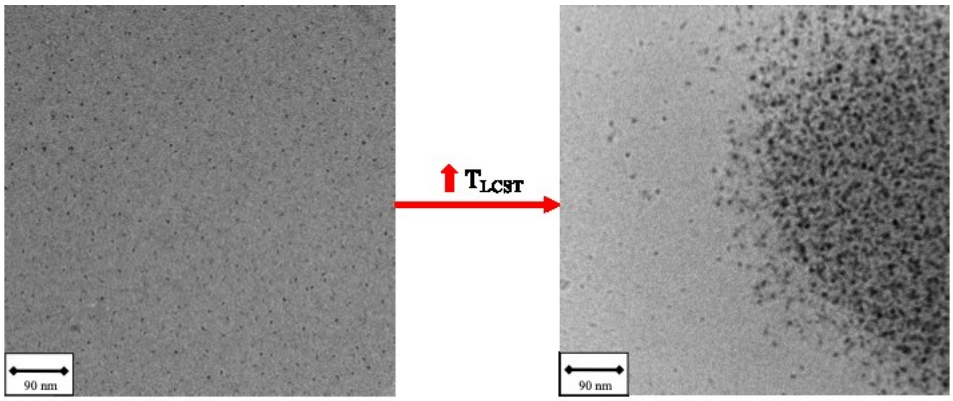

Figure 26. Cryo-TEM images of PS-b-PNIPAM-C_{12} solution at one-phase region (left) and at the two-phase region (right).

Swollen and collapsed micelles of PS-*b*-PNIPAM-C_{12} are presented in Figure 26. On the left, is an image of the sample prepared at T = 25 °C, where micelles are swollen and separated. On the right in Figure 26, is an image of the sample prepared at T = 40 °C, above LCST. At this temperature, single spherical-shaped large domains composed of collapsed micelles were found in the solution. In aggregates, dense PNIPAM shell is better visible, which indicates that the micellar corona contains less water than at T = 25.0 °C.

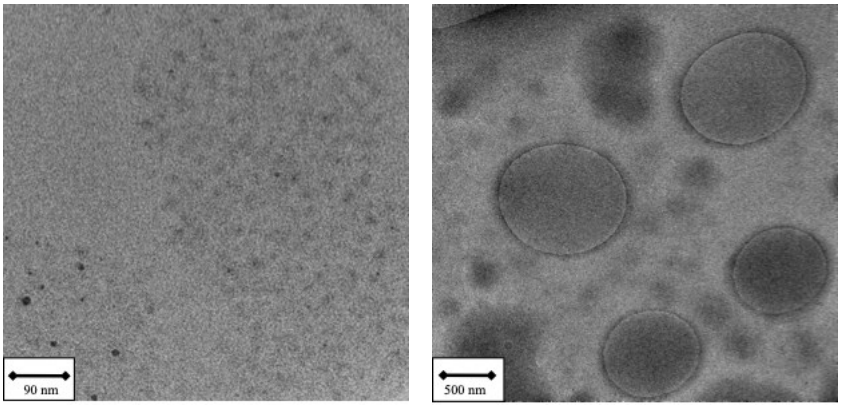

Figure 27. Cryo-TEM images of linear PNIPAM homopolymer solution (PNIPAM-97) at 37.0 °C (above LCST).

Figure 27 shows the collapsed state of linear PNIPAM-97 homopolymer. Polymer above LCST aggregates to large domains with irregular shapes. On the left image of Figure 27, there is a thin layer of collapsed polymer, where the coexistence of dilute and dense PNIPAM microdomains is observed, as well as in PS-*b*-PNPAM micelles above LCST. At lower magnification, large domains of aggregated PNIPAM-97 polymer are observed over a wide range of sizes with irregular shapes (Figure 27, right), which is not the case for PS-*b*-PNIPAM copolymers. Due to low electron density contrast between the solvent (water) and the PNIPAM polymer, at the fully swollen state, PNIPAM-shell or homopolymer PNIPAM was difficult to distinguish.

3.3. Bistability and memory function

3.3.1. Hysteresis loop

For all polymers presented in the thesis, a hysteresis loop is observed with changes in optical transmission and hydrodynamic radii. Significant swelling of the linear PNIPAM homopolymer with high molecular weight and block PS-*b*-PNIPAM copolymer clusters upon cooling is in agreement with observations by Cao et al. [141]

In optical transmission, the hysteresis appears in range of 1.0 °C – 2.0 °C, while in changes of hydrodynamic radii, the hysteresis is wider (2.0 °C – 5.0 °C). Much broader hysteresis in R_h indicates that slightly below LCST the PNIPAM shell is partially swollen, thus the solution is transparent. However, a lower temperature is needed to fall apart clusters to single micelles.

3.3.2. Bistability

Due to clear and sharp hysteresis loop for linear PNIPAM homo- and copolymers, the stability of one-/two-phase state at the hysteresis temperature range was checked by turbidity measurements. The stability of one- or two-phase state at bistability temperature, T^*, was monitored for PS-*b*-PNIPAM-BA solution at T^* = 30.0 °C and PNIPAM-97 solution at T^* = 32.0 °C. Due to sharp phase transition for collapsing and swelling process, T^* was designated in the middle of the hysteresis temperature range for both polymers. The transmittance is close to *TR* = 100% for the swollen (one-phase) state because the solution is non-absorbing, the light scattering intensity of the single polymers or micelles is very low. The collapsed (two-phase) state is characterized by a transmittance close to *TR* = 0 %, because of the intense light scattering of the micellar clusters, which strongly reduces the intensity of the transmitted light when propagating through the solution.

Figure 28a shows the measured transmission as a function of time for the linear PNIPAM-97 solution at the temperature of T^* = 32.0 °C in the one-phase (blue curve) and two-phase (red curve) states. The one-phase state was prepared by heating from 25.0 °C to T^*, while the two-phase state was prepared by cooling from 40.0 °C to T^*. For the one-phase state, the transmittance initially decreases from *TR* = 99 % to *TR* = 88 % in the first 10 hours. Over the next 14 hours, it gradually decreases to *TR* = 84 % and then is constant with fluctuations below 5 %. For the two-phase state, the signal was constant, *TR* = 0 % for 24 h. Therefore, both states are stable over a long time, with the remanent transmission slightly smaller within the one-phase state. This is similar to the remanent magnetization, which is usually smaller than the saturation magnetization.[142,143] Figure 28b presents the optical transmission for the micellar PS-*b*-PNIPAM-BA solution at the temperature of *T* = 30.0 °C for 96 h. In addition, the solution was heated from 25.0 °C to T^*, to reach the one-phase state (blue curve), and from 40.0 °C to T^*, to reach the two-phase state (red curve). For the one-phase state, a long-term stable value of *TR* = 98 % is observed, and for the two-phase state, a stable value of *TR* = 0 % is observed over days with fluctuations less than 3 % in both states.

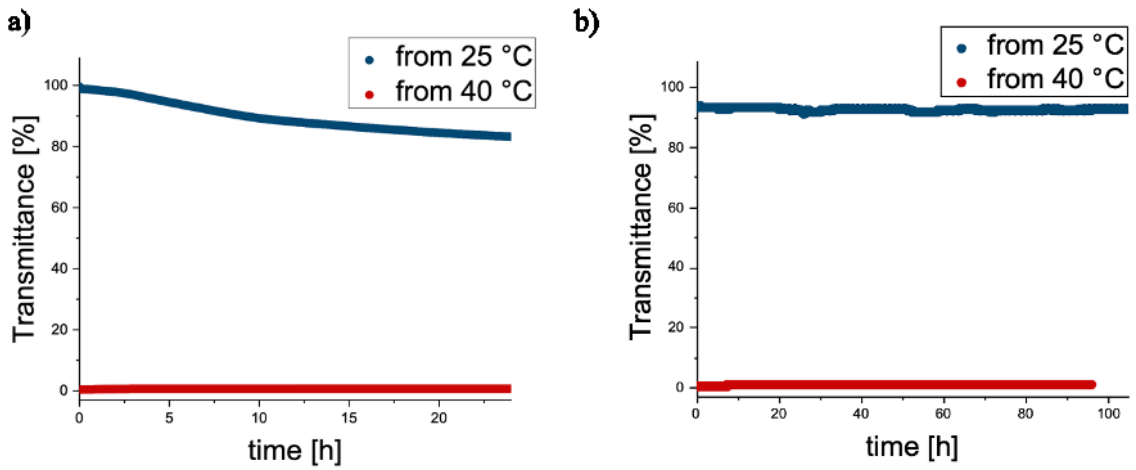

Figure 28. Optical transmission measurement to show the remanence of the one-phase state (blue) and the two-phase state (red) at the temperature in the hysteresis loop, T = 32 °C for linear PNIPAM-97 (a) and T = 30 °C the PS-b-PNIPAM-BA block copolymers (b).

3.3.3. Cluster formation and swelling

A stable two-phase region below LCST and the stepwise cluster formation is of central importance for the hysteresis and bistability behavior. Hence, a detailed cryo-TEM study was performed, focusing on the hysteresis temperature range. The sizes of micelles or clusters obtained from cryo-TEM are in good agreement with the hydrodynamic radii. The detailed analysis by cryo-TEM compared with DLS results are presented in Figure 29. In the heating/cooling cycle, the polymer solution at each region was equilibrated at the given temperature and then vitrified by applying sample on a carbon grid and plunging it into liquid ethane.

The cryo-TEM image, for the sample prepared at $T = 25.0$ °C, shows single swollen micelles with a diameter of approx. 30 nm. The dark grey dots represent the PS-core, and the light grey shadow is the PNIPAM-shell. By increasing the temperature close to the phase transition point, the PNIPAM-shell becomes smaller and more prominent, darker. Moreover, the size of dark dots, representing the micellar core, increases indicating dehydration of the PNIPAM layers close to the PS-core. Above the LCST, collapsed micelles assemble into clusters with a diameter of approx. 100 nm. Collapsed micelles can be easily recognized within the clusters. The PNIPAM-shell is darker than in the image with the sample prepared at $T = 25.0$ °C, which indicates polymer thickening by removing water from the micellar corona. In the clusters, the compact dark grey PNIPAM domains are microphase separated from swollen light grey PNIPAM domains. The coexistence of dilute and dense PNIPAM-microdomains corresponds to the coexistence of dilute and dense macrophases in classical binary phase diagrams. In the aqueous solution of PS-*b*-PNIPAM-BA, micellar clusters are stabilized by charged end groups. They provide

electrosteric stabilization, limiting further aggregation that would eventually lead to macrophase separation. When the PS-*b*-PNIPAM-BA solution is heated above LCST, the clusters aggregate to larger spherical domains what is not observed by DLS due to the higher concentration of solution used for the cryo-TEM imaging.

Upon cooling, the aggregates first swell, which is observed by increasing the PS-core to core distance and forming irregular and expanded cluster domains. With further cooling of the polymer solution, single micelles and small micellar multiplets are observed. The dark PS micellar cores can be distinguished from the light grey swollen PNIPAM shells. Thus, the one-phase state is reached again. The average radius of the multiplets is 30 – 40 nm.

The transition from one-phase to two-phase state proceeds in two steps:

1) collapse of the PNIPAM polymers at the temperature close to LCST,
2) subsequent aggregation into microphase separated domains above LCST.

The reverse transition, from two-phase to one-phase state can be described in two steps as well:

1) swelling of large domains,
2) a breakdown into single micelles upon cooling the polymer solution.

Similarities can be found in the magnetization state transition of ferromagnetic materials, which is also a two-step process,[144,61] including:

1) fast local rotation of the magnetization direction in the domains,
2) the slow (irreversible) increase/decrease of domain sizes, occurring by the movement of domain interfaces.

In both cases, hysteresis involves a local process → swelling/collapsing or change of magnetization direction, and a larger-scale process → aggregation/de-aggregation or domain size increase/decrease. For ferromagnetic materials, this causes the hysteresis that is necessary for information storage.[145]

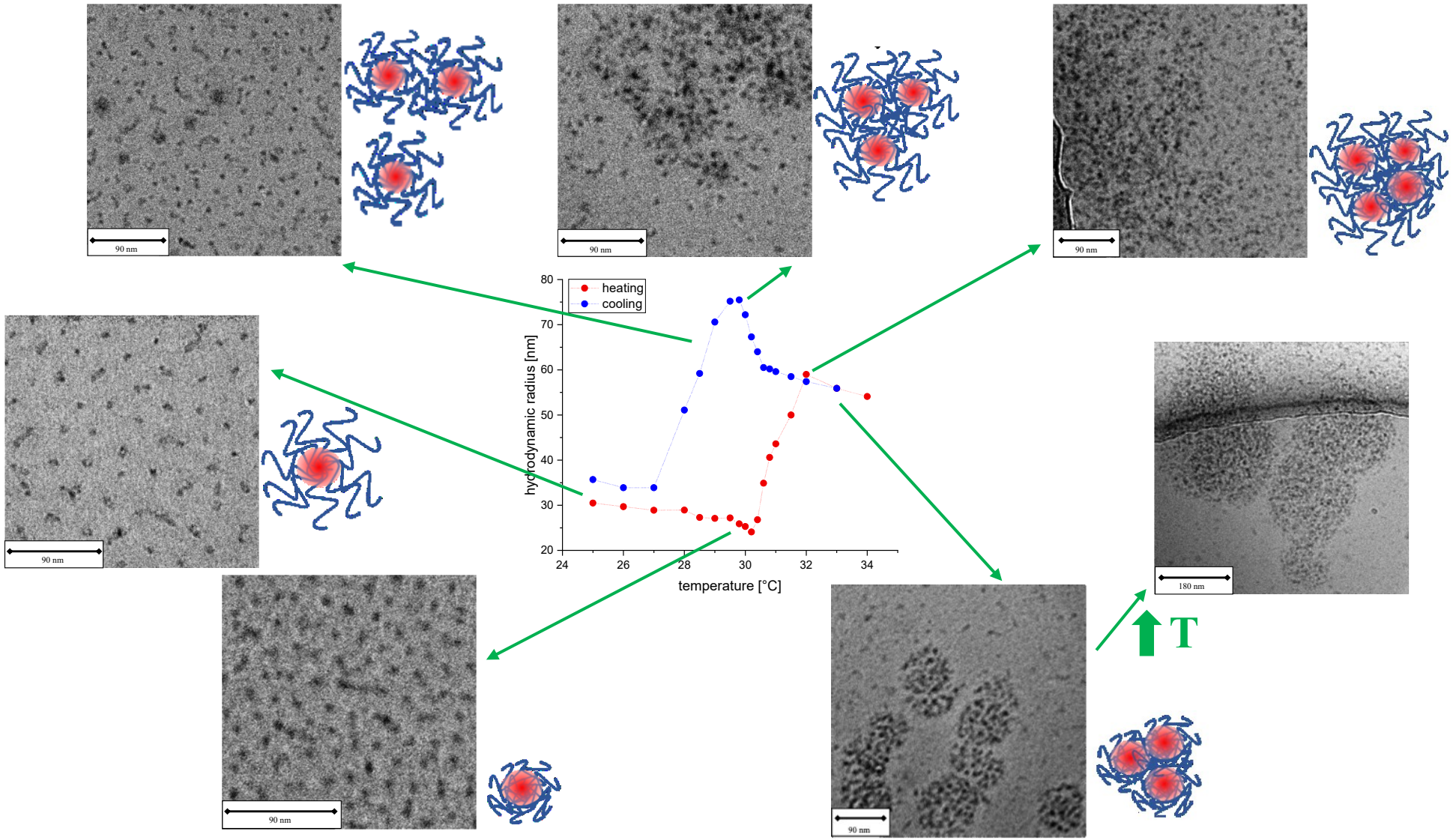

Figure 29. Micellar size dependence on temperature monitored by dynamic light scattering and cryo-TEM imaging. The measurements were done across LCST with small steps of temperature changing in the hysteresis range.

3.3.4. Locally induced phase transition

Remanence is a condition for bistability and information storage. In the case of magnetic information storage, a magnetic field is applied very close to the thin magnetic layer. Then the field is locally larger than the coercivity field to reverse the magnetization direction, thus changing the magnetic state. For thermal information storage within the bistability region of a thermo-responsive polymer, there are similarities. A temperature outside the coercivity temperature is locally applied to a thin layer of a polymer solution at its temperature within the hysteresis range, T^*.

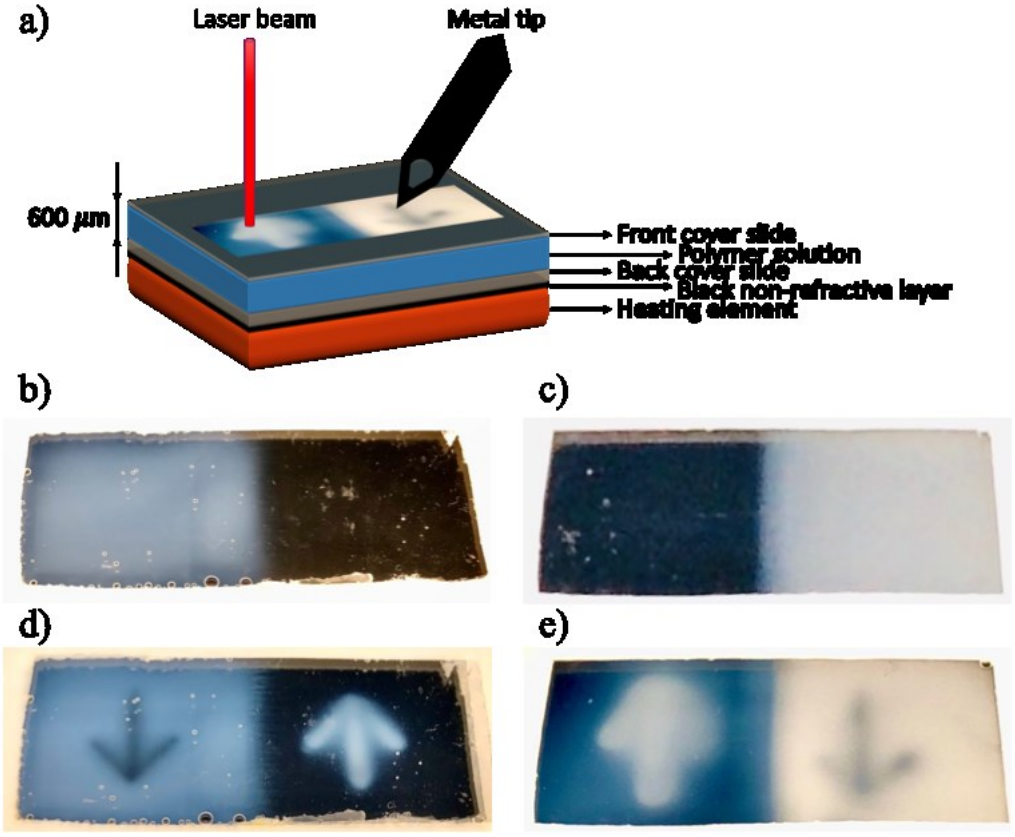

Figure 30. a) Scheme of the thin layer backscattering device (TLBS-device) used for thermally write and read information by laser or a metal tip. Peltier element kept the polymer solution at T. In the initially bright and dark states (b, c) of solutions of the linear PNIPAM-97 homopolymer (left images) and the PS-b-PNIPAM-BA block copolymer (right images) dark arrows in a white matrix are written using a cold metal tip, and white arrows are written into a dark matrix using a hot metal tip (c, d).*

Figure 30 b – c show images of TLBS-devices in ambient light at T^*. Figure 30b shows the image of the PNIPAM-97 solution, where the left half of slide is with the solution at two-phase state (it is white) due to cooling from 35.0 °C to the bistability temperature. The right half is in one-phase state (transparent so the black background is visible) because

the solution was heated from 25.0 °C to T^*. Likewise, Figure 30c shows a photograph of the PS-*b*-PNIPAM-BA solution, where the left half of the slide is in one-phase state by heating from 25.0 °C to T^*, and the right half is in two-phase state by cooling from 35.0 °C to T^*. Both states can coexist at bistability temperature and are stable in days with a sharp boundary that separates them. Figure 30 d–e show the photographs of TLBS-devices in ambient light at T^* after writing. A metal tip with a lower or higher temperature that hysteresis temperature range was used for the writing process. The cold metal tip was used to write on the solution at two-phase state. After contact of the cold tip with the cover slide of TLBS-device, the polymer solution goes from two- to one-phase state, and thus the white state becomes a dark state due to swelling of the polymer at the contact points. Hot tip drives the polymer solution from one- to two-phase state, thus the dark state becomes white due to aggregation of the polymer at the contact points. Figure 30d shows that on the PNIPAM-97 solution, a dark ↓ arrow symbol can be written on a white display field by the cold tip, corresponding to two- to one-phase transition. The hot tip can be used to write a white ↑-arrow symbol on a dark display field corresponding to a one- to two-phase transition. In the case of PS-*b*-PNIPAM-BA solution (Figure 30e), similarly to PNIPAM-97, a white ↑-arrow symbol can be written on left dark field, and a dark ↓ arrow symbol can be written on right white field. It is possible to change the state of the PNIPAM-based polymers locally and it can stay constant with sharp boundaries between states for days at their bistability temperatures. The images in Figure 31 and Figure 32 show the long-term bistability for PNIPAM-97 and PS-*b*-PNIPAM-BA, respectively. The TLBS-device demonstrates writing and reading information employing the intrinsic bistability of the thermally responsive polymers. Heating the whole device to temperatures above the hysteresis temperature range or cooling below it, the information can be erased.

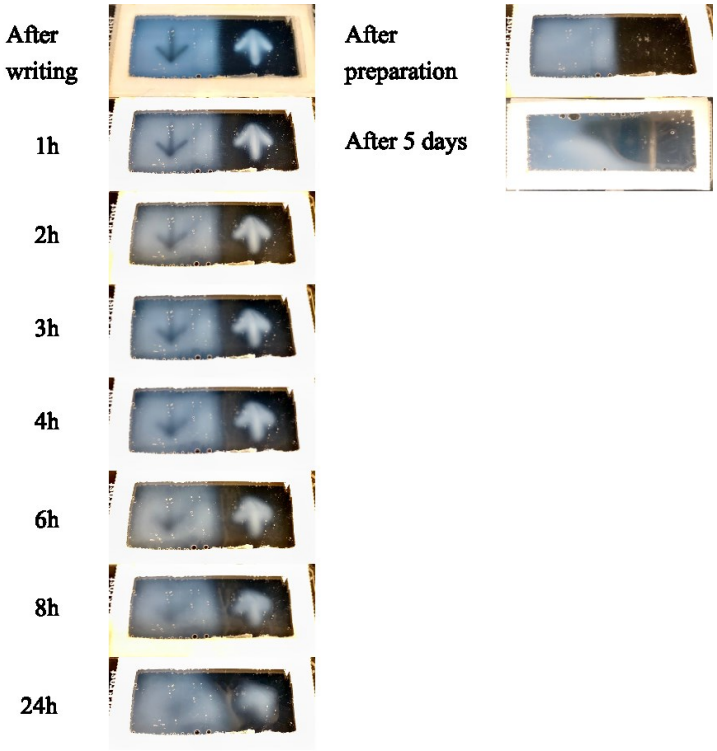

Figure 31. Writing experiment with long time observation for linear-PNIPAM-97 polymer. Observation was performed for 24 h, at T^* = 32 °C. Solution half turbid-half transparent were kept 5 days on the Peltier element to check stability of both stages for longer time.

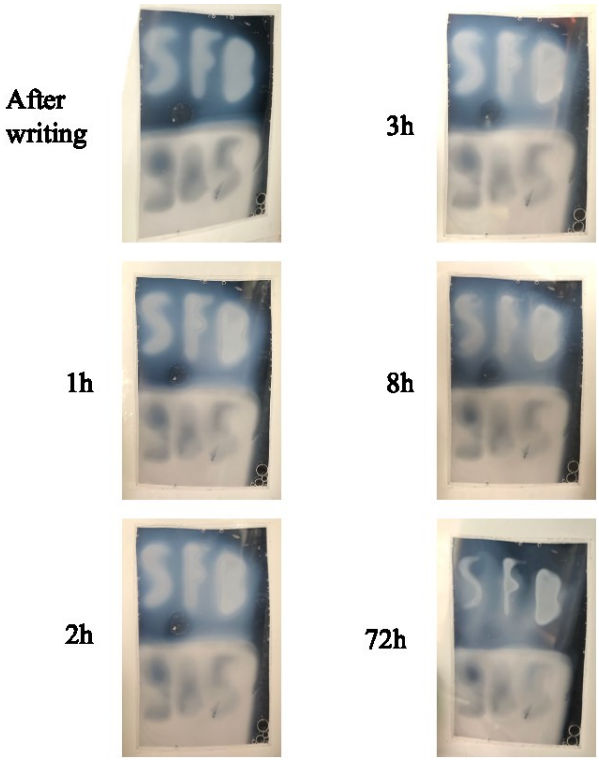

Figure 32. Writing experiment with long time observation for PS-b-PNIPAM-BA copolymer. Observation was performed for 72 h at T^* = 30.0 °C.

Results and discussion

Thulium NIR-laser was used to achieve faster writing of feature with smaller size on polymer solution. The absorption coefficient of water in the visible spectral region is approx. 0.001 cm^{-1} at room temperature,[146] whereas in the NIR spectral region at a wavelength of 2 µm it is 100 cm^{-1},[147] thus five orders of magnitude higher. The corresponding water penetration depth, over which NIR-radiation is completely absorbed, is in a range of a few hundred micrometers. Therefore, thin layers of polymer solutions as in the TLBS-device are well suitable for writing information. To make a pattern on the polymer solution, the NIR-laser beam was passed through an aperture with array of hexagonally arranged spots as shown in Figure 33a and Figure 33b. The diameter of the spots is 1 mm, separated by 0.5 mm. Initially, the polymer solutions were in one-phase state due to heating from room temperature to T^* (T^* = 30.0 °C for PS-*b*-PNIPAM-BA and T^* = 32.0 °C for PNIPAM-97), from which the *T*-jump was performed. The laser pulse energy was $E_{laser\ pulse}$ = 250 mJ with exposure time of $t_{laser\ pulse}$ = 5 ms thus at the illumination spot, the temperature jump is approx. +5 °C.

At the illuminated spots on sample, the temperate increased above LCST, thus the phase transition was observed from one- to two-phase state. The backscattering intensity increased at those spots by change the solution from transparent to turbid. The writing speed and spatial resolution was followed by high-speed camera (HSC) with frame frequency of 1000 fps. The heating time for liquid water is in the range of ~ 10 nanoseconds, thus in milliseconds time scale the aqueous solution has long reached its high temperature plateau in the two-phase state.

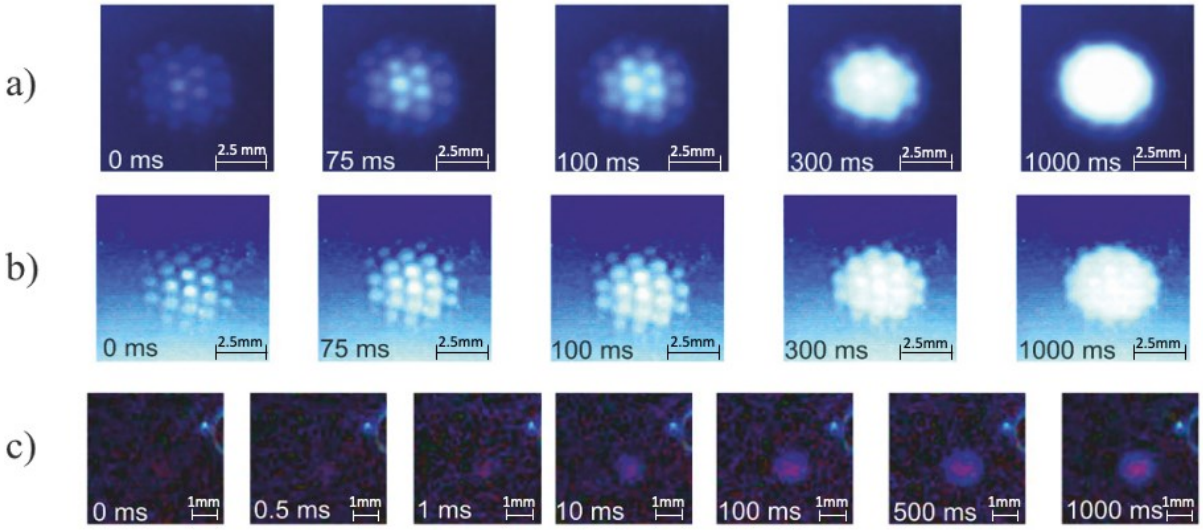

Figure 33. Temporal evolution of a hexagonal spot pattern written into the backscattering display using a 5 ms pulse (250 mJ) of an NIR-laser at times of 0, 75, 100, 300, and 1000 ms after the pulse for the a) linear PNIPAM-97 homopolymer solution and the b) PS-b-PNIPAM-BA block copolymer solution. Individual spots have an initial diameter of 1 mm.

By reduction of the pulse duration (0.5 ms) and the pulse energy (7.5 mJ) the display spot size can be confined to the 1 mm laser spot size (c) for PNIPAM-97 solution.

Figure 33a and Figure 33b show a series of snapshots recorded by HSC, at different times after laser pulse for linear PNIPAM-97 and PS-*b*-PNIPAM-BA aqueous solutions, respectively. After the laser pulse is switched off, a hexagonal array is observed of bright 1mm-spots with sharp and well-separated edges. Over 100 ms, the spot intensities increase and spread into the surrounding domains. Subsequently, the spots merge and create one large spot, corresponding to NIR-laser beam with diameter of 5 mm.

The information on polymer solution can be written by NIR-laser beam with laser pulse of 5 ms and stay at longer time at T^*. After laser pulse, the two processes are observed, where the spot intensities increase and spread in solution. Increase of intensity is caused due to the large domain formation of collapsed polymer by cluster-cluster aggregation. This occurs in time range of sub-seconds in the case of linear homo- and copolymer systems. The spreading intensity is caused by thermal heat diffusion from heated spots to local surrounding solution, which represents the transition from dark (one-phase) to bright (two-phase) state. Heat diffusion distances can be estimated from the thermal diffusivity of water at 30.0 °C, which is $D_T = 0.148 \cdot 10^{-6}$ m^2/s.[148] After time of t = 100 ms, the mean square diffusion length[149] is equal to $r = \sqrt{6 D_T t} = 240$ µm, which well corresponds to the observed spreading from spots. Summarizing, the spots in millimeter size range can be written on polymer solution within milliseconds and during hundred milliseconds the final backscattering signal will be fully develop. The spatial resolution is limited by thermal diffusion, similarly such as in many lithographic processes.[150]

Reducing the illumination time and laser spot size can minimize the blurring effects of heat diffusion. With the laser beam size changed to 1 mm by a lens and shorten the laser pulse to 0.5 ms with the energy of $E_{laser\ pulse}$ = 7.5 mJ, the absorbed heat is reduced to sufficient for one- to two-phase transition (Figure 33c). Lower energy of laser pulse does not lead a persistent phase transition. In that case, the backscattering intensity initially increases, and subsequently decreases back to zero. The spatial resolution can be reduced by decreasing illumination energy to a minimum to induce the phase transition by crossing the coercive temperature. Variation of laser pulse energy, exposure time and sample thickness are described in detail in section 3.6.2.

3.3.5. Non-erasable memory

In the case of magnetic storage devices, the stored information is remanent since the device is kept at external magnetic fields below the coercivity field strength. For the thermo-responsive polymer, the stored information is saved since the temperature is kept

withn its hysteresis temperature range, ΔT^*. When the temperature increases above this range, then the polymer solution switches from one- to two-phase state completely. Within cooling below ΔT^*, the transition from two- to one-phase state is observed. Heating or cooling of the system beyond the ΔT^* erases all stored information in solution.

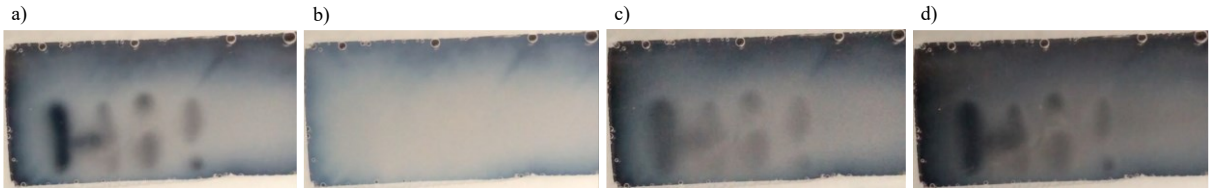

Figure 34. Unusual invisible remanence of the encoded information 'Hi!'. The information is written on PNIPAM-97 solution at T^* = 32.0 °C (a) and becomes invisible when heating to T = 40 °C, above the coercive temperature (b). Surprisingly, the information reappears after cooling back to T^* (c – when the T>ΔT^*, d – after reaching T^* and equilibrate).

Interesting memory behavior was observed for the linear PNIPAM-based polymers where the written information was not erased. After writing on the polymer solution at two-phase state by a cold metal tip, the information is saved at T^*. When the temperature of the heating device is cooled below ΔT^*, the information was erased, and after heating to T^*, the system stayed at one-phase state completely. Similar behavior was expected, when the same system with information written by the cold tip, was heated up above ΔT^*. Nevertheless, after returning to T^* from high temperature, the earlier saved information appeared again. Figure 34 shows the invisible/visible cycle of information "*Hi!*" written by the very cold tip on the linear PNIPAM-97 solution at two-phase state depends on the temperature of the polymer solution. The temperature of the TLBS-device at the writing was T^* = 32.0 °C. The written information becomes invisible when the system is heated to T = 40.0 °C, and the whole solution display homogeneous and bright backscattering indicating information erasure that is shown in Figure 34b. With slow cooling down of the system to T^*, the solution stays at two-phase state however, the information begins to appear (Figure 34c). After reaching the T^*, the sign "*Hi!*" is visible again very well, shown in Figure 34d.

Copolymer PS-*b*-PNIPAM-BA shows also the non-erasable memory behavior. Figure 35a shows the polymer solution is in an equilibrated state at T^*, which is fully in two-phase state. In Figure 35b, the information is saved by writing the " ☺ " sign, and next the solution is heated up to T = 37.0 °C. As is shown in Figure 35c, the solution goes fully to two-phase state. However, the polymer solution is not homogenous in the device and the written sign can be seen as brighter, white points. Figure 35d show that decreases of temperature to T^*, the information begins to appear and when T^* is reached, the sign is visible. Although the polymer is not completely swollen as well as directly after writing (Figure 35e). Additionally, the direct contact between very cold tip and slide can be pointed

very well, and how far the low temperature diffuses from cold tip can be also recognized by a lighter shadow around the information.

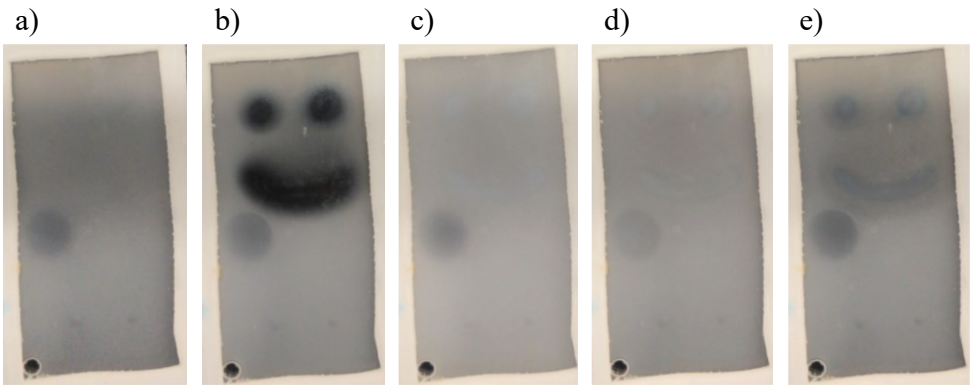

Figure 35. PS-b-PNIPAM-BA solution at the bistability temperature in two-phase state (a). The information "☺" is written at T^* = 30.0 °C (b) and becomes invisible when heating to T = 37.0 °C, above the coercive temperature (c). Surprisingly, the information reappears after cooling back to T (d – when $T = T^*$, e – after reaching T^* and equilibrate).*

The invisible/visible cycle can be repeated many times in a wide temperature range above ΔT^*. The mechanism for 'invisible memory' storage is currently not completely clear. It appears during rapid cooling across the volume phase transition. Clusters with polymer/polymer- or polymer/glass hydrogen bonds are trapped in states that do not undergo hysteresis. When the solution is heated above LCST, clusters are in an aggregated state, and thus the corresponding device area appears bright within a bright matrix. With cooling to T^*, the non-hysteretic clusters return to one-phase state, whereas all other clusters remain in the two-phase state. In that, written information appears black again, within a white matrix. It was found that, with keeping the solution at 50.0 °C for one hour, the information reappeared for 5 – 6 cycles. The information can be erased by keeping the solution at a high temperature in a two-phase state for more than 12 h. If the lifetime of this state could be increased, it would allow for storage of information in visible and invisible states.

3.3.6. AND logic gate function

If the bistable state can be switched in addition by other variable such as pH, it would enable a logic gate functionality. Figure 36 shows that for the TLBS-device an AND logic gate function can be implemented with the temperature and the pH as inputs, which both define the backscattering intensity I_{BS} as the output. When the temperature is below LCST, e.g., at $T = 20.0\ °C < T^*$, the polymer system is in the one-phase state, backscattering intensity I_{BS} is low, and the device is in dark state (0). When the temperature is above LCST,

e.g., at T = 40.0 °C > T^*, the polymer system is in the two-phase state, backscattering intensity I_{BS} is high, and the device is in a bright state (1). This single input system corresponds to a simple 'YES'-logic.

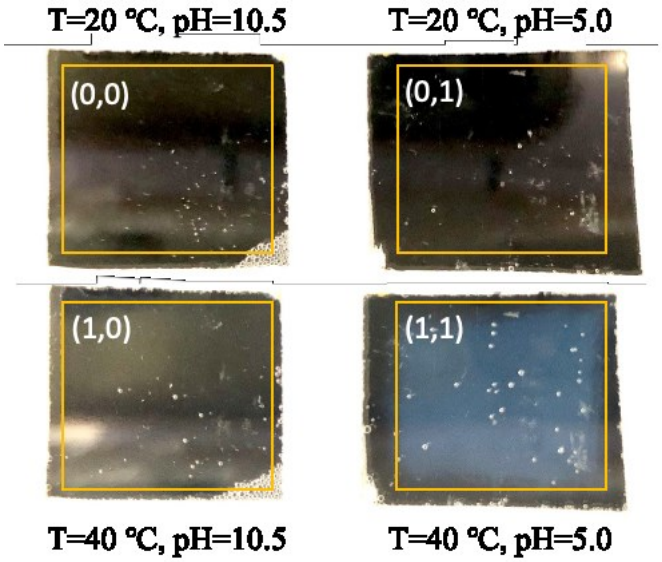

INPUT		OUTPUT
T	pH	I_{BS}
0 T < T_{VPT}	0 pH > 7	0 low
0 T < T_{VPT}	1 pH < 7	0 low
1 T > T_{VPT}	0 pH > 7	0 low
1 T > T_{VPT}	1 pH < 7	1 high

Figure 36. AND logic gate functionality with images of the device brightness for different temperature and pH input states (left) and the corresponding table (right). For the input states $T > T_{VPT}$ (1) and pH < 7 (1) the device is in its bright state (1) with a bright back scattering signal I_{BS} at the temperature T, in other cases the device is in dark state (0).*

Changes in the pH do not affect the volume phase transition temperature or the hysteresis. However, this affects the size of the clusters in the two-phase state, thus the intensity of backscattering. Linear PNIPAM homopolymers with carboxylic end groups were used to check pH responsiveness. At low pH-values, the end groups are protonated and in the uncharged form (-COOH), enabling cluster aggregation. High pH-values, end groups are deprotonated and in the charged form ($-COO^-$), suppressing cluster aggregation.

Combining both inputs, temperature, and pH, the AND logic gate with PNIPAM polymer solution can be designed as is shown in Figure 36. At a temperature of T = 20.0 °C and pH =10.5, the input state is (0,0) and the backscattering intensity, I_{BS}, is low. Therefore, the TLBS-device in the 0-state. At T = 20.0 °C and pH = 5.0 the input is in the (0,1)-state, where I_{BS} is low and in the 0-state. In the case, where T = 40.0 °C and pH = 10.5, the device is in (1,0)-state, and the backscattering intensity I_{BS} is low, thus in the 0-state. Only for T = 40.0 °C and pH = 5.0 corresponding to the (1,1)-state, the backscattering intensity is high and the TLBS-device in the bright state (1). The binary values corresponding to the temperature, pH and backscattering intensity states are summarized in the corresponding table in Figure 36. This demonstrates AND-logic gate functionality, which can be switched by temperature and pH-changes and be stored in the hysteresis window.

3.4. Responsiveness monitoring for temperature and pressure of PNIPAM-shell in the micelles

The linear block PS-*b*-PNIPAM copolymers self-assemble to micelles in the water. The morphology and the size of domains of the polymers were distinguished by cryo-TEM imaging and DLS in previous sections. Micelle consists of the hydrophobic PS-core and hydrophilic PNIPAM-shell. The micellar core size is independent of the temperature. The micellar corona consists of a thermo-responsive polymer. The small-angle neutron scattering was used to study the morphology of the PS-*b*-PNIPAM copolymers in semi-dilute solution and to monitor the PNIPAM-shell changes on temperature.

3.4.1. PS-core size determination

Due to low electron density contrast between PNIPAM-shell in swollen state, size of the PS-core was determined by small angle X-ray scattering (SAXS). For that, experiment was performed for PS-*b*-PNIPAM-BA aqueous solution with concentration of 10 mg/mL at temperature of T = 25.0 °C. The SAXS-curve with best fit is presented in Figure 37, where two shoulders are observed that indicates core-shell structure.

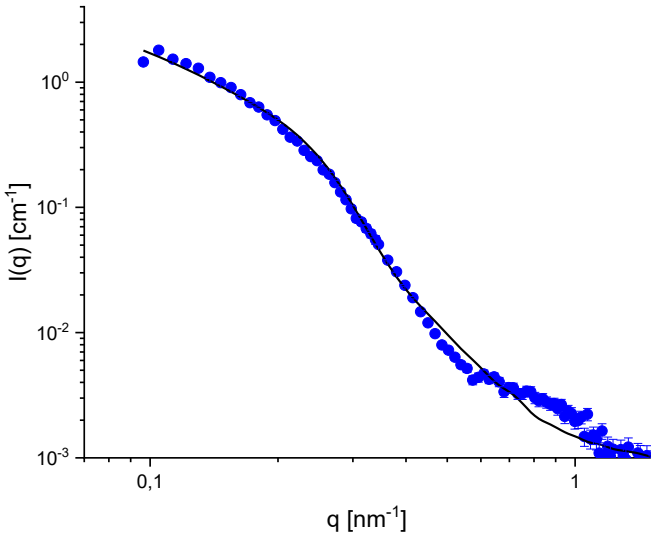

Figure 37. SAXS curve of PS-b-PNIPAM-BA solution (blue dots) with concentration of 10 mg/mL at room temperature (T = 25.0 °C) with its best fit (black line).

To get a detail information about the structure, SAXS curve was fitted with function from *Eq.29*., that contributes the form factor for core-shell sphere which describe the size of the PS-core and thickness of the PNIPAM-shell. Results from modeling shows that the R_{core} = 5.32 ± 0.05 nm and R_{shell} =24.9 ± 3.5 nm.

3.4.2. PNIPAM-shell shrinking and cluster formation upon heating

To characterize the internal morphology of the micelles and further cluster formation across LCST, SANS measurements were performed at the temperature range of 25.0 °C – 35.0 °C. Due to differential scatter of hydrogen and deuterium and low electron density of PNIPAM, neutron scattering is a good technique to follow changes of micellar PNIPAM-shell as a function of temperature.

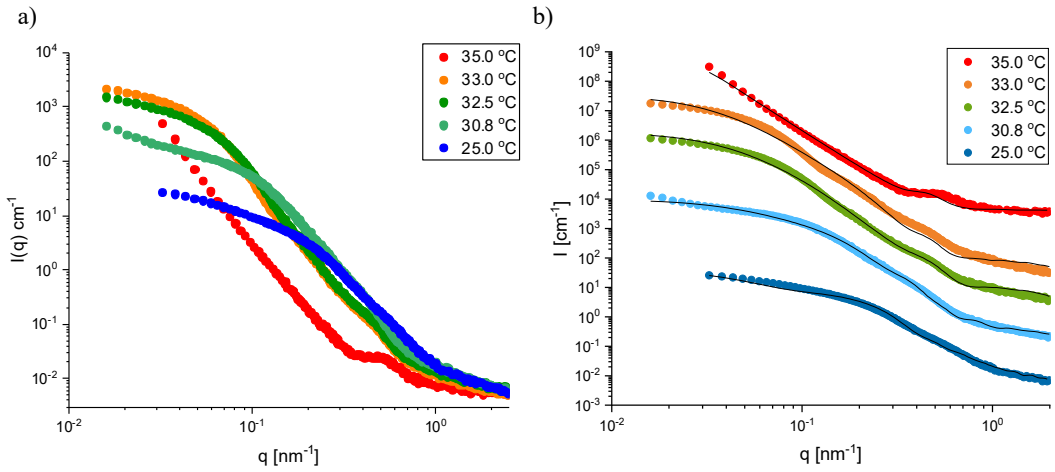

Figure 38. a) SANS curves of PS-b-PNIPAM-BA solution in D_2O with concentration of 5 mg/mL in the temperature range of 25.0 °C – 35.0 °C and b) with their best fits (black lines), curves are shifted vertically to separate the curves.

Figure 38 shows representative SANS curves of PS-*b*-PNIPAM-BA solution prepared in deuterated water with concentration of 5 mg/mL. Upon heating from 25.0 °C to 33.0 °C, the forward scattering intensity increases, what indicates that the polymer solution becomes cloudy. At T = 25.0 °C, where micelles are swollen, at the scattering curve two shoulders can be indicated, one for q ~ 0.19 nm^{-1}, and second, less prominent for q ~ 0.6 nm^{-1}, what is with good agreement with SAXS measurement at the same temperature, demonstrating core-shell micelles. At temperature close to LCST, more prominent shoulder shifts to higher q ~ 0.35 nm^{-1}, due to collapsing of the PNIPAM–shell, and additional shoulder appears at low q value (q ~ 0.1 nm^{-1}) and shifts to lower q (~ 0.055 nm^{-1}) at T = 33.0 °C. This move to lower q value is caused by clusters formation and growth with increase of temperature. At T = 35.0 °C, this shoulder turns into a straight line with slope characteristic for aggregates with smooth surface.[151] Due to continuous growth of clusters at heating, the shoulder may shift to the lower q, beyond the resolution of experimental settings. Also, at 32.5 °C, shoulder at q ~ 0.45 nm becomes more pronounce and can be attributed to the collapsed micelle. From T = 32.5 °C to T = 35.0 °C, this

shoulder moves to ~ 0.55 nm^{-1} by continuous shrinkage of the micelles (dehydration of the PNIPAM block).

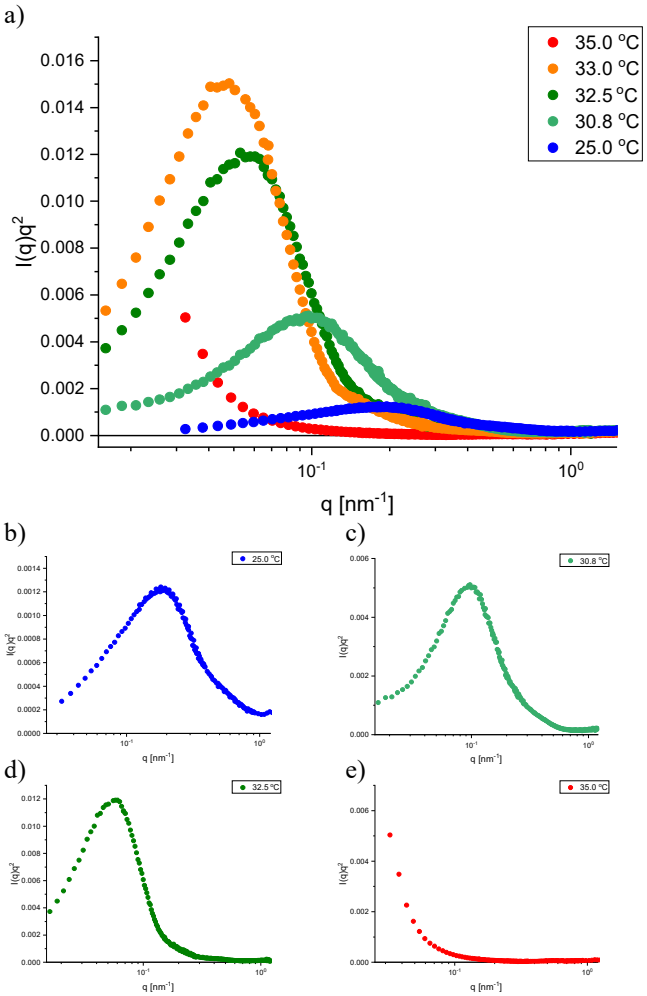

Figure 39. Kratky plot, $I(q)q^2$ vs q of the SANS data for aqueous PS-b-PNIPAM-BA solution at temperature range 25.0 °C – 35.0 °C all compiled (a) and at b) T = 25.0 °C, c) T = 30.8 °C, d) T = 32.5 °C and e) T = 35.0 °C.

Figure 39 shows Kratky plots of the SANS data for PS-*b*-PNIPAM-BA solution, providing the model–free information on micellar structure changes as a function of temperature. Details about Kratky analysis are described in section 2.3.1.6. Figure 39a presents curves together where the cluster growth is traced. Figure 39b shows the SANS curve of the polymer at swollen state with a bell–shaped peak (q ~ 0.19 nm^{-1}) and weak shoulder (q ~ 0.6 nm^{-1}). This can be referred to a spherical core–shell micelle, the bell-shaped peak revealing the spherical structure and additional shoulder, a heterogeneous structure. At the temperature slightly below LCST (T = 30.8 °C, Figure 39c), peak at q ~ 0.19 nm^{-1} shifts to ~ 0.35 nm^{-1} and shoulder at q ~ 0.6 nm^{-1} disappears due to shrinkage of PNIPAM block and due to a decrease of SLD contrast between core and shell in micelles. Additional peak appears at q ~ 0.1 nm^{-1} which can be address to early stage of cluster

formation. Above LCST, the bell–shaped peak is observed with maximum at $q \sim 0.055$ nm^{-1} and ~ 0.045 nm^{-1} for $T = 32.5$ °C and $T = 33.0$ °C, respectively. The maximum shifts to the lower q values, and intensity increases, $I(q)$ [cm^{-1}], what attributes to clusters growing even for a small temperature increase (+ 0.5 °C). Moreover, a weak shoulder at $q \sim 0.2$ nm^{-1} is observed, thus the clusters are formed by micelles with not entirely dehydrated PNIPAM block. At 35.0 °C, is seen only a steep decay at low q, indicates large aggregates with fully collapsed micelles.

The SANS data were analyzed with different models to get detail information about the changes of micellar internal morphology and further aggregation as a function of temperature. PS-core size is not affected by temperature change thus, R_{core} was fixed with value of 5.3 nm (value was determined by SAXS measurement, 3.4.1. From 25.0 °C to 33.0 °C curves were fitted by function *Eq.41.*, where the form factor for core-shell spherical particles $P_{CS}(q)$ (*Eq.29.*) was used to observe the evolution of the PNIPAM-shell and structure factor of fractal aggregates $S_F(q)$ (*Eq.40.*) to monitor the cluster formation with heating. I_0 is a scaling factor, I_{OZ} is an Ornstein-Zernike function (*Eq.31.*) for the concentration fluctuation from the internal polymer network as it was observed in PNIPAM microgel.[152] The influence of fluctuations can contribute the scattering intensity at higher q-values. I_{bkg} is the background intensity.

$$I(q) = I_0 P_{CS}(q) S_F(q) + I_{OZ} + I_{bkg} \qquad (Eq.41.)$$

The SANS curve from $T = 35.0$ °C was fitted with function *Eq.42.*, due to the low SLD-contrast between core and shell, size of the collapsed micelle was determined by sphere form factor $P_s(q)$ (*Eq.28.*), and distance between them in aggregate was obtained by hard sphere structure factor, $S_{HS}(q)$ (*Eq.35.*). Furthermore, at the low q-range, the curve was fitted by Porod law equation (*Eq.27.*) to distinguish a structure of fractals by Porod exponent, d.[153]

$$I(q) = I_{PL} + I_0 P_S(q) S_{HS}(q) + I_{OZ} + I_{bkg} \qquad (Eq.42.)$$

Fit results are presented in Figure 40, where changes of the radii are shown as a function of temperature. At 25.0 °C, PNIPAM–shell thickness is equal to $R_{shell} = 25.4$ nm, thus the size of swollen micelle is $R_{swollen\ micelle} \cong 30.7$ nm, which is in a good agreement with DLS results. Upon heating, the micellar corona shrinks to $R_{shell} = 9.3$ nm at $T = 33.0$ °C. After phase transition, the difference between SLD of PNIPAM-shell and PS-core is small enough that the collapsed micelle can be treated as a homogenous sphere. At the low q-range in SANS is observed that the cluster formation starts below LCST, and

upon heating their size increases from $R_{cluster}$ = 22.0 nm at T = 30.8 °C to $R_{cluster}$ = 26.0 nm at T = 33.0 °C by aggregation. Above LCST, the distance between correlated micelles in the cluster is described by R_{HS}, at T = 32.5 °C the half-distance between particles is R_{HS} = 8.5 nm, and at T = 35.0 °C the R_{HS} decreases to 6.1 nm with Porod exponent d = 3.98. Value of R_{HS} is lower than R_{shell} at temperature slightly above LCST, that means the PNIPAM-shell overlap in aggregates very fast.

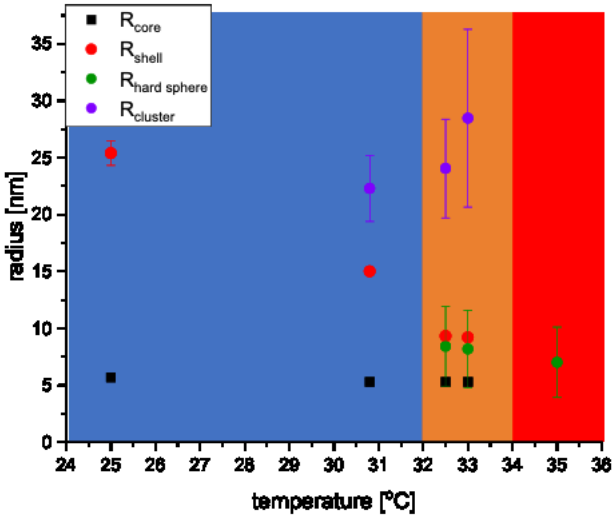

Figure 40. Results obtained from fit models of the SANS data as a function of temperature. The temperature range was divided to 3 parts, below LCST (blue background), slightly above LCST (orange background) and above LCST (red background). The PS-core radius was fixed at fitting and R_{core}=5.3 nm.

Figure 41 shows the contrast profile of scattering length density between micellar corona and solvent along the radial direction. The profile presents that the closer to the core the denser the PNIPAM-shell is. Also, at higher temperature, SLD contrast decreases due to lowering of difference between core and corona SLD.

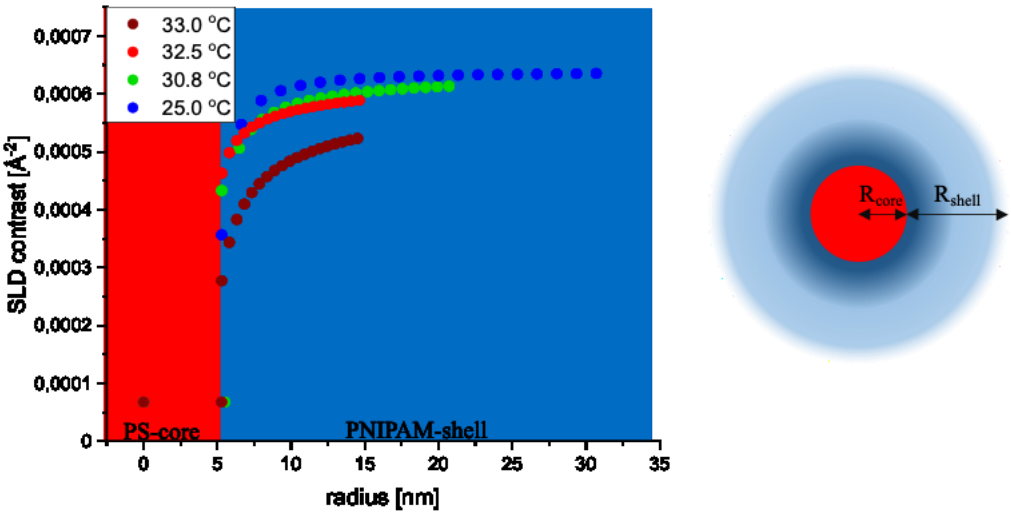

Figure 41. Scattering length density difference of PNIPAM-shell and solvent on distance from PS-core to the edge of PNIPAM corona at 25.0 °C (blue), 30.8 °C (green) and 32.5 °C (red).

SANS measurement for PS-*b*-PNIPAM-BA solution at temperature range 25.0 °C – 35.0 °C gave a detailed information about the PNIPAM-shell thermo-responsiveness. Upon heating, the monitoring of the PNIPAM-shell shrinkage, the distance between correlated micelles in aggregates, cluster formation and growth is possible. Results of radii for micelles and clusters are in good agreement with DLS and cryo-TEM imaging. Additionally, the profile of scattering length density contrast between deuterated water and polymer shows increasing of PNIPAM density with heating. However, at $T = 33.0$ °C, the micellar corona consists of a lot of water.

3.4.3. Cluster swelling/deswelling upon pressure change

The swelling degree of PNIPAM in water can be changed by pressure and can be used to control the cluster formation and its size.[93] The phase transition temperature of PS-*b*-PNIPAM-BA aqueous solution is T_{LCST} = 32.0 °C (in deuterated water) at the atmospheric pressure. The pressure-temperature phase diagram of PS-*b*-PNIPAM-BA solution with c = 5 mg/mL has elliptically shaped coexistence line, determined by turbidimetry (transmission measurement, Figure 42). This shape is characteristic for reversible pressure-temperature protein denaturation and represents the phase boundary between thermodynamically different phases, native and denatured.[154,155] Similar behavior was observed for PNIPAM solutions with different molecular weight.[156,157] Points at the phase diagram were fitted by equation for ellipse according to the Hawley's theory (*Eq.43.*)[154], where p_c and T_c are the values of pressure and temperature indicating the center of the

ellipse, V_c is a volume, $\Delta\beta$ describe the differences in the isothermal compressibility, ΔC_p is the heat capacity between one- and two-state and ΔG_c is a free energy at p_c and T_c. Fit results are presented in Table 2 and thermodynamic parameters are in good agreement with values found in literature.[158]

$$\frac{V_c\Delta\beta}{2\Delta G_c}(p-p_c)^2+\frac{V_c\Delta C_p}{2T_c\Delta G_c}(T-T_c)^2=1 \qquad \textit{(Eq.43.)}$$

Table 2. Fit results from Hawley's equation (Eq.43.)

p_c [bar]	T_c [K]	$\frac{V_c\Delta\beta}{\Delta G_c}$ [bar^{-2}]	$\frac{V_c\Delta C_p}{\Delta G_c}$ [K^{-1}]
394.3	263.0	$5.56 \cdot 10^{-7}$	0.28

Pressure increase at temperature above LCST causes swelling of the PNIPAM chains,[159] and the maximum of the coexisting line is observed at T_M = 33.05 °C and $p_M \cong$ 390 bar. For temperature between T_{LCST} and T_M, the phase transition is observed twice, at low- and high-pressure regime for the same temperature. At the low q-range the coexisting line slope is positive, and first transition is from collapsed to swollen state and represents the first-order transition. With further increasing of pressure (above p_M), second transition from swollen to collapsed state is observed, which is less rapid and clear as first, and it represents a continuous volume transition.[160]

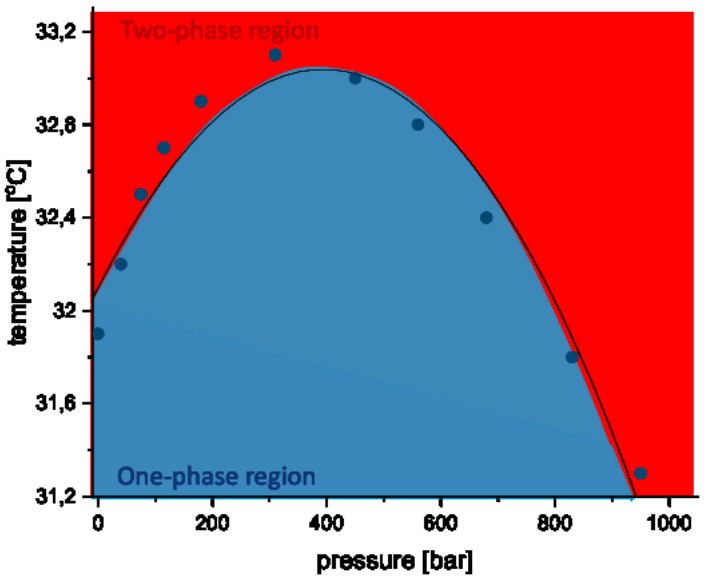

Figure 42. Temperature-pressure phase diagram of PS-b-PNIPAM-BA aqueous solution (c = 5 mg/mL) measured by turbidimetry.

Results and discussion

The SANS measurements were performed to check the effect of the pressure change on the PNIPAM–shell swelling degree. The pressure scan was done at 4 different temperatures above LCST, T_1 = 32.5 °C and T_2 = 33.0 °C, T_3 = 33.2 °C and T_4 = 33.5 °C. Data were fitted with two models, at the two-phase region with *Eq.43.*, and at one-phase region with *Eq.45.* After phase transition, the micelles are not swollen entirely, thus the clusters are still observed and fractal structure factor is used in both models. The fractal dimension (d_f) can be distinguished by the curve slope at the low q-range. At the collapsed state, in high q-range, the peak corresponding to the distance between correlated particles is well visible, thus the $S_{HS}(q)$ was used to determine the R_{HS}. At swelling state, the distance between particles in aggregate increases, and the shoulder at $q \sim 0.045$ nm^{-1} presumably shifts to lower q values due to increase of the micellar corona size and raise or breakdown the correlation between micelles thus this shoulder is not visible.

$$I(q) = I_0 P_{CS}(q) S_F(q) + S_{HS}(q) + I_{OZ} + I_{bkg} \qquad (Eq.44.)$$

$$I(q) = I_0 P_{CS}(q) S_F(q) + I_{OZ} + I_{bkg} \qquad (Eq.45.)$$

PS-*b*-PNIPAM-BA SANS data measured at T = 32.5 °C and in p-range from atmospheric pressure to 1000 bar is shown in Figure 43. Within the pressure increase, the phase transition is observed between p = 100 bar and p = 200 bar by prominent shifting of the shoulder from $q \sim 0.45$ nm^{-1} to the lower q-values and disappearance of peak at q ~ 0.085 nm^{-1}. Shift of the shoulder at the middle-q range indicates the swelling of the PNIPAM-shell in the micelles, thus the size of the shell thickness increases. Above 200 bar, vanish of the peak and changing of the curve slope at the low-q value indicates change of the cluster shape. Moreover, the forward scattering intensity decreases with increasing of pressure, that means the polymer solution becomes transparent, so the micellar PNIPAM corona swells.

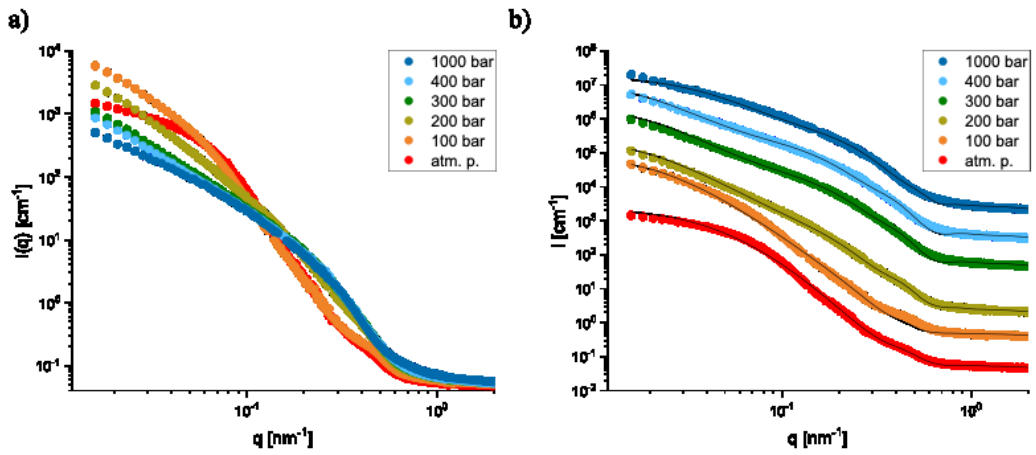

Figure 43. a) SANS curves of PS-b-PNIPAM-BA in D_2O at pressure range 100 – 1000 bar compared with curve measured at atmospheric pressure for temperature of T_1 = 32.5 °C. b) curves are shifted vertically with their best fit as a black line.

Fit results are presented in Figure 44a, and they prove that the transition from two- to one-phase at T_1 = 32.5 °C occurs above 100 bar. At two-phase state, the shell thickness is constant, $R_{shell} \cong$ 9.3 nm, and at the one-phase state the thickness increases to R_{shell} = 13.3 nm at p = 300 bar. More pronounce transition is seen in Figure 44b for parameters of fractal dimension (d_f) and decay SLD-contrast profile (α). At the collapsed state, value of the d_f is above 2.8 and α increases from α = 0.56 to α = 0.72. Fractal dimension parameter decreases to approx. d_f = 2.6 and decay parameter remain constant, $\alpha \cong$ 1.1 at the swollen state. In both states, the fractal dimension parameter indicates that the polymer is densely packed, however, pressure increase to 400 bar cause that packing density is lower by swelling. The shell thickness within one- or two-phase state remains constant, $R_{shell} \cong$ 9.5 nm and 14.5 nm, respectively. In the case of p = 1000 bar the transition from one-phase to two-phase is observed due to deswelling of the PNIPAM thickness of the shell decreases to R_{shell} = 10.0 nm. However, the PNIPAM chains stay more hydrated than at two-phase state for low p-range, and that is proven by the fractal dimension, d_f = 2.45, and decay contrast SLD profile, α = 1.05, parameters. In polymer solution, the cluster size increases significantly with pressure, $R_{cluster}$ = 24.5 nm at atm. p. and $R_{cluster}$ = 60.2 nm at p = 400 bar, although for p = 1000 bar radius decreases to $R_{cluster}$ = 34.0 nm. The half-distance between two correlated micelles in cluster was determined from SANS curves at the two-state phase in low pressure range, at the atmospheric pressure and p = 100 bar. $R_{HS} \cong$ 14.8 nm, which is equal of the size of collapsed micelles (R_{core} + R_{shell}).

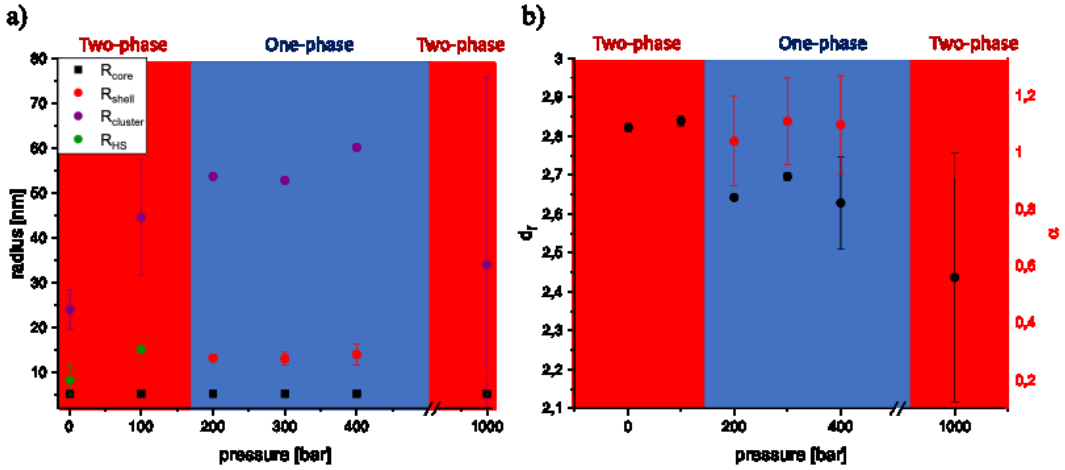

Figure 44. a) Fit results obtained from SANS data for PS-b-PNIPAM-BA solution as a function of pressure at T_1 = 32.5 °C. The black dots represent the radius of the micellar core, red dots – micellar shell thickness, purple dots – radius of the cluster and green dots the half-distance between correlated collapsed micelles in the cluster. b) Changes of a fractal dimension, d_f, and decay parameter of shell-SLD profile, α, as a function of pressure at T_1 =32.5 °C.

Pressure scan from atm. p. to p = 400 bar, with 100 bar step and 50 bar step close to phase transition point, was performed at T_2 = 33.0 °C. SANS data are presented in Figure 45a and with their best fit in Figure 45b. The phase transition from two- to one-phase state is observed between p = 200 bar and p = 250 bar. As it was described for pressure scan at T_1 = 32.5 °C, the pressure transition has been designated in the same way.

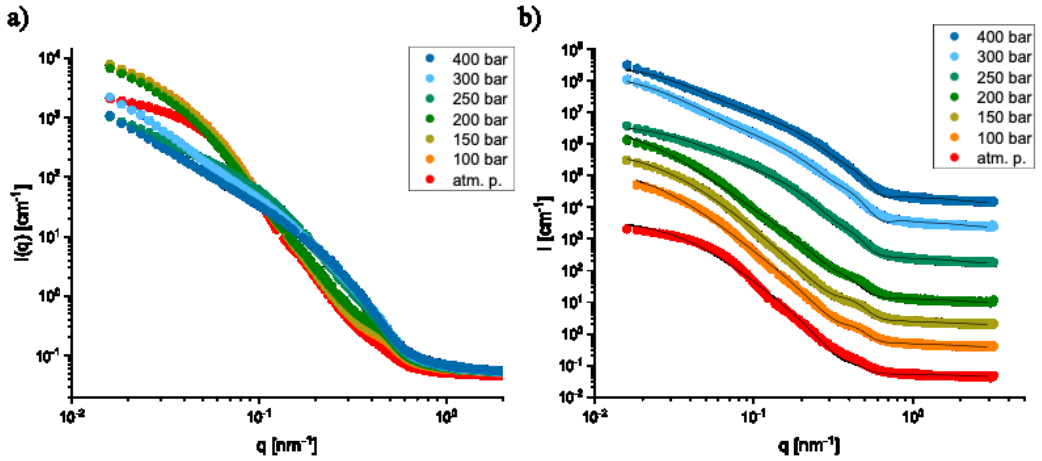

Figure 45. a) SANS curves of PS-b-PNIPAM-BA in D_2O at pressure range 100 – 400 bar compared with curve measured at atmospheric pressure for temperature of T = 33.0 °C. b) curves are shifted vertically with their best fit as a black line.

The micellar corona swells less at T_2 = 33.0 °C than at T_1 = 32.5 °C, ΔR_{shell} (33.0 °C) ≅ 2.5 nm and ΔR_{shell} (32.5 °C) ≅ 4 nm. The same is seen for cluster size, where $R_{cluster}$ does not increases as much as for lower temperature. The fluctuations in the cluster size at one-phase state probably are caused by irregular cluster shape. At atmospheric pressure, the half-distance in clusters is lower than the shell thickness, R_{HS} = 8.2 nm, and R_{shell} = 9.2 nm, due to an overlap of the PNIPAM blocks between micelles. The overlap seems to disappear with pressure increase as R_{HS} becomes larger than shell thickness and the radius of hard sphere growth prominently, compare to change of R_{shell}, at p = 200 bar R_{HS} = 15.1 nm. According to another fit parameters as d_f or α, similarly to previous temperature, the phase transition is sharp and sudden, compared to changes in size of micelles or aggregates.

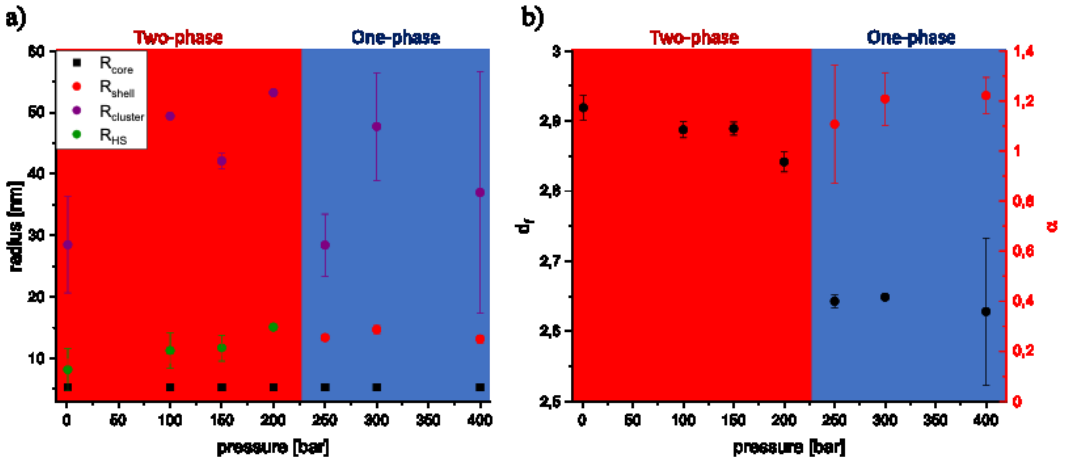

Figure 46.a) Fit results obtained from SANS data for PS-b-PNIPAM-BA solution as a function of pressure at T_2 = 33.0 °C. The black dots represent the radius of the micellar core, red dots – micellar shell thickness, purple dots – radius of the cluster and green dots the half-distance between correlated collapsed micelles in the cluster. b) Changes of a fractal dimension, d_f, and decay parameter of shell-SLD profile, α, as a function of pressure at T_2 = 33.0 °C.

For other temperatures, pressure scan was made only at four steps for every temperature due to the close to maximum point of the coexistence line in phase diagram. The SANS curves and fit results are presented in Figure 47. As it is seen in Figure 47a and Figure 47d, the phase transition at T_3 = 33.2 °C is observed between p = 200 bar and p = 300 bar. However, at T_4 = 33.5 °C, determination of the transition pressure is not very clear, though from SANS curves it was determined for p approx. 300 bar. At T_3, size of the micellar corona increases by approx. ΔR_{shell} (33.2 °C) ≅ 3 nm through transition from two- to one-phase and the changes of the value of other fit parameters are very similar to lower temperatures. At T_4, the transition is not as clear as for other T, increase of R_{shell}

is small ΔR_{shell} (33.5 °C) ≅ 1.6 nm, the cluster size remains fluctuate in approx. 33 nm for the whole *p*-range. Fractal dimension decreases with pressure, from 2.90 (p = 200 bar) to 2.62 (p = 500 bar), and peak, which corresponds to the hard sphere structure factor, shits to the lower q-value, thus minor swelling can be detected.

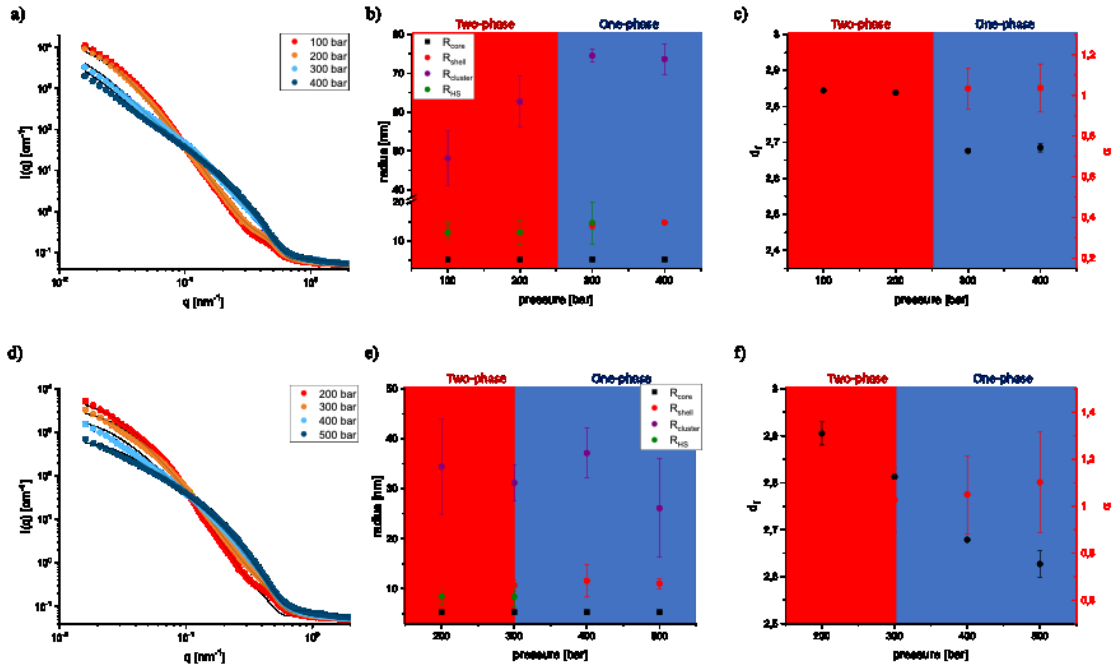

Figure 47. SANS curves with their fits for pressure scan at a) T = 33.2 °C and d) T = 33.5 °C. Fit results are presented in case of radii changes: thickness of the micellar corona (R_{shell}, red dots), size of the clusters ($R_{cluster}$, purple dots), distance between correlated micelles in aggregate (R_{HS}, green dots), black squares represent size of the micellar core, R_{core}, at b) T_3 and e) T_4. Parameters of swell degree are shown in c) and f) for both temperatures as well.

The temperature-pressure phase diagram of PS-*b*-PNIPAM-BA solution with concentration of 5 mg/mL was determined by transmission measurement, where elliptically shaped coexistence line in observed. Influence of pressure change at two-phase state of polymer solution was monitored by SANS experiment at 4 temperatures above LCST. From the phase diagram, at T_1 and T_2 the phase transition should be clear and after crossing the coexisting line, solution changed its turbidity. T_3 and T_4 were chosen due to the temperature at and slightly above the maximum of the line to check if any significant differences in structure can be observed. Through the pressure scan at given temperature, the phase transition from two- to one-phase state was observed for p ≅ 175 bar at T_1 = 32.5 °C, p ≅ 225 bar at T_2 = 33.0 °C and p ≅ 250 bar at T_3 = 33.2 °C. At T_4 = 33.5 °C, the pressure of phase transition is p ≅ 300 bar however, it is not as clear as for lower temperatures. The forward scattering intensity decreases above these pressures what

indicates change in turbidity, thickness of micellar shell grows and shoulder on the SANS curve corresponding to distance between particles in aggregate vanished by shifting to lower *q*-values. Phase transition caused by pressure change is not as sharp as caused by temperature and growth of R_{shell} is only with a few nanometers. Above LCST, small temperature increase in solution causes a significant change in behavior of micelles and clusters size change with pressure increasing.

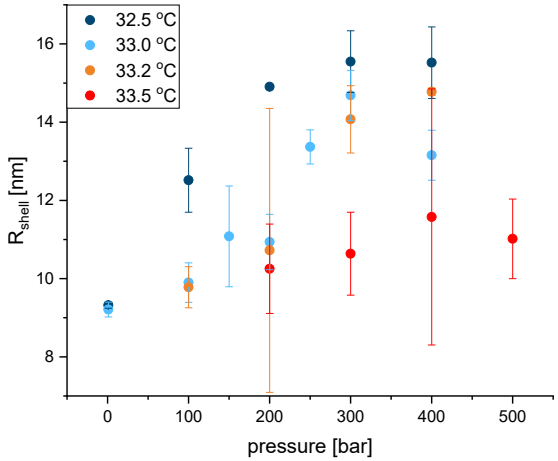

Figure 48. Change of the PNIPAM- shell thickness in pressure at temperature of T_1 = 32.5 °C (dark blue dots), T_2 = 33.0 °C (light blue dots), T_3 = 33.2 °C (orange dots) and T_4 = 33.5 °C (red dots).

Figure 48 shows the influence of the pressure and temperature on the PNIPAM micellar corona. Slightly above LCST (at T_1, T_2 and T_3, below the maximum of coexisting line in phase diagram) the thickness of the PNIPAM micellar corona increases gradually with pressure and swelling is well visible. For temperature above the maximum of the line, the transition still can be distinguished, however the swelling is very limited. At pressure where polymer solution is in one-phase state (p = 400 bar), size of the PNIPAM-shell increases to R_{shell} = 15.5 nm at T_1, although at T_4 PNIPAM-shell swell to R_{shell} = 11.5 nm. The micellar corona size at fully swollen state is approx. 25.0 nm. To compare the size at one-phase state cause by pressure change, the difference is significant what indicates that they are in partially collapsed state. Moreover, at the low *q*-range in SANS curves, the plateau was not observed, thus the clusters were detected in every pressure scan.

3.5. Kinetics of the PNIPAM-shell shrinkage and cluster aggregation at the temperature jump

The phase transition of the PS-*b*-PNIPAM-BA micelles across the LCST caused by temperature jump (T-jump) was followed in real-time from milli seconds to minutes. Time-resolved SANS (tr-SANS) measurement with stopped-flow device was used to provide fast temperature jump. With mT-jump system, fast heating was caused by mixing the polymer solution ($T_{polymer\ solution}$ = 25.0 °C) and pure water heated to T_{water} = 45.0 °C in ratio 1:1, directly before measurement, that shorted the dead time to a few milliseconds (approx. 10 ms). The measuring time for the first frame was 0.1 s and every next frame was measure for a longer time with factor of 1.05. The kinetic experiment was performed for polymer solution at two concentrations, to check the influence of the small change of polymer content for kinetics of the cluster aggregation. To monitor the transition from swollen to collapsed state and next follow the cluster growth within 15 min, the temperature jump from T_I = 25.0 °C to T_F = 35.0 °C was performed in both cases. Due to mixing the solution with hot water, it is possible to monitor the cluster formation and aggregation directly after reaching the desired temperature by polymer solution with high time resolution.

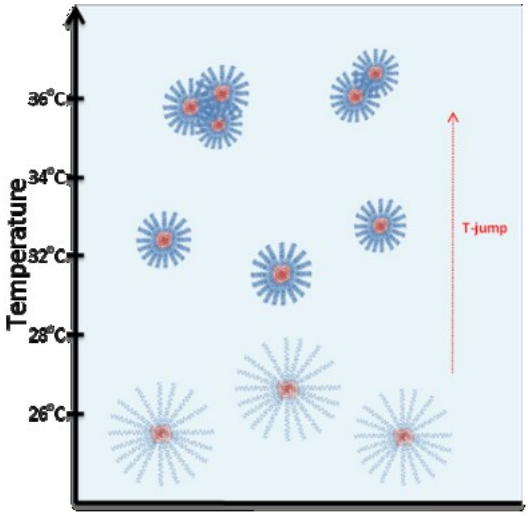

Figure 49. Scheme of the PS-b-PNIPAM-BA micelles behavior as a function of temperature.

3.5.1. Effect of the concentration on the cluster formation

The structural changes were followed at two concentrations: c_1 = 1 mg/mL and c_2 = 5 mg/mL. To compare quantitatively the influence of the concentration and temperature on morphology of the PS-*b*-PNIPAM-BA in water, static measurements

at swollen and collapsed states (T_I = 25.0 °C and T_F = 35.0 °C) were performed. The SANS curves are presented in Figure 50. The blue curves represent the measurement below LCST, at T_I, and red curves above LCST, at T_F. As it is seen, for both concentrations there are no differences in morphology of aqueous PS-*b*-PNIPAM-BA at given temperatures in equilibrium. Below LCST in solution are single swollen micelles and above LCST are large domains of collapsed micelles. The sizes obtained from modeling of SANS curves at static measurements are detailed described in section 3.4.2. The slight increase of forward scattering is observed for solution with concentration of 5 mg/mL however, this is caused by higher polymer content in solution. With this information, the concentration effect on the mechanism of cluster aggregation can be described in detail by kinetics measurement.

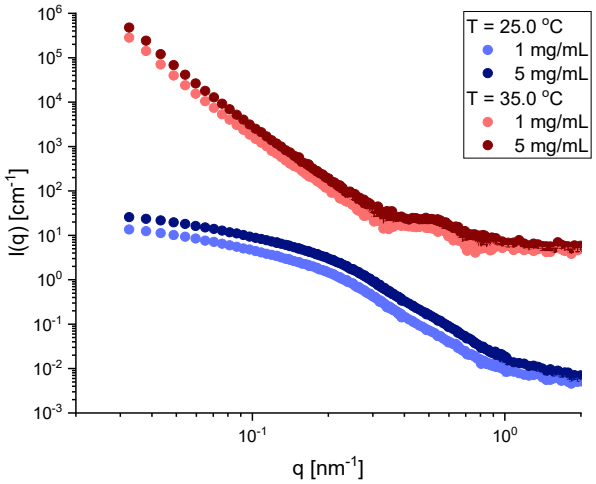

Figure 50. SANS curves of PS-b-PNIPAM solution in D_2O with concentration 1 mg/mL (lighter dots) and 5 mg/mL (darker dots) measured at temperatures T_I = 25.0 °C (blue) and T_F = 35.0 °C (red). Curves represent measurement at high temperature are vertically shifted by a factor of 1000.

Figure 51 shows the results of T-jump kinetics experiment with final polymer concentration of c_1 = 1 mg/mL. 3D-graph in Figure 51a displays changes in the SANS curves as a function of time. Comparison static and kinetics experiments, reveals that, 100 ms after temperature jump, the micelles are already collapsed, and small clusters are formed. The forward scattering intensity increased significantly during first 4 s. Subsequently, the intensity increases slowly till end of measurement. At the first frame, shoulder appears at q ~ 0.11 nm^{-1} and with time, it shifts to lower q values indicates clusters growth. Comparison last frame from kinetics experiment with SANS curve at T = 35.0 °C (Figure 51b) marks that the equilibrium is not achieved and dehydration of the PNIPAM-shell, as well as the cluster aggregation is slow.

SANS curves for first 5 s were according to *Eq.41.*, due to fast cluster formation and their size can be distinguished from the beginning of the measurement.

For frames above 4 s, the $S_{HS}(q)$ was added to the model due to estimate the distance between correlated micelles in clusters and for fitting was used an *Eq.44*. Fit results are presented in Figure 52, where the parameters from fit models describe the shape of particles change, as R_{shell} and $R_{cluster}$, the distance between correlated micelles in aggregate, as R_{HS}, and the swell degree, as α and d_f parameters. The *T*-jumps were repeated a few times and averaged for better statistic. However, due to low concentration of polymer solution and short measuring time, SANS frames for first 10 s are noisy, and the fit results for this time range, have broad errors.

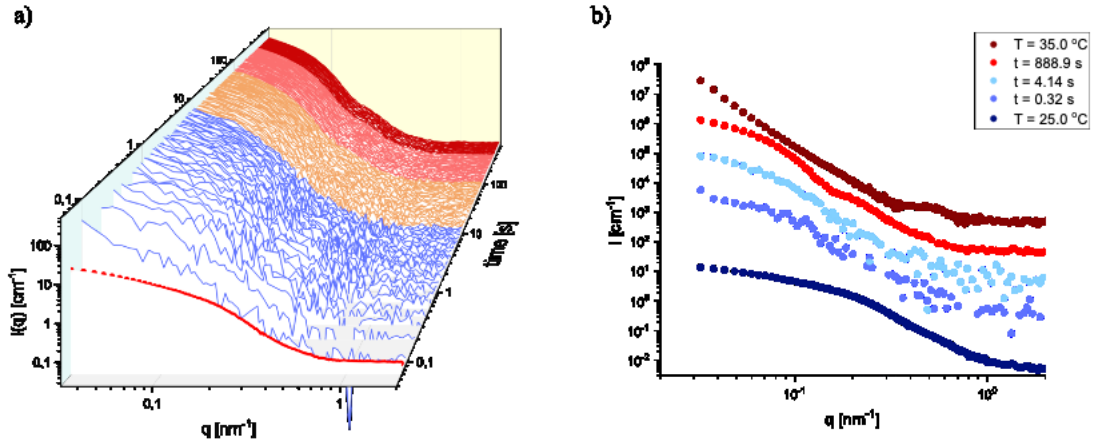

Figure 51. a) 3D-graph of SANS curves after T-jump for PS-b-PNIPAM-BA solution with final concentration of 1 mg/mL and SANS curve measured at initial temperature of the polymer solution (red dots); b) representative curves from kinetics measurement, directly after injection solution to the cuvette (t = 0.32 s, blue dots), after cluster formation (t = 4.14 s, light blue dots) and at the end of measurement (t = 888.9 s, red dots), compared with static results at T_I = 25.0 °C (blue triangles) and T_F = 35.0 °C (red triangles), curves are vertically shifted to each other.

To compare fit results for first frame of kinetic experiment and SANS curve for T_I it is seen that, after *T*-jump, micelles are already partially collapsed, $\Delta R_{shell} \cong 10$ nm, and mass fractal dimension indicate a compact structure, $d_f = 2.71$. For the first 10 s after jump, the thickness of the shell significantly decreases from $R_{shell} = 15.3$ nm to $R_{shell} = 11.5$ nm and d_f gradually increases to 2.85, indicating further dehydration of the PNIPAM-shell. The α parameter gradually decreases due to increasing of the SLD contrast between particles and solvent. R_{HS} distance decreases significantly 20 s after T-jump, from $R_{HS} \cong 15$ nm to $R_{HS} \cong 10$ nm and minor decrease is observed in time. Therefore, the micelles are compacted densely in aggregate which contributes to overlapping of the micellar shell between particles. The cluster size uniformly increases from $R_{cluster} = 22.6$ nm to $R_{cluster} = 30.0$ nm indicates slow aggregation at the measuring time.

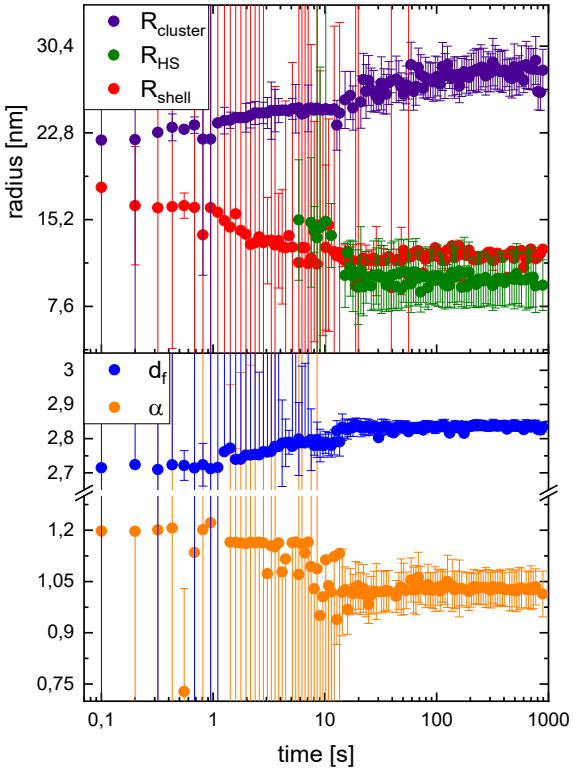

Figure 52. Fit results obtained from SANS data for PS-b-PNIPAM-BA solution as a function of time. The model parameters are presented to describe the evolution of particles size by PNIPAM shell thickness (R_{shell}, red dots), the cluster size ($R_{cluster}$, purple dots), distance between 5micelles in large domains (R_{HS}, green dots), and PNIPAM swell degree by SLD-contrast profile (α, orange dots) and mass fractal dimension (d_f, blue dots) parameters.

Time-resolved SANS measurement was performed for PS-*b*-PNIPAM-BA solution at higher concentration (c_2 = 5 mg/mL) as well. 3D-graph of the SANS curves are shown in Figure 53a for and the results are compared with static curves measured at initial and final temperatures (Figure 53b). Similarly to the solution with lower concentration, directly after injection of polymer solution to the observation cell, the micelles are partially collapsed and during first few seconds the cluster growth is observed. The shoulder at the low *q*-range shifts to lower *q* very fast by cluster aggregation and approx. after 7 s disappears. In a quite early stage, the dehydrated micelles in large domains are distinguished. Last curve for kinetics measurement covers very well with SANS curve from static measurement, which indicates faster aggregation than for solution with c = 2 mg/mL.

SANS frames were divided to two times regimes, at I-time regime for 0.1 s > t > 8 s, the micelles are not fully dehydrated, thus the micellar corona can be still recognized and determined as well as the R_{HS} distance in cluster. Therefore, this region was fitted by *Eq.44*. However, first ten frames are noisy at the high *q*-range, thus the R_{HS}

was difficult to fit and was flawed by a large error and was omitted. The II-time regime for $t > 8$ s the forward scattering follow the Porod law and PNIPAM-shell is dehydrated that core-shell micelle can be treat as a homogenous sphere, thus the frames were fitted with *Eq.42.*

The fit results are shown in Figure 54. Immediately after *T*-jump, the $R_{shell} = 12.8$ nm and with time it gradually decreases to $R_{shell} = 8.8$ for $t = 8.01$ s. The cluster size slowly grows from $R_{cluster} = 23.8$ nm to $R_{cluster} = 29.6$ nm for the first 2 s, further the growth accelerates and at $t = 8.01$ s $R_{cluster} = 48.5$ nm. Due to the decrease of the SLD contrast between core and shell in micelle, in the II-time regime, the size of the homogenous sphere was determined as a radius of collapsed micelle, R_S, which gradually decreases at the whole measuring time. Consequently, the distance between micelles in aggregate shrinks slowly with time, value of the radius decreases from $R_{HS} = 13.3$ nm at $t = 1$ s to $R_{HS} = 7.7$ nm at $t = 888.9$ s. It is more pronounced than at lower concentration. To compare with the static experiment, at $T_F = 35.0$ °C, $R_{HS} = 6.1$ nm what means that 15 min after temperature jump, this state was almost reached for polymer solution with c_2. The distance between collapsed particles is lower than R_S approx. 25 s after T-jump, thus the micellar corona overlaps between micelles in cluster.

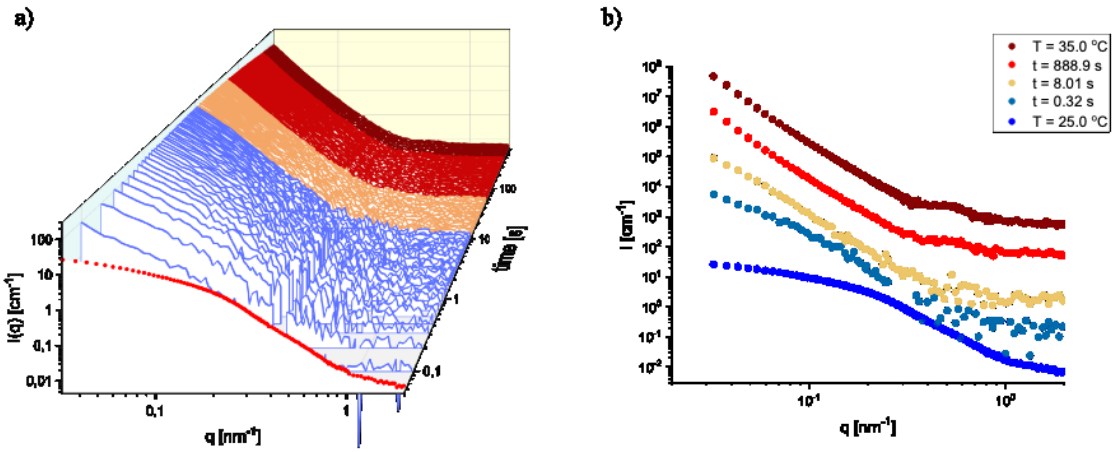

Figure 53. a) 3D-graph of SANS curves for PS-b-PNIPAM-BA solution with final concentration of 5 mg/mL representative curves from kinetics measurement, directly after injection solution to the cuvette (t = 0.32 s, blue dots), after cluster formation (t = 8.01 s, yellow dots) and at the end of measurement (t = 888.9 s, red dots), compared with static results at $T_I = 25.0$ °C (dark blue triangles) and $T_F = 35.0$ °C (dark red triangles), curves are vertically shifted to each other.

In the I-time regime, clusters are formed immediately, and they are mass fractals due to water trapped in PNIPAM-shell. Mass fractal dimension, indicate that they are compacted in the early stage after T-jump, $d_f = 2.79$. Value of fractal dimension increases in time and after 8 s clusters are very compacted, thus the roughness of the fractal surface

can be described. The surface of aggregates become quite smooth (d = 3.55) approx. 75 s after fast heating and further d slightly increases to 3.66.

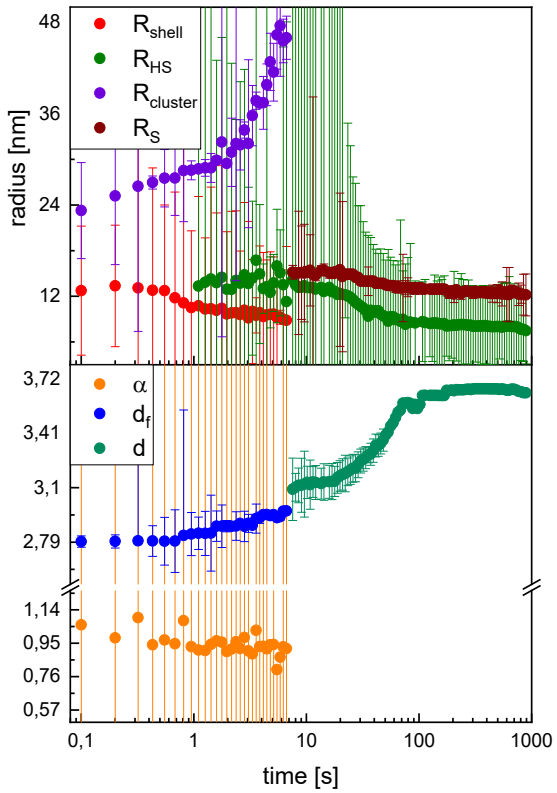

Figure 54. Fit results obtained from SANS data for PS-b-PNIPAM-BA solution as a function of time. The model parameters present the collapsing of the PNIPAM-shell (R_{shell}, red dots), cluster growth ($R_{cluster}$, purple dots) the evolution of distance between micelles in large domains (R_{HS}, green dots), size of the collapsed micelles (R_S, dark red dots), mass fractal dimension (d_f, blue dots), surface fractal dimension (d, light green dots) and decay parameter of SLD contrast between shell and solvent (α, orange dots).

The temperature jump from 25.0 °C to 35.0 °C in polymer solution with two different concentrations was performed with stopped-flow device, and the structural changes were followed by tr-SANS. The mT-jump system used with stopped-flow, can cause a temperature jump in millisecond time range which allows tracing cluster formation in real-time. Immediately after injection of solution to observation cell, the micelles were partially collapsed and formed small clusters. With time, the slow dehydration of PNIPAM-shell and cluster growth was observed. However, discrepancies are observed in the mechanism of cluster aggregation depends on the concentration, even for a small change.

The fractal dimension indicates that, directly after T-jump the PNIPAM-shell is densely packed, independent on the concentration (d_f ~ 2.75). With time it gradually increases however, for c_1 after 15 min d_f is still lower than 3, what means that the clusters

have very rough surface and $R_{shell} \cong 10$ nm thus shell not fully dehydrated. For c_2 and the same T-jump, large domains appear fast and fractal dimension indicates that roughness of their surface significantly decreases, and after 15 min $d = 3.65$. However, from the static SANS curve, at temperature of 35.0 °C, fractal dimension can reach $d = 3.98$, thus the surface is smooth.

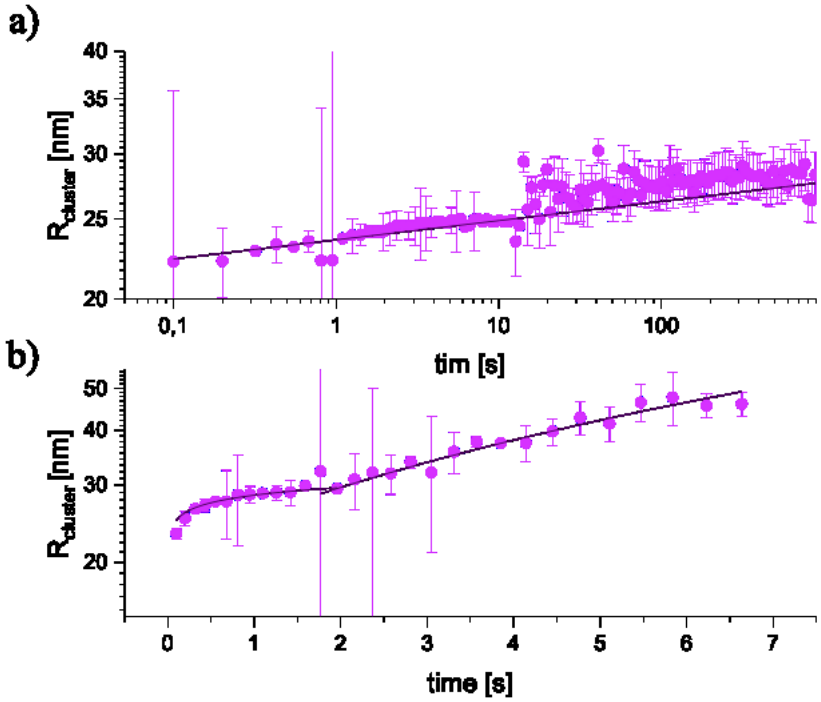

Figure 55. The aggregation kinetics of clusters in PS-b-PNIPAM-BA solution with concentration a) c_1 = 1 mg/mL and b) c_2 = 5 mg/mL. In the case of the lower concentration, only DLCA kinetics was observed, however, for higher concentration.

Kinetics of clusters aggregation was followed for both polymer concentrations and significant differences are observed depending on the small change of polymer content in solution. The aggregation can be described as a diffusion-limited colloid aggregation (DLCA) or reaction-limited colloid aggregation (RLCA). The kinetics of DLCA is related to the power-law and increase of $R_{cluster}$ is proportional to t^{ϵ}, where the exponent ϵ is inversely proportional to fractal dimension, and cluster size as a function of time has linear behavior on logarithmic graph. In the case of RCLA, the kinetics is exponential, thus the linear behavior is observed for semi-logarithmic plot.[161] At the low concentration, the cluster size linearly increases with time, what indicate the DLCA kinetics (Figure 55a). In Figure 55b in presented the $R_{cluster}$ evolution for polymer solution with c_2 in time on semi-logarithmic plot due to clear behavior change 2 s after T-jump (Figure 54, upper graph). From $t = 2$ s to $t = 7$ s, the size growth is linear, thus the kinetics can be described as a RLCA. Initially, the behavior is exponential thus, it can be overlap of DLCA and RLCA kinetics.

3.6. Mechanism of the phase transition across LCST for PNIPAM-based linear polymers trace by optical transmission change

3.6.1. Fast temperature jump induced by NIR-laser setup

Near infrared (NIR) laser setup consist of Raman laser and thulium-fiber laser allows to a very fast temperature jump in polymer solution, with tracing the kinetics from nanoseconds to hours. The Raman laser causes the temperature jump in aqueous solution within $t_{laser\ pulse}$ = 10 ns and the temperature increases up to ~ +10 °C. After 1 s, solution cools down to initial temperature ($T_{initial}$) by thermal diffusion. Thulium laser heats the sample within $t_{laser\ pulse}$ = 100 μs, and the jump can reach ~ +20 °C with keeping higher temperature (T_{max}) to 9 s. When the laser is off, heat from *T*-jump dissipates to $T_{initial}$ after approx. 2 min. Moreover, both lasers can be used simultaneously, thus the changes of optical densities (*OD*) can be followed in polymer solutions. Change of temperature induced by laser pulse can be traced using the aqueous solution of phenol red that acts as a fast responsive thermo-sensitive dye. Its transient absorption at a wavelength of λ = 560 nm can be related to temperature. Absorption of phenol red increases with characteristic time of 100 ns corresponds to rate-limiting step of the deprotonation of the dye induced by temperature change. Profiles of temperature change in time caused by Raman laser pulse (red line), thulium laser pulses (blue line) and Raman-thulium laser pulses (magenta line) for phenol red solution are presented in Figure 56.

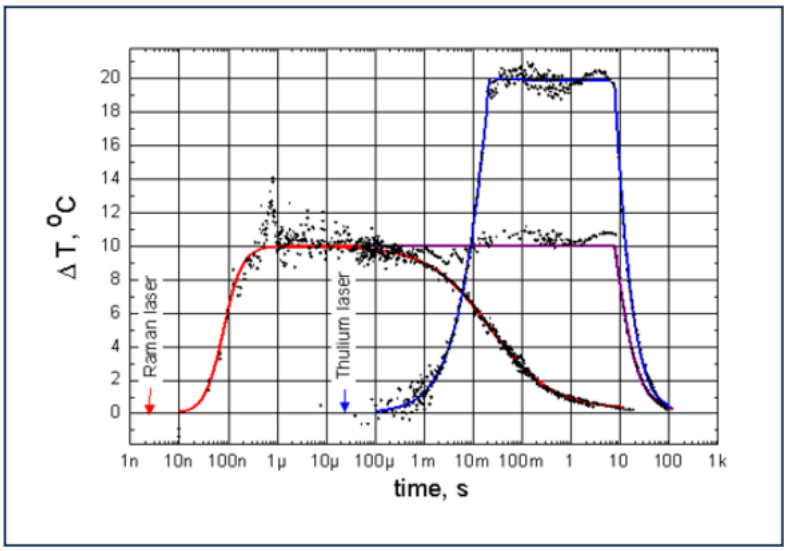

Figure 56. Profile of temperature jump induced by Raman laser (red line), by thulium laser (blue line) and by Raman-Thulium lasers simultaneously (magenta line). The profile was done for transient adsorption of Phenol Red at λ = 560 nm, where points are measurement and lines are fit.[162]

Trace of ΔOD (optical density difference) as a function of time was done by normalization of OD from experiment by OD of sample measured at $T_{initial}$. The optical density is the logarithmic ratio of incident light intensity to transmitted light intensity, then the very small changes can be detected. ΔOD was calibrated before every jump. When hydrophobicity of PNIPAM change, hydrogen bonds between the amide group and water break down, and the formation of the H-bonds between amid groups in the polymer chain is preferred, thus solution changes from transparent to turbid. Therefore, the intensity of the transmitted light decreases drastically.

Three polymers, PS-b-PNIPAM-BA, PS-b-PNIPAM-C_{12}, and PNIPAM-36 have been used for measurements, to compare two different systems, polymer coils and micelles, the difference in end-groups within one system, and influence of the of hydrophobic block in polymer chain on kinetics of phase transition for PNIPAM-based linear polymers. Concentration of the solution was c = 10 mg/mL to be above overlap concentration (e.g., $c^*_{\text{PNIPAM-36}} \cong 2$ mg/mL). Due to small change in optical density at the cluster formation state than in the aggregation state, experiments with different laser setups were done for each sample. At first, T-jump was induced only by Raman laser (RL experiment) to check polymer responsiveness on quick and short impulse. The second experiment was done with both lasers, where Raman laser induced T-jump in nanoseconds and temperature after jump was kept at T_{max} for 9 s by thulium laser (RTL experiment).

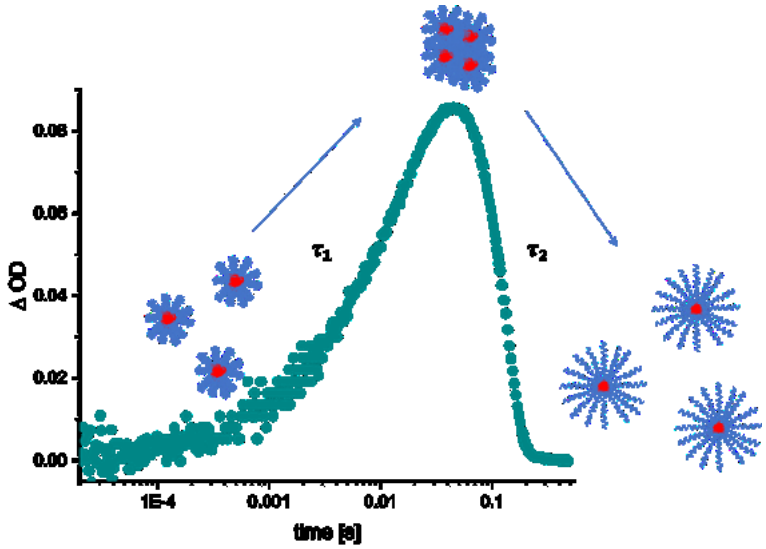

Figure 57. The scheme of micelles behavior after T-jump above phase transition temperature induced by Raman laser pulse.

Figure 57 and Figure 58 show proposed mechanism of micelles behavior as a function of time in experiments with Raman laser and Raman-thulium laser, respectively. In RL experiment, can be distinguished two-steps kinetic mechanism for the forward and reverse transition (Figure 57) across LCST, where the solution is heated up fast with a very

short laser pulse ($t_{laser\ pulse}$ = 10 ns). The time of micelles collapse can be designated at the point where ΔOD starts to increase. With further increasing to maximum, characteristic time of cluster formation and early stage of cluster aggregation (τ_1) can be detected. Temperature in solution starts to decrease approx. 1 ms after laser pulse. Therefore, when the temperature in solution decreases below T_{LCST}, the ΔOD value returns to zero, what indicates a swelling process with characteristic time τ_2. The closer initial temperature of solution is to phase transition temperature, the longer polymer is in two-phase state (Figure 59). Due to the *T*-jump is constant, the shallow or deep jumps can be made by varying a $T_{initial}$.

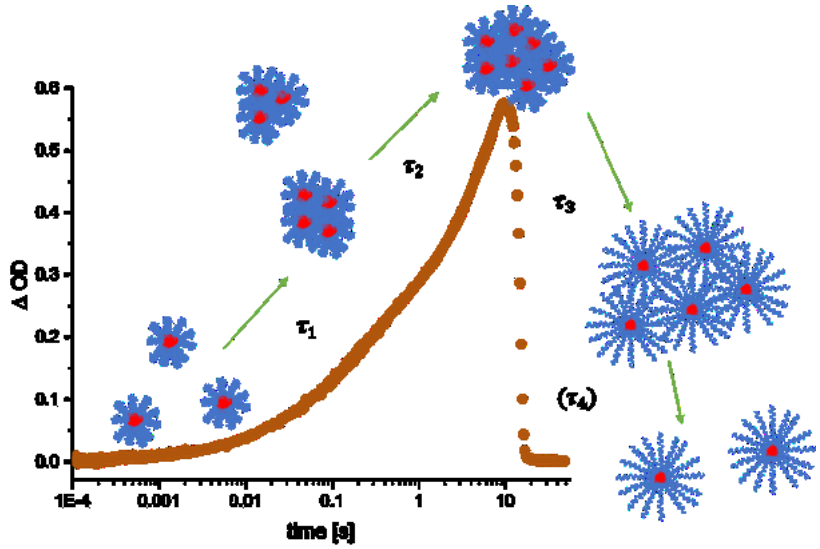

Figure 58. The scheme of micelles behavior after T-jump above phase transition temperature induced by Raman-thulium laser pulses.

In the RTL experiment, where two lasers were used to induce fast *T*-jump and keep temperature at T_{max} for a few seconds (Figure 58), more complex mechanism is observed. Upon heating, two-step mechanism is recognized. The first step can be described as the cluster formation with characteristic time τ_1 (the same as for RL experiment). The second step is much slower, and it indicates cluster aggregation with τ_2. When the thulium laser is off, the ΔOD value decreases by changing the turbidity of the polymer solution and two-steps can be described as well. When the solution cools down below the phase transition temperature, the clusters first swell, causing increase in their size and changing the turbidity to a rather transparent one. With further cooling down, the turbidity of the PNIPAM solution comes back to clearly transparent state and in the solution are only single swollen micelles. Similarly in this case, the kinetics of the swelling can be divided to two characteristic times, τ_3 and τ_4. However, the cluster swelling step is not always possible to

detect by overlapping with kinetics of breakage to individual swollen micelles. When $T_{initial}$ is below the hysteresis range, only one step is observed due to very fast de-aggregating.

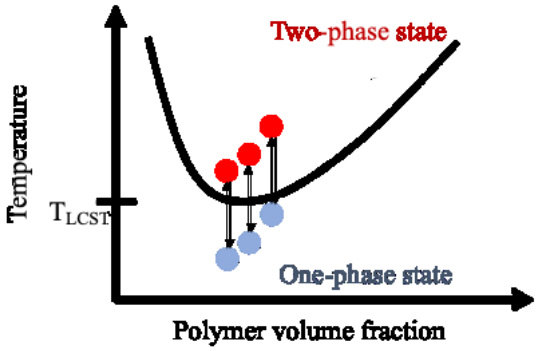

Figure 59. Scheme of T-jump across LCST for different $T_{initial}$. Due to the ΔT is constant for every jump, the shallow or deep temperature jump above transition point can be performed.

Experimental curves show a non-exponential time dependence for forward and reverse transition for every *T*-jump, thus they were fitted by Kohlrausch-Williams-Watts (KWW) function (*Eq.46.*), where τ is a characteristic relaxation time and β is stretched exponent for β<1 or compressed exponent for β>1.[163] β is related to characteristic time's distribution, and it is a shape parameter. For the relaxation dynamics of glass-forming liquids was found crossover from stretched to compressed relaxation if the temperature is decreased slightly below T_g.[164] This unusual super-diffusive behavior is thought to be related to the relaxation of internal stress and a ballistic-like dynamics in this regime.[165,166]

$$I(t) = Ae^{-(t/\tau)^{\beta}} \qquad (Eq.46.)$$

Datasets obtain in RL experiment were fitted with *Eq.47.* With short laser pulse and fast temperature return to $T_{initial}$, the initial rise on time scale was analyzed by stretched exponential function with stretching exponent, β_1, for $t \leq t^*$, and for followed decay was used compressed exponential function with compressing exponent, β_2. Characteristic relaxation times, τ_1 [s] and τ_2 [s], show the time range at which the polymer aggregates and swells, respectively. t^* is a transition time where the *OD* starts to decrease and was determined from modeling.

$$I(t) = \begin{cases} I_1\left(1 - e^{-(t/\tau_1)^{\beta_1}}\right) & for \quad t \leq t^* \\ I_2 \cdot e^{-((t-t^*)/\tau_2)^{\beta_2}} & for \quad t > t^* \end{cases} \qquad (Eq.47.)$$

Results and discussion

For the experiment with both lasers (RTL), was observed additional processes for each stage (with some exceptions), thus the curves were analyzed by *Eq.48.*, where: τ_1 is characteristic time of aggregation process [s], τ_2 is characteristic time of aggregates growth [s], τ_3 and τ_4 are characteristic relaxation times of fast and slow aggregates dissolution [s], β_1 and β_2 are stretched exponents of aggregates formation and growth, β_3 and β_4 are compressed exponents of fast and slow aggregates dissolution.

$$I(t) = \begin{cases} I_1\left(1 - e^{-(t/\tau_1)^{\beta_1}}\right) + I_2\left(1 - e^{-(t/\tau_2)^{\beta_2}}\right) & for \quad t \le t^* \\ I_3 \cdot e^{-\left(\frac{t-t^*}{\tau_3}\right)^{\beta_3}} + I_4 \cdot e^{-\left(\frac{t-t^*}{\tau_4}\right)^{\beta_4}} & for \quad t > t^* \end{cases} \qquad \textit{(Eq.48.)}$$

Analysis of curves was performed with fixed stretched and compressed exponents to get a better overview of τ changes, as a function of temperature ($T_{initial}$). Values of exponents were estimated on the analysis of the same data, where this parameter was free and for every state, β is temperature independent. Value of stretched exponent for cluster formation, $\beta_1 = 0.68 \sim {}^{2}/_{3}$, corresponds to DLCA[167,168], and in aggregation process $\beta = 1.0$ indicates exponential growth typical for RLCA.[169] The swelling process when temperature decreases below LCST, the compressed exponents of $\beta = 2.0 - 2.5$ indicate fast local expansion of PNIPAM chain in a good solvent.

T-jumps were performed in series of $T_{initial}$ which were increased/decreased with step of 1 °C – 2 °C. There were no significant differences in characteristic times (τ) depending on the heating or cooling process, thus values of τ are presented together for both processes.

First measurements have been done only with Raman laser, where *T*-jump was cause by a single laser pulse. The *T*-jump was estimated by aqueous solution of phenol red dye in the case of RL experiment the jump was gained of ΔT = +8 °C. The datasets were fitted by two KWW-functions (*Eq.47.*) with fixed exponents, $\beta_1 = 0.68$ and $\beta_2 = 2.0$. Therefore, from the modeling, two characteristic relaxation times were distinguished: for cluster formation (τ_1) and cluster swelling (τ_2).

Figure 60a shows the representative curves with their best fits (black lines) for PS-*b*-PNIPAM-BA. Experiment was performed for initial temperatures in range of 24.0 °C – 30.0 °C. Increase of $T_{initial}$ causes a significant shift of transition time (t^*) to higher value, from 0.07 s to 0.23 s. The characteristic time increases linearly in a semilogarithmic plot (Figure 60b), from 0.0018 s to 0.045 s for τ_1 and from 0.017 s to 0.6 s for τ_2. Also closer to LCST, the amplitude of ΔOD changes significantly, from 0.014 to 0.22 by the aggregation to larger polymer-rich domains with a deep temperature jump.

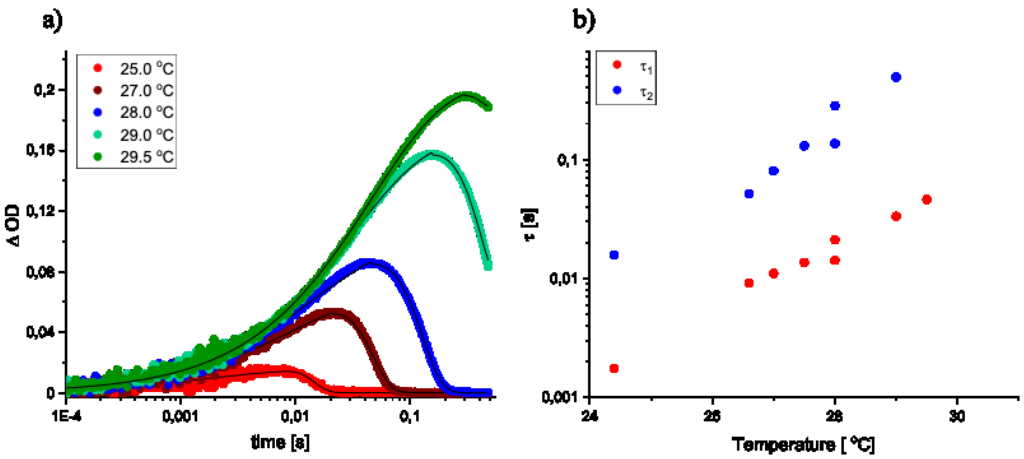

Figure 60. a) Representative curves in time function of the optical density changes for PS-b- PNIPAM-BA after T-jump (ΔT = +8 °C) induced by Raman laser pulse (black line) and b) characteristic relaxation times of cluster forming and swelling in aqueous PS-b-PNIPAM-BA solution for different initial temperatures.

Similar behavior was obtained for PNIPAM-36 solution in RL experiment at initial temperature range of 26.0 °C – 31.7 °C. The representative curves with their best fits are shown in Figure 61a, and fit results in Figure 61b. PNIPAM-36 in water acts as a random polymer coil, and two distinguished processes can be described as follow: 1. collapsed chain aggregation and 2. swelling of the aggregates. For the lowest $T_{initial}$ = 26.0 °C, $\tau_1 = 5.1\,ms$ and $\tau_2 = 15.5\,ms$, for the highest $T_{initial}$ = 31.7 °C, $\tau_1 = 55.7\,ms$. The τ_2 was impossible to determine for the highest initial temperature, due to the polymer remained at the globule state (solution stayed turbid) which is consistent with the DLS results (Figure 22).

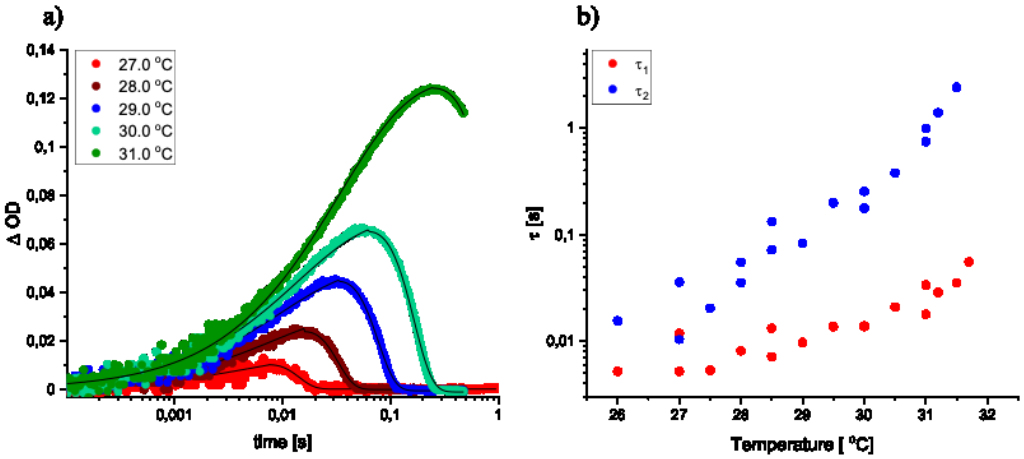

Figure 61. a) Representative curves of time dependence of the optical density changes for linear PNIPAM-36 after T-jump (ΔT= +8 °C) induced by Raman laser pulse (black line)

and b) characteristic times of cluster formation and swelling at different initial temperatures.

Figure 62 presents the representative experimental curves and the fitting results for PS-*b*-PNIPAM-C_{12}. In the experiment with fast *T*-jump induced by Raman laser pulse, a 3-steps mechanism is observed, which can be described as follow: 1. cluster formation, 2. cluster swelling, and 3. slow cluster disintegration. For the analysis, the exponents were used as before, and the additional step was fitted with $\beta_3 = 1.0$. Even for a very short laser pulse, the additional slow process is observed for a reverse transition, which can be explained by morphology of the polymer. The polymer chain has a short PS-block (approx. 18 styrene monomers) and a long hydrophilic PNIPAM block (140 NIPAM monomers) with a dodecyl end-group. In the aqueous solution, the polymer chains self-assemble into flower-shaped micelles or/and create connections (bridges) between micelles at swollen state. This can affect the kinetics of phase transition, mostly for concentration above c^*. The additional slow process can be caused by connections between micelles and recovery to the initial state (below LCST) is slowed down.

PS-*b*-PNIPAM-C_{12} solution at room temperature is not completely transparent (Figure 21, turbidity experiment) and with calibration on pure water, the transmittance is $TR \cong 80\%$, where both PS-*b*-PNIPAM-BA and PNIPAM-36 have $TR \sim 100\%$. Therefore, the amplitude of ΔOD for copolymer with dodecyl group is smaller than for other examined polymer solutions, when temperature increases. Moreover, the transition time does not shift as pronounced as for other polymers within the experimental temperature range.

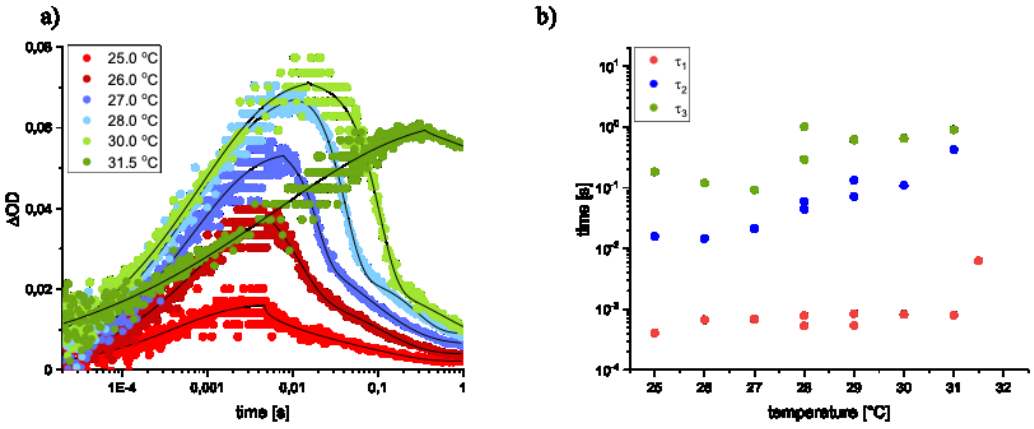

Figure 62. a) Representative curves of time dependence of the optical density changes for linear PNIPAM after T-jump (ΔT= +8 °C) induced by Raman laser pulse (black line) and b) characteristic times of processes of aqueous PS-PNIPAM-C_{12} solution for different initial temperature.

The same samples were tested in RTL experiment to check the influence of the illumination time of laser pulse on mechanism of polymer aggregation. The second NIR-laser setup causes the temperature jump of ΔT = +10 °C. When the thulium laser is off, the

temperature in the solution decreases by dissipation, which gives the characteristic times of reverse processes.

Figure 63 shows the RTL experiment results for PS-*b*-PNIPAM-BA polymer solution. The measurements were performed within temperature range of $T_{initial}$ = 24.0 °C – 30.0 °C. In the case of the PS-*b*-PNIPAM-BA solution, at low $T_{initial}$, a 3-step mechanism is distinguished of forward and reverse PNIPAM phase transition. Above 28.0 °C, the kinetics mechanism is observed with 4-steps. The datasets were fitted by bi-stretched and bi-compressed exponential functions (*Eq.48.*). Each step is described by a characteristic time, τ. For analysis, the stretched and compressed exponents are fixed with values of $\beta_1 = 0.68$, $\beta_2 = 1.0$, $\beta_3 = 2.5$, $\beta_4 = 2.0$. Characteristic time of the first process, cluster formation, remains constant as a function of initial temperature, $\tau_1 \cong 0.13\ s$. The second process, cluster aggregation, is described by τ_2. At the $T_{initial}$ between 24.0 °C – 27.0 °C, value is constant, $\tau_2 = 4.5\ s$. With a further increase of $T_{initial}$ to T = 30.0 °C, value of τ_2 decreases to 3.0 s, which indicates a slight acceleration for deep *T*-jumps. For the reverse transition, value of τ_3 increases exponentially in a semilogarithmic plot with $T_{initial}$ and above 28.0 °C additional fourth process is distinguished, τ_4, which can be described as a slow cluster swelling and disintegration to single micelles. Values of τ_4 are close to values of τ_3 but significant differences are found at compressed exponent values.

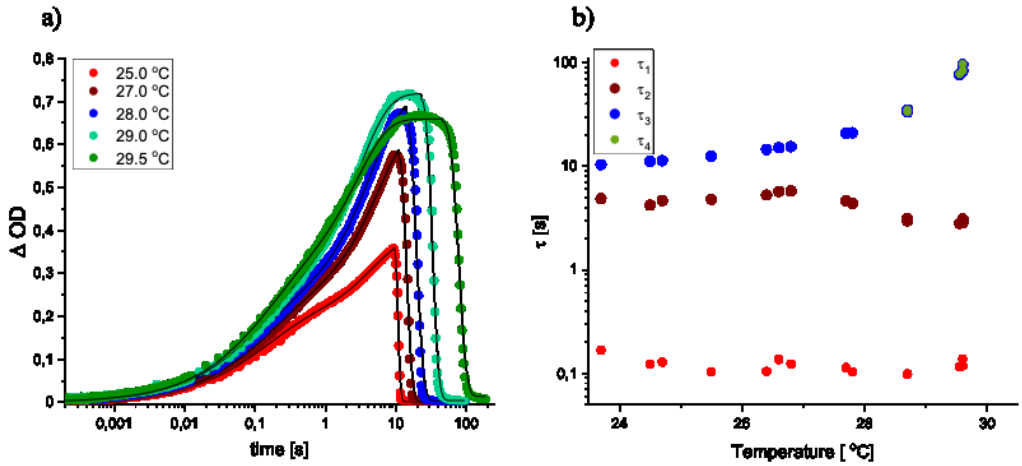

Figure 63. a) Representative curves of the optical density changes after temperature jump (ΔT = +10 °C) induced by Raman and thulium laser pulses with their fits (black line) and b) characteristic times of processes of aqueous PS-b-PNIPAM-BA solution for different initial temperatures when solution was kept in higher temperature ~9s).

At the T-jump induced by RTL pulses for a solution with linear PNIPAM-36, the 4-steps kinetics mechanism is observed for forward and reverse transitions at the measured temperature range of 22.0 °C – 31.5 °C. Figure 64a shows representative curves of ΔOD changes as a function of time with their best fit and the analysis results are

presented in Figure 64b. From $T_{initial}$ = 24.0 °C to 26.0 °C, values of τ are constant. From 26.0 °C to 31.5 °C the characteristic times increase for polymer chain aggregation and aggregates growth (from 0.32 s to 0.11 s and from 7.40 s to 2.70 s, respectively), which is not observed for the copolymer. Fast and slow swelling processes are significantly slowed down, close to the transition temperature (from 9.70 s to 78.4 s and from 13.1 s to 27.5 s, respectively). Above 31.0 °C, last step of swelling fades away.

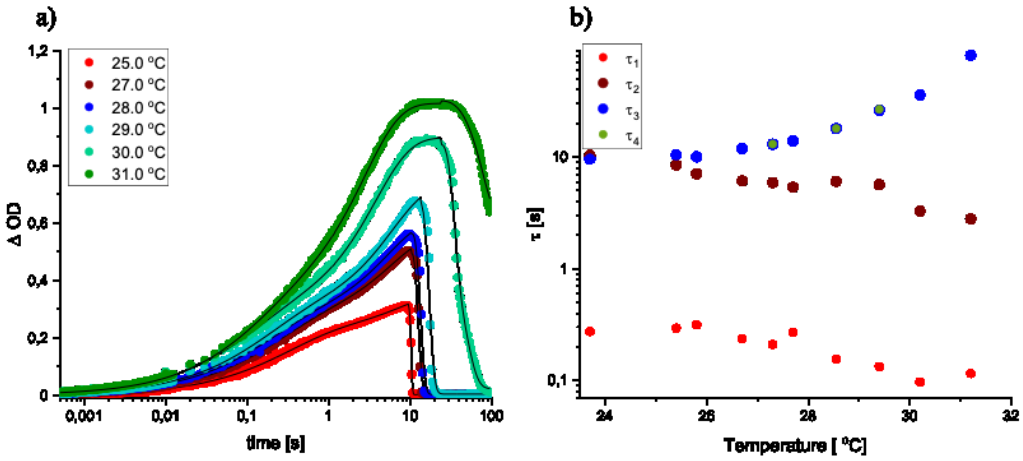

Figure 64. a) Representative curves of the optical density changes after temperature jump (ΔT = +10 °C) induced by Raman and thulium laser pulses (black line) and b) characteristic times of processes of aqueous linear PNIPAM solution for different initial temperatures when solution was kept in T_{max} ~10s.

Comparing the results from the RTL experiment for both copolymers, significant differences are observed in kinetics of transition across LCST. In the case of PS-*b*-PNIPAM-C_{12} for experiment with two lasers setup, the 4-steps mechanism is observed in the initial temperature range (24.0 °C – 32.0 °C), and representative curves with their best fits are presented in Figure 65a. Kinetics mechanism can be described in the same way as for PS-b-PNIPAM-BA: 1. clusters formation, 2. clusters aggregation, 3. rapid swelling of aggregates, and 4. slower disintegration of aggregates. The stretched (β_1 and β_2) and compressed (β_3) exponents are set as for previous samples. However, the exponent for the last step is set $\beta_4 = 1.0$, due to much slower returning to transparent state. Figure 65b shows the results of curves fitting. The characteristic times of cluster formation and clusters aggregation are constant for the whole temperature range and the values are approx. 0.95 s and 2.8 s, respectively. In the case of swelling process, two steps are observed for each $T_{initial}$. The characteristic times, τ_3 and τ_4, increase exponentially with initial temperature, however there is a significant difference between τ_3 and τ_4. For $T_{initial}$ = 24.0 °C, τ_3 = 9.0 s and τ_4 = 14.0 s, and close to LCST, τ_3 = 80.0 s and τ_4 = 94.0 s. Due to a stepwise swelling process, as described in previous sections, the closer the $T_{initial}$ to transition temperature,

the larger domains can stay at the end of reverse transition. Therefore, returning to transparent state is longer or solution can stay turbid even at temperature below LCST.

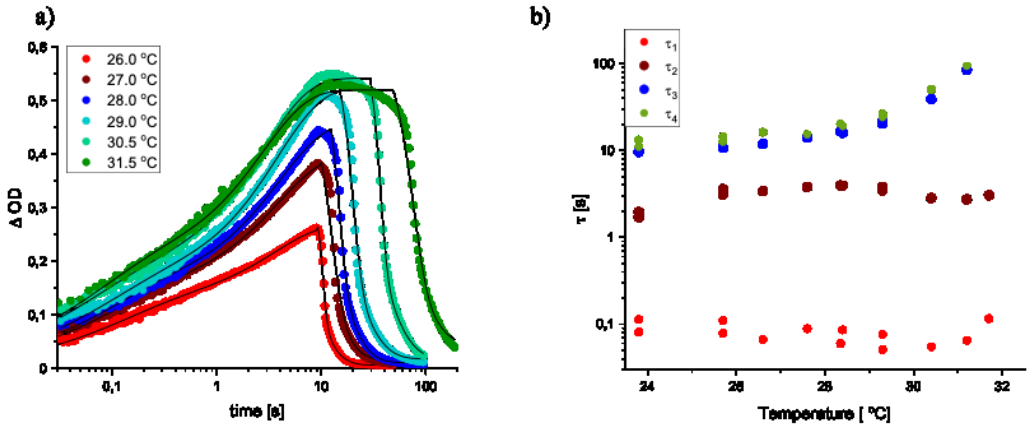

Figure 65. a) Representative curves of the optical density changes after temperature jump (ΔT = +10 °C) induced by Raman and thulium laser pulses with their best fits (black line) and b) characteristic times of processes of aqueous PS-b-PNIPAM-C12 solution for different initial temperatures when solution was kept in higher temperature ~9 s.

Both time-resolved experiments for different PNIPAM-based systems show a real time response on rapid heating. Here, the change of optical density, thus the turbidity in polymer solution was traced in a broad time scale, from sub-milliseconds to minutes.

At RL experiment, the turbidity of sample starts to increase from 0.5 – 0.7 ms. That is with a good agreement with a calculated value of half-time rapid coagulation (*Eq.6.*) for particles of the same size, such as single collapsed coils or micelles, τ_{RC} ~ 0.75 ms. This can be attributed to the begin of nucleation along polymer chain as it was reported previously for individual PNIPAM polymer.[10,11] For copolymer with dodecyl end-group, increase of ΔOD is one order of magnitude faster than for other polymers, which can be caused by connection between micelles. Temperature jump induced only by short laser pulse revealed 2 step mechanism of phase transition in polymer solution. The characteristic time of early state cluster formation (τ_1) above LCST and swelling (τ_2) of PNIPAM-shell below LCST is estimated as a function of initial temperature in solution. Coil or micelle collapse is difficult to distinguish in this experiment by relatively small change in solution turbidity, compared to strong changes of ΔOD for aggregation. The kinetics mechanisms and parameters obtained from analysis for PNIPAM-36 and PS-*b*-PNIPAM-BA are very similar. Within copolymers, the difference in end-groups causes different behavior for the cooling process. In the case of PS-*b*-PNIPAM-C_{12} additional step is observed, independently of the value of initial temperature in solution. The third step can be described as a slow cluster disintegration to small domains with swollen PNIPAM-shell or as a local expansion at swelling. Short laser pulse causes the phase transition by heating solution

above LCST. However, the laser illumination time is too short to create dehydrated aggregates, thus only small clusters are formed, which immediately swell below T_{LCST}.

Across LCST, a more complex kinetics behavior is observed in the RTL experiment. Upon a temperature jump above T_{LCST}, swollen state A forms a collapsed state B, which undergoes an aggregation and microphase separation (C). Upon cooling below T_{LCST}, polymers at aggregated state de-swell, creating a state D, which can further de-aggregate, thus returning to swollen state A. Each step of complex mechanism of phase transition can be characterized by a rate constant, $k_i = {}^{1}/_{\tau_i}$, which is related to characteristic relaxation time.

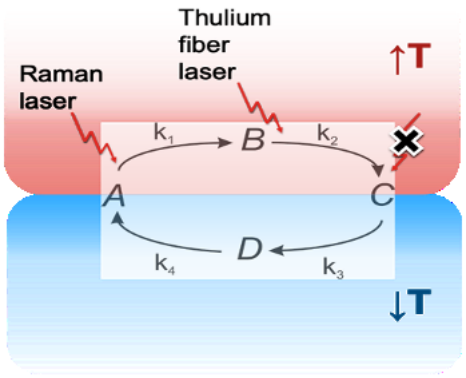

Figure 66. Scheme of multistep kinetics mechanism across transition temperature in Raman-thulium laser experiment.

Measurements were performed for a wide $T_{initial}$ range to cover shallow and deep jumps above phase transition temperature for RL and RTL experiment. The most significant differences in kinetic model are observed for RTL, when $T_{initial}$ is within a hysteresis temperature range. As it is shown by DLS (3.2.2) and cryo-TEM imaging (3.3.3), in order to return for polymer aggregates to swollen state, temperature in solution has to be decreased of a few degrees below LCST to fall apart of large domains to single particles. At the deep T-jump, the cluster aggregation becomes faster for PS-*b*-PNIPAM-BA and PNIPAM-36, but for PS-*b*-PNIPAM-C_{12} this process is constant regardless of the jump depth. Moreover, the swelling processes significantly slowdown from a few seconds to minutes, where for $T_{initial}$ outside of hysteresis range remain constant. In the case of copolymer with dodecyl end-group, the second process (τ_2) is approx. 2 s – 3 s, and this may be cause by the polymer morphology in water solution, as is mentioned before. In the case of size change, PNIPAM can be in swollen state, but the micelles/coils can still be in irregular clusters thus, performing T-jump from that state, the ΔOD will increase much faster.

The shallow or deep jumps above phase transition temperature show a clear distinction in ΔOD amplitude at transition time, t^*. The deeper T-jump above LCST the

more pronounced ΔOD at maximum point and t^* shifts to larger values. Analyzing the delay of return to one-phase state for each polymer depends on the T-jump depth, the interesting insight are observed at RL and RTL experiment. Independently on polymer system, the transition time increases very similarly and in the same value range. In Figure 67 is presented the t^* as a function of temperature jump depth (ΔT_{depth}) above LCST for a) RL and b) RTL setups. When $T_{initial}$ is outside the hysteresis temperature range, the delay increases linearly in semilogarithmic plot. In the hysteresis range, t^* significantly increases deviating from the previous trend. In both cases, for $\Delta T_{depth} > 7$, points diverge from linear function. For RL experiment, the aberrations are smaller than for RTL by shorter heating time of polymer solution. Furthermore, polymer solution always returns to one-phase state in the case of RL experiment, even very close to LCST. When the polymer solution is heated by 9 s, the solution stays in two-phase state much longer even after laser pulse is off. For $T_{initial}$ at the hysteresis range, the delay is well visible even for several seconds or solution stays turbid till end of measurement. The single short laser pulse heats the polymer solution above LCST, and phase transition is observed. Nevertheless, only small clusters are aggregated, which immediately swell at $T_{solution} < T_{LCST}$. Aggregation to a large domains is observed approx. 2 – 3 s after T-jump for solution with concentration above c^*, where RLCA dominates and it is shown at RTL experiment (Figure 63, Figure 64, Figure 65) as well as at tr-SANS (Figure 55b).

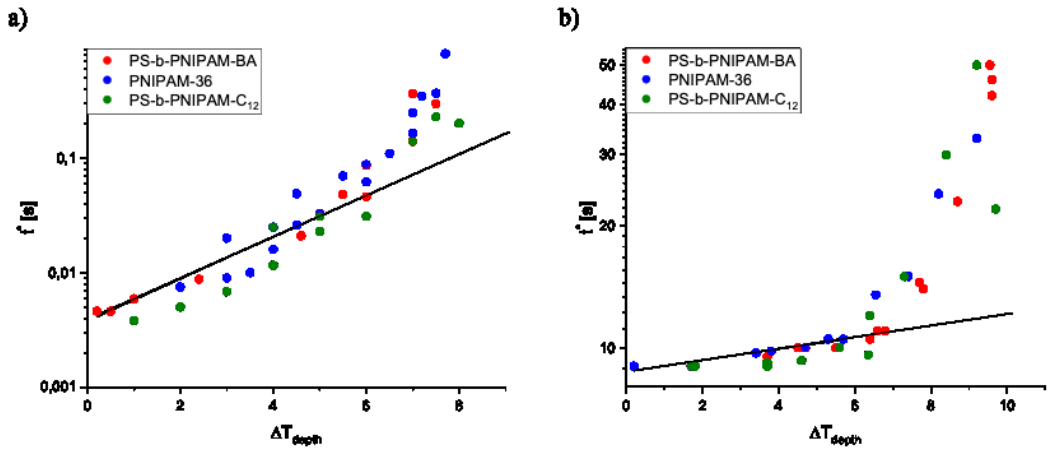

Figure 67. Transition time for polymers examined in a) RL and b) RTL experiments as a function of temperature jump depth above LCST.

Due to a wide range of initial temperature for the RTL measurement, and clear distinction between two steps in aggregation process, an apparent activation energy (E_a) of phase transition can be determined. For that, the rate constant of the cluster formation is calculated, k_1, from τ_1 (obtained from experiment). Arrhenius plots for cluster formation and aggregation is presented in Figure 68 for each polymer. Designated values of E_a are listed in Table 3. Similar of E_a for PNIPAM-based polymers experimentally were achieved

by different groups[76,170,79] and the high values of energy are explained that the phase transition occurs cooperatively along the PNIPAM chain in water. At the phase transition, the hydrogen bonds between water and amide group from polymer chain break down and the minimum energy needed for that is approx. 20 – 30 kJ/mol.[171] Therefore, during phase transition simultaneously multiple hydrogen bonds break down, which may increase the activation energy.

The highest E_a was obtained for linear homopolymer assumably by larger solvation layer around polymer chain in swollen state, comparing to micelle. Hydrophobic-hydrophilic PNIPAM copolymer creates less H-bonds per polymer chain with water than PNIPAM homopolymer, thus the less energy is needed to accomplish the phase transition.

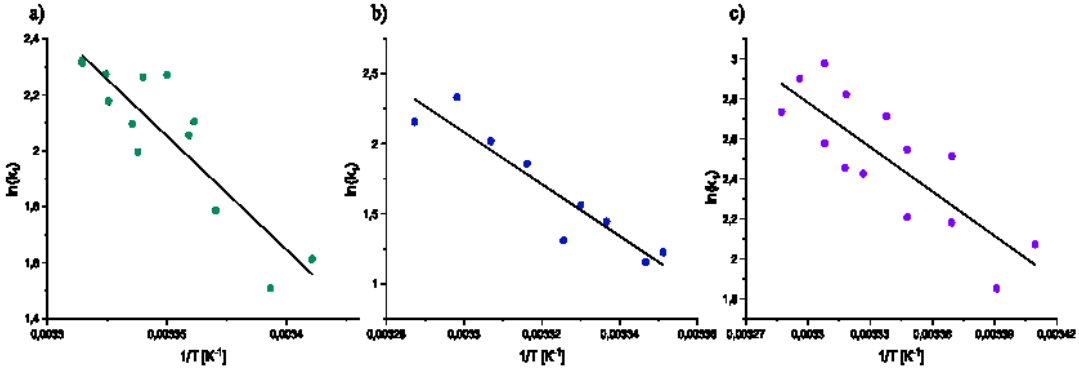

Figure 68. Arrhenius plot of cluster formation for a) PS-b-PNIPAM-BA, b) PNIPAM-36 and c) PS-b-PNIPAM-C_{12} to determine the activation energy of the process.

Table 3. Values of apparent activation energy for clusters formation and aggregation obtained from Arrhenius function.

Polymer / Activation Energy [kJ/mol]	PS-*b*-PNIPAM-BA	PNIPAM-36	PS-*b*-PNIPAM-C_{12}
E_a	72.8	164.5	65.8

3.6.2. Temperature jumps in hysteresis temperature range

The temperature jump induced by laser pulses allows studying a phase transition mechanism of thermo-responsive polymers in detail. Stepwise behavior of collapse and swelling processes is traced by optical transmittance change as a function of time. NIR-lasers setup described in the previous section (3.6.1.) heats sample in nanoseconds, where the energy of laser pulse and illumination time is fixed, and the depth of the jump above LCST is controlled by the change of initial temperature in solution. Due to significant differences in phase transition kinetics in the hysteresis temperature range, the following

experiments were performed with a thulium NIR-laser setup with HSC as a detector. With this setup, it is possible to change laser pulse energy and the exposure time, as well as sample thickness. As a result, the depth of the temperature jump can be adjusted, and polymer solution can be heated up within a range of $\Delta T \cong 0.5$ °C – 10 °C.

At the measurement, change of backscattering intensity is followed by HSC with a frame frequency of 1000/2000 fps. Therefore, the evolution of thermal diffusivity in solution is traced with a step of 1/0.5 ms. Figure 69 shows the example of measurement for PS-*b*-PNIPAM-BA, and the solution was kept at initial temperature of $T^* = 30.0$ °C. With the lase pulse parameters of $E_{laser\ pulse} = 500$ mJ, $t_{laser\ pulse} = 10$ ms and sample thickness of 0.6 mm, the sample is heated by approx. +5 °C. In the initial state, the solution is transparent, so the dark background under the cuvette is well visible. Directly after the laser is off, a light circle is visible with a diameter of 5 mm, which corresponds to size of the laser beam, and boundary between dark and light areas is sharp. Next, the white circle becomes more pronounced due to aggregation to larger domains. The size of circle increases to ~8 mm of diameter at 2 s after *T*-jump, with easy to distinguish one- and two-phase areas. After that time, changes of size or intensity are no longer observed in the two-phase state. The bistability state can be constant for a very long time (e.g. in days), as described in section 3.3.4.

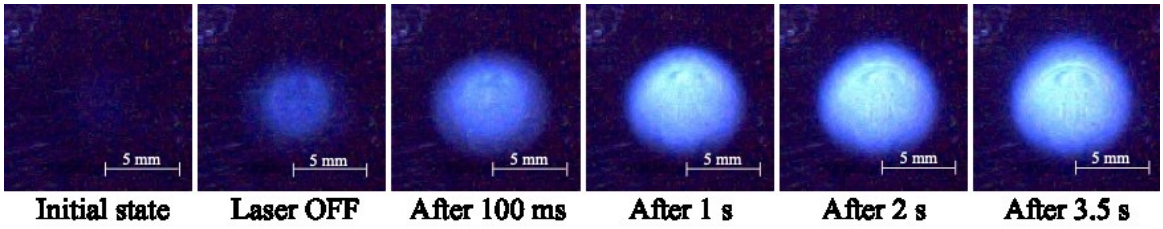

Figure 69. Snapshots of phase-transition evolution in time after laser pulse for PS-b-PNIPAM-BA solution with pulse energy of $E_{laser\ pulse} = 500$ mJ, illumination time of $t_{laser\ pulse} = 10$ ms, sample thickness of 0.6 mm and laser beam diameter of 5 mm.

A laser pulse can write the information in the polymer solution with exposure time within milliseconds. If the temperature of solution is kept in hysteresis window, the information can be stored for a long time. As it is observed from previous experiments, the swelling process is influenced by both the energy of laser pulse and the heating time. Therefore, series of measurements was performed for linear PS-*b*-PNIPAM-BA, where the laser pulse energy, illumination time and sample thickness varied. Figure 70 presents the snapshots of difference in the spot size 100 ms after laser pulse with laser parameters listed in Table 4. The size of the written spot significantly changes with the shortening of a laser pulse. The longer exposure, the further heat diffuses from the hit spot, thus a larger area in solution passed from one- to two-phase state. In the energy range of $E_{laser\ pulse} = 500$ mJ – 25 mJ, the written spot stays on the solution thus the energy is sufficient to aggregate

polymer in large clusters which do not de-aggregate below LCST. For measurement with $E_{laser\ pulse}$ = 10 mJ, the illuminated spot disappears approx. 1.5 s after (Figure 71), so there is not enough energy to aggregate the large clusters. Additionally, in this figure, though the size of laser beam is the same for both measurements, a difference in illuminated spot size is observed. The spot made by pulse with $E_{laser\ pulse}$ = 10 mJ has approx. 2–3 mm of diameter, whereas for pulse with $E_{laser\ pulse}$ = 25 mJ, spot size is approx. 5 mm. The difference in size can be caused by inhomogeneous energy distribution at the cross-section of beam. Therefore, there is less energy on the beam edges. Energy distribution in the laser beam can have a Gaussian profile thus, the polymer solution cannot be heated sufficient at the edges of the illuminated spot to create large aggregates. For thinner sample, the edges are sharp due to a heating of smaller solution volume. Thus, the aggregates are large enough to stay in a two-phase state and complete microphase separation. Reducing a sample thickness changes the sharpness of the two-phase state edges. At the measurements with the thickness of solution 200 μm, the boundary between phases is sharp, and with the thickness of 600 μm the boundary is rather blurred.

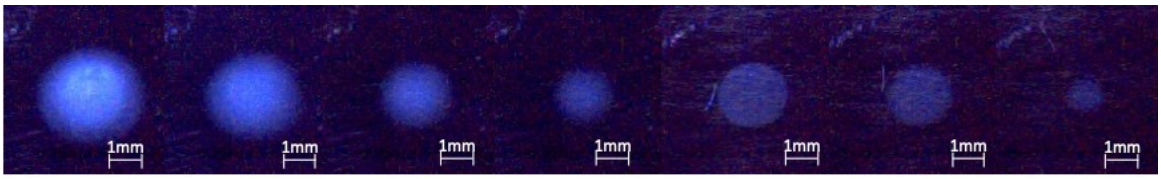

Figure 70. Difference of spot size written on the PS-b-PNIPAM-BA solution by NIR-laser at 100 ms after laser-pulse depending on the time and energy of the laser-pulse.

Table 4. Conditions of laser pulse and sample thickness for Figure 70.

Energy [mJ]	**500**	**250**	**100**	**50**	**50**	**25**	**10**
Pulse time [ms]	10	5	2	1	1	0.5	0.5
Thickness of sample [μm]	600	600	600	600	200	200	200

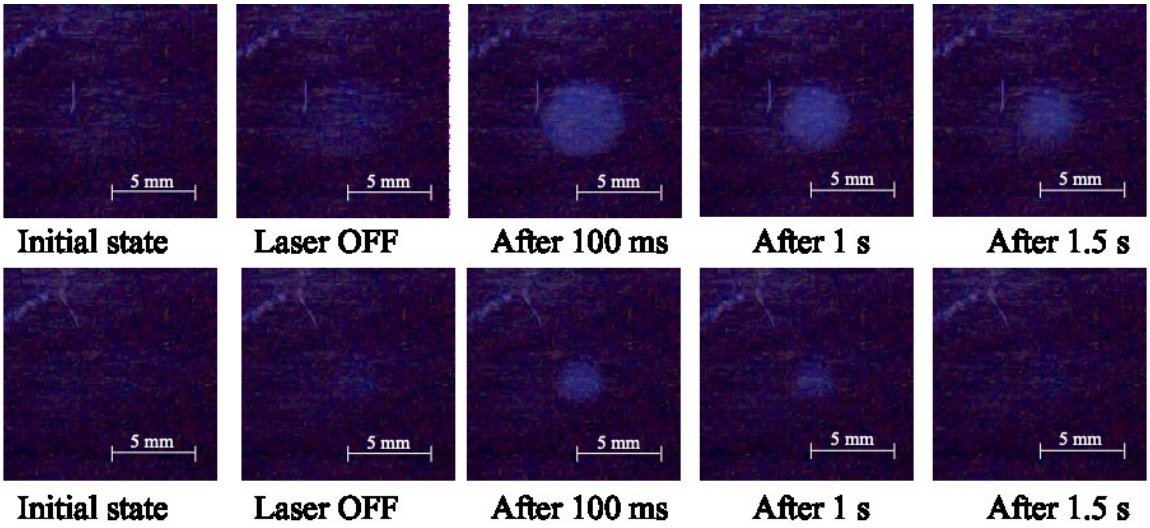

Figure 71. Snapshots of phase-transition evolution in time after laser pulse, with beam diameter of 5 mm, for PS-b-PNIPAM-BA solution with illumination time of $t_{laser\ pulse}$ *= 0.5 ms, sample thickness of 0.2 mm and pulse energy of* $E_{laser\ pulse}$ *= 25 mJ (up) and* $E_{laser\ pulse}$ *= 10 mJ (bottom).*

The focus of the laser beam allows reducing the laser pulse energy to $E_{laser\ pulse}$ = 7.5 mJ, at which polymer does not return to one-phase state after *T*-jump. Illumination time of laser pulse was set to $t_{laser\ pulse}$ = 0.5 ms, which is the shortest time possible with this setup. The beam diameter can be decreased to 1 mm by lens thus, polymer is heated to a higher temperature. Additional measurements were performed with the focused laser beam and compared with the non-focused one. Results are presented in Table 5. For the non-focused beam, the lowest energy of the pulse that heats polymer solution above LCST is $E_{laser\ energy}$ = 10 mJ. For lower energy, the transition to two-phase state is difficult to detect. When a lens is used to focus beam, backscattering intensity significantly increases at the hit spot, and collapse process is possible to trace even for laser pulse energy of $E_{laser\ energy}$ = 7.5 mJ, where polymer stays at aggregated state. For $E_{laser\ energy}$ = 5 mJ the phase transition is observed. However, 1s after laser pulse, solution returns to the one-phase state. With the focused beam, higher energy, and HSC, it is possible to trace the heat transfer from the illuminated spot and the size changes in time function. The smallest step between snapshots from HSC used for this experiment was 0.5 ms thus, it is possible to catch the polymer solution turbidity directly after laser pulse and in detail trace changes over time in detail.

Table 5. Evolution of spot size made by laser pulse on PS-b-PNIPAM-BA solution at time function depends on energy of laser pulse, thickness of the sample and focusing of beam by lens. Polymer solution was kept at the initial temperature of $T^* = 30.0$ °C.

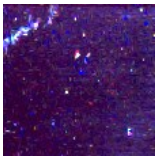	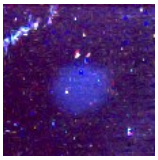	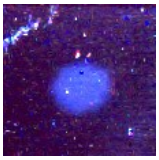	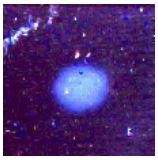	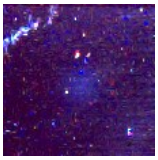	
Initial state	After 5 ms	After 10 ms	After 100 ms	After 1s	
Energy: 25 mJ	Pulse time: 0.5 ms	Power: 100%	Sample thickness: 100 μm		
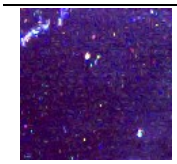	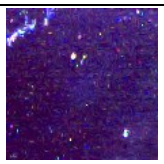	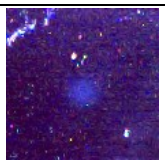	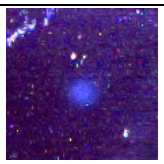	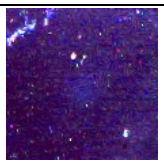	
Initial state	After 5 ms	After 10 ms	After 100 ms	After 1 s	
Energy: 10 mJ	Pulse time: 0.5 ms	Power: 40%	Sample thickness: 100 μm		
	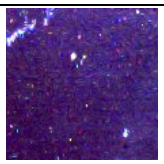	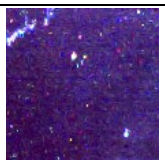	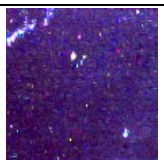		
Initial state	After 5 ms	After 10 ms	After 100 ms		
Energy: 7.5 mJ	Pulse time: 0.5 ms	Power: 30%	Sample thickness: 100 μm		
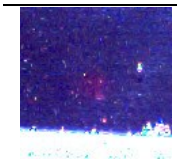	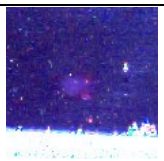	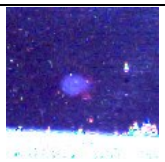	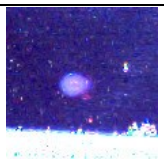	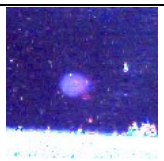	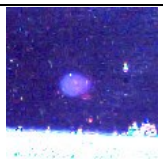
Initial state	After 5 ms	After 10 ms	After 100 ms	After 1 s	After 2 s
Energy: 7.5 mJ	Pulse time: 0.5 ms	Power: 30%	Sample thickness: 100 μm		Focused beam by lens
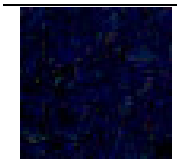	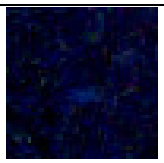	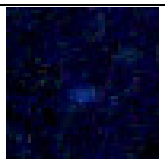	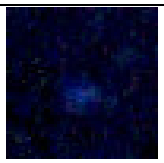		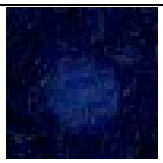
Initial state	After pulse	After 10 ms	After 100 ms	After 1 s	After 2 s
Energy: 12.5 mJ	Pulse time: 0.5 ms	Power: 50%	Sample thickness: 200 μm		Focused beam by lens

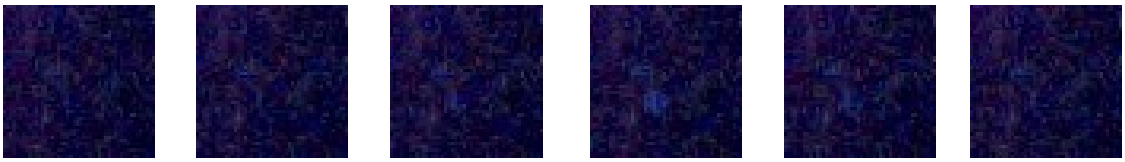

Initial state	After pulse	After 10 ms	After 100 ms	After 500 s	After 1 s
Energy: 5 mJ	Pulse time: 0.5 ms	Power: 20%	Sample thickness: 100 μm		Focused beam by lens

Frames from HSC have been analyzed of mean gray value (MGV) change over time at the illuminated area of the sample to get a more accurate picture of the change in backscattering intensity. Datasets were obtained from software ImageJ[172] by analyzing the frames obtained from HSC. Figure 72a–e shows representative curves for PS-*b*-PNIPAM-BA at different laser pulse energy, $E_{laser\ pulse}$ = 25 mJ – 5 mJ, with their best fits. The temperature jump was induced in the range of ΔT = 3 °C – 10 °C. Curves were fitted by KWW functions, as for analysis in section 3.6.1. In the aggregation process, two-step behavior is observed, where first step describes the cluster formation and the second a cluster aggregation, similarly to RTL experiment. In the case of first step, stretched exponent is fixed with value of β_1 = 2.0 due to a rapid increase of MGV in short time after laser pulse. Curve slop is steeper for first step than at second one because a simultaneous polymer aggregation with water heating at the illumination area. At the second step, the stretched exponent was a free parameter due to the change of slope steep, depending on the laser pulse energy, and it successively decreases from β_2 = 1.0 to β_2 = 0.68. Initial temperature of polymer solution is close to LCST, T^* = 30.0 °C, thus the higher energy causes a deep jump above transition temperature. The aggregation growth is slower than the cluster formation, and with increasing of laser pulse energy, the clusters are formed faster, hence the aggregates growth dominates in second step. Above the transition time, t^*, the polymer solution returns to the transparent state, except for measurement with $E_{laser\ pulse}$ = 25 mJ, where solution after laser pulse remains at two-phase state. Figure 72f shows fit results of characteristic times. Comparing the values of τ_2 from Figure 72f and τ_1 obtained from RL experiment (Figure 67a), they are very close to each other according to the ΔT_{depth}. Therefore, this laser setup can be used to obtain the complementary information within hysteresis range and compare with results from section 3.6.1.

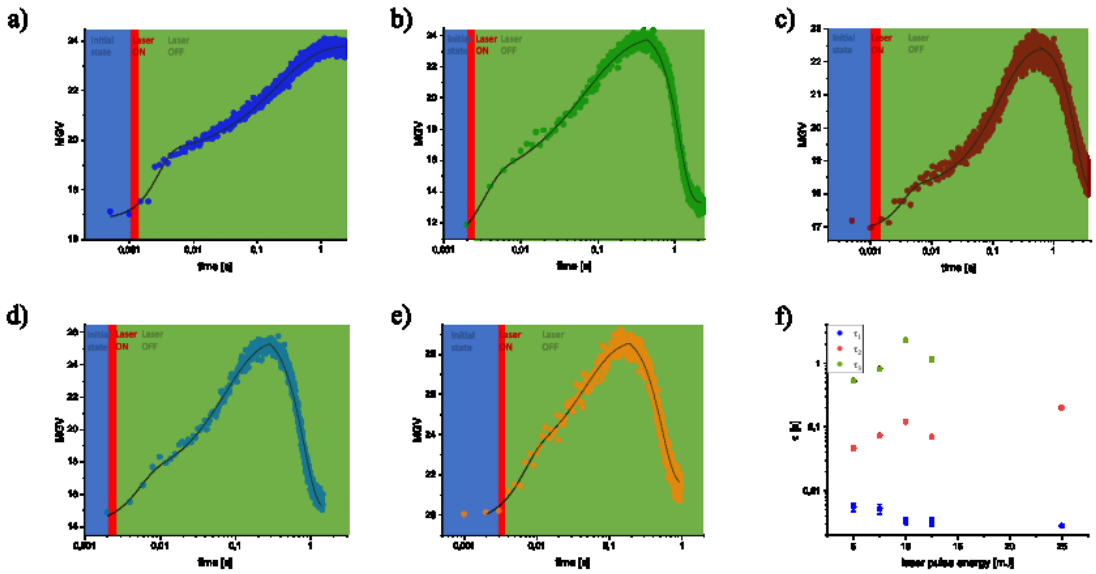

Figure 72. Curves obtained from experiment where T-jump was induced by thulium laser with fixed illumination time, $t_{laser\ pulse}$ = 0.5 ms, and different laser pulse energy, a) 25 mJ, b) 12.5 mJ, c) 10 mJ, d) 7.5 mJ and e) 5 mJ. They were fitted by KWW stretched and compressed exponential function and obtained results of characteristic times are presented in f). Initial temperature of the polymer solution was fixed, T^* = 30.0 °C, for every measurement.

The lowest laser pulse energy, at which the bistability is observed, is $E_{laser\ pulse}$ = 7.5 mJ for linear PNIPAM and PS-*b*-PNIPAM polymers. Slight temperature fluctuations in the hysteresis temperature range can significantly change the swelling behavior. Therefore, additional experiment was performed with PNIPAM-97 polymer fixed laser pulse energy, where the initial temperature of solution was in the hysteresis window. For detailed observation, HSC was used to observe the aggregation process in a short time scale, and a supplementary camera (webcam) for the longer time scale. *T*-jump performed for $T_{initial} = T^* = 32.0$ °C, where bistability in solution is observed, and for $T_{initial} = 30.0$ °C, where solution returns to one-phase state within milliseconds. Figure 73a shows the datasets obtained with HSC and Figure 73b with webcam (frame frequency of 30 fps). In the curves obtained from webcam, due to the jump to higher temperature, aggregation of the polymer into large domains and a high MGV value at maximum point are observed. For shallow jump, the aggregation process is the same as for deep, but the microphase separation is not complete and polymer solution return to swollen state.

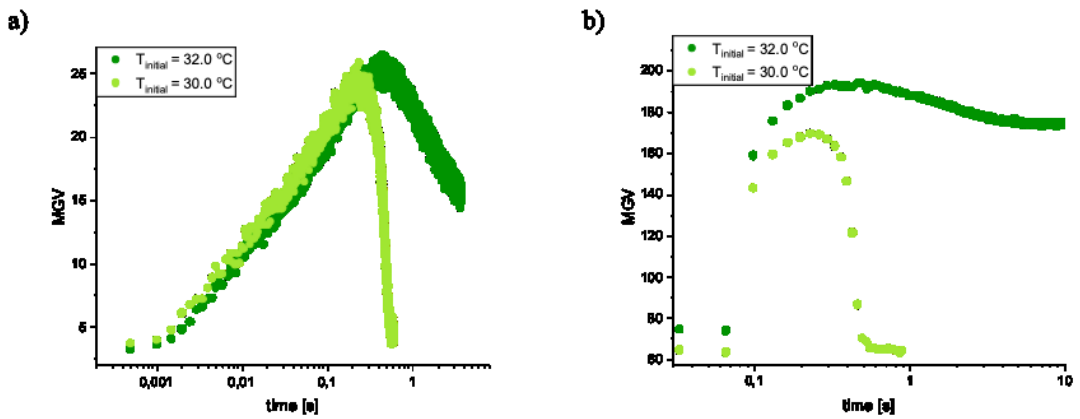

Figure 73. Experimental curves for linear PNIPAM-97 obtained from T-jump induced by thulium laser with pulse time of $t_{laser\ pulse}$ = 0.5 ms and energy $E_{laser\ pulse}$ = 7.5 mJ but with different initial temperature, $T_{initial}$ = 30.0 °C light green, and $T_{initial}$ = 32.0 °C green. Changes of the mean gray value (MGV) were traced by a) HSC and b) webcam to record changes at longer time.

Thulium NIR-laser set for fast temperature jump in polymer solution is a powerful technique to describe the phase transition mechanism across LCST by following the change in backscattering intensity. Obtained datapoints have been fitted by the KWW functions to get the characteristic times for every distinguished step at heating or cooling process, and the values are comparable to results from RL experiments. Thulium laser set, used in this experiment, allows for varying the depth of T-jump above LCST. Therefore, it is possible to determine the lowest energy of the pulse causing the phase transition from temperature in the hysteresis range and to complete the microphase separation in an illuminated spot. Conditions under which long-stay bistability is observed can be estimated by varying not only pulse energy, but also the exposure time, sample thickness, and diameter of the laser beam. The detailed description of behavior across LCST, depending on changes in setup, is shown above, and can be traced over time scale from sub-milliseconds to minutes by HCS and webcam combination. Frames obtained from experiments have been analyzed to change the mean gray value by software ImageJ.

4. Summary and Outlook

The aim of the thesis is to investigate the kinetics of the phase transition of PNIPAM-based linear polymers in a broad time scale. Linear PNIPAM polymer and PS-*b*-PNIPAM copolymers were synthesized by RAFT polymerization due to good control of molecular weight and low polydispersity. Therefore, two polymeric systems were examined with different morphology: polymer coils and micelles.

First, polymers were characterized in detail across the phase transition temperature using turbidity measurement, dynamic light scattering, cryogenic transmission electron microscopy, and small-angle neutron/X-ray scattering. Significant hysteresis was observed for each system, and two-step aggregation and de-aggregation were designated. Based on static measurements, the stability of each step was checked and described, where different experimental methods provide complementary results.

Linear PS-*b*-PNIPAM copolymer self-assembles into micelles in aqueous solution, with a hydrophobic PS-core and a hydrophilic PNIPAM-shell. The phase transition mechanism can be described as follow: at room temperature, the micellar corona is swollen, and upon heating, its size decreases by collapsing; above the transition temperature collapsed micelles aggregate to clusters; next, the clusters start to aggregate and large domains are observed; upon cooling, the size of these domains first grows due to swelling of the PNIPAM-shell and then break down to single micelles. The cluster formation was observed in dilute solution ($c \ll c^*$), and it was found that cluster size could be controlled by temperature. The DLS measurement proved that the clusters consisting of collapsed micelles were formed above T_{VPT} stepwise within the T-range of T_{VPT} + 2 °C. In that range, clusters are monodisperse, as shown by cryo-TEM imaging. With Further temperature increase, clusters aggregate. Cooling the polymer solution in small steps (0.5 °C – 1.0 °C) showed that first, the domains size increases and they have irregular shapes by gradually falling apart into single particles. Regarding large domain formation above LCST, even with dilute concentration, solution temperature has to be decreased by 2 °C – 3 °C below LCST for complete return of polymer particles to the initial state.

The phase transition behavior across LCST for copolymer micelles was compared to linear PNIPAM polymers. The homopolymers were synthesized with different molecular weights, and the phase transition temperature was shifted to a larger value with increasing polymer chain length. For the polymer with Mn = 36.8 kg/mol, the transition mechanism revealed two steps across LCST: polymer aggregation for the heating process and de-aggregation to single coils for the cooling process. In the case of the polymer with Mn = 96.7 kg/mol, the thermo-responsiveness change was similar to that of the copolymer.

The sizes of the individual polymer coils in water are comparable to the micellar size, therefore, linear PNIPAM could be used as a reference for block copolymers.

Regardless of the morphology, all polymers reveal a significant hysteresis, which is related to cluster domain formation above the volume phase transition. Due to the sharp transition across the LCST and the broad hysteresis window, stable one- and two-phase states can be observed in polymer solution. Bistability, remanence, and information storage were successfully demonstrated for linear PNIPAM-based polymers. An AND logic gate was also obtained with a variation of pH and temperature. Information can be written thermally by heated or cooled metal pen tips or using a laser beam, where the writing speed can be minimized to sub-milliseconds. It has been found that the spatial resolution is limited by thermal diffusion, and if excess heat is minimized to pass only the coercive temperature, the size of the two-phase state spot can be reduced to the size of the laser beam. Additionally, an unusual memory function was discovered, where the information storage is based on the intrinsic hysteresis of responsive polymers, it is in principle applicable to a broad range of responsive materials.

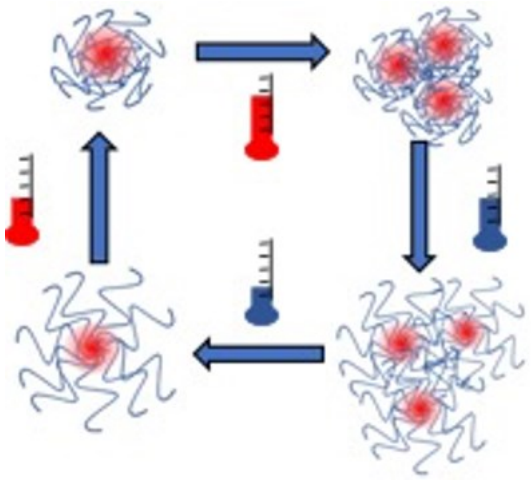

Figure 74. Scheme of phase transition across LCST for linear PNIPAM polymer.

SANS measurements were performed to focus on the temperature influence on a swelling degree of PNIPAM-shell in micelles, in the temperature range of 25.0 °C – – 35.0 °C and semi-dilute conditions (c > c*). Partially collapsed micelles and pre-formed clusters were observed already below the transition temperature. Above LCST, monodisperse clusters were observed in which the distance between collapsed micelles was determined. At 35.0 °C, the size of aggregates was beyond the resolution of experimental settings, so only the size of dehydrated micelles was obtained. Upon heating, the profile of scattering length density contrast between solvent and polymer showed increasing of PNIPAM density thus, dehydration degree could be followed.

The influence of the pressure on to cluster swelling/deswelling process was examined at temperatures above LCST. The temperature-pressure phase diagram for

PS-*b*-PNIPAM was determined. The elliptically shaped coexistence line of one- and two-phase states was obtained, which is in good agreement with previously published studies for linear PNIPAM polymer. At atmospheric pressure, the cloud point for PS-b-PNIPAM-BA in deuterated water is 32.0 °C. With pressure increase, the point is shifted to approx. 33.05 °C at 390 bar. Above this temperature, the solution remains turbid. However, from SANS measurement, even at T = 33.5 °C, changes in the PNIPAM-shell thickness were detected with pressure increase. Thanks to this experiment, only the responsiveness of PNIPAM-shell was observed for transition from two- to one-phase state.

Two experimental methods were used to study the kinetics of the phase transition caused by rapid temperature jump: tr-SANS and NIR-laser setups. The PNIPAM-shell thickness upon temperature jump from 25.0 °C to 35.0 °C was followed for PS-*b*-PNIPAM micelles by tr-SANS with a stopped-flow device, at which the T-jump was induced in milliseconds time range. After solution injection to observation cell, the micelles were partially collapsed and over time, the slow dehydration of PNIPAM-shell and cluster growth were observed. The aggregation kinetics of clusters was investigated for two polymer concentrations (c_1 = 1 mg/mL and c_2 = 5 mg/mL) and significant differences were observed. At low concentration, aggregation was described as a diffusion-limited colloid aggregation, for high concentration within the first 2 seconds, the overlap of DLCA and RLCA kinetics is observed, whereas at later times RCLA dominates. Therefore, the kinetics of phase transition strongly depends on whether polymer concentration is in a dilute or semi-dilute regime.

The second method was used to examine optical transmittance changes to obtain a general picture of the thermal sensitivity for linear PNIPAM-based polymers. The solution was heated in nanoseconds with the NIR-laser setup, after which the polymer responsiveness was followed in real time. The measurements were performed with three laser configurations: 1. Raman laser to rapidly heat the solution (RL experiment), 2. Raman-thulium laser to rapidly heat the solution and keep the higher temperature within 9 s (RTL experiment), and 3. thulium laser, to heat the solution in sub-milliseconds with initial temperature in hysteresis range.

For configurations 1. and 2., the measurements were performed for a wide $T_{initial}$ range to cover shallow and deep jumps above the phase transition temperature. For a single laser pulse, the temperature returned to the starting point. Therefore, the swelling process was also observed. Three polymers were studied to check the influence of the polymer morphology on the phase transition kinetics. In the case of polymer coils and micelles, the kinetics mechanisms were very similar. However, the difference in end-groups between copolymers revealed discrepancies in the characteristic time values. The copolymer with dodecyl end-groups, due to its hydrophobic structure, can create bridges between micelles, which affect the rate of change of the solution turbidity. Hence, the kinetics results obtained for PS-*b*-PNIPAM-C_{12} can describe the collapsing process, which was difficult to obtain

for PS-*b*-PNIPAM-BA and PNIPAM-36. According to the experiment with the 3. configuration, the temperature jump was induced from temperatures in the hysteresis range, and the backscattering intensity change was followed by a high-speed camera. The T-jump was controlled by laser pulse parameters, such as energy or illumination time. Therefore, the influence of the jump depth on the phase transition kinetics was designated and the minimum conditions to cause the bistability were determined.

Apparent activation energies of phase transition for polymers were calculated from characteristic relaxation time of cluster formation. The results showed that the lowest energy is needed in the case of copolymer with dodecyl end-group and the highest for linear homopolymer. That can be explained by the solvation layer thickness around PNIPAM polymer in the swollen state and the number of possible H-bonds between solvent and polymer. Due to polymer chain assembly to micelles, the PNIPAM block creates fewer hydrogen bonds with water compared to a polymer coil due to the spatial limitation. Water can attach to the polymer all over the chain in the case of homopolymer. Thus, more energy is needed to break most H-bonds between water and polymer to induce the phase transition.

In conclusion, this thesis provides a detailed description of the phase transition kinetics for linear PNIPAM-based polymers. Different experimental techniques have been applied to identify stepwise aggregation and de-aggregation processes across the LCST. Moreover, an unusual behavior within hysteresis temperature range was discovered for simple linear polymers, such as bistability or memory function in storage information. The results can be used to compare the thermo-sensitivity of more complex PNIPAM-based materials.

5. Materials and Experimental Procedures

5.1. Materials

The monomers N-isopropylacrylamide (NIPAM, ≥99%), styrene (St, ≥99%), n-Butyl acrylate (BA, ≥99%), RAFT agents such as 2-(Dodecylthiocarbonothioylthio)-2-methylpropionic acid (DDMAT, 98 %) and 2-Cyano-2-propyl dodecyl trithiocarbonate (CPDT, 97 %), the initiator 2,2-Azobis(2-methylpropionitrile) (AIBN, 98 %) and solvents 1,4-Dioxane (> 99 %) and methanol (> 99 %) were purchased from Sigma-Aldrich (Germany). Styrene was distilled under pressure (3 mbar, 120 - 130 °C) prior to use to remove 4-tert-butyl catechol stabilizer. Solvent 1,4-Dioxane was distilled under pressure (3 mbar, 100 °C) before polymerization. RAFT agents were degassed on vacuum line overnight (3 mbar) and stored in fridge in glovebox. For the Michael addition reaction, compounds N-hexylamine (99 %) and Tris(2-carboxyethyl) phosphine hydrochloride (TCEP) were purchased from Sigma Aldrich and used as received. Tetrahydrofuran (THF, 99.7 %), n-hexane (96%) and diethyl ether were purchased from VWR (Germany). NIPAM, n-Butyl acrylate, AIBN, THF, diethyl ether and methanol were used as received. Water for all purposes was purified using Millipore-Q system. For the SANS experiments, samples were prepared in deuterated water with deuteration degree of 99 % from Sigma Aldrich.

5.2. Synthesis of the polymers

Polymers for thesis were synthesized by RAFT polymerization with Trithocarbonate as RAFT agents (Figure 75). They are used to polymers “more activated” monomers (MAM’s), which have their vinyl group conjugated to an aromatic ring (e.g., styrene), a carbonyl group (e.g., (meth)acrylamides), a double bond (e.g., isoprene) or a nitrile (e.g., acrylonitrile).[173] They are less active than other RAFT agents, thus provide a good control over synthesis and they give less retardation and less prone to hydrolytic degradation.[174]

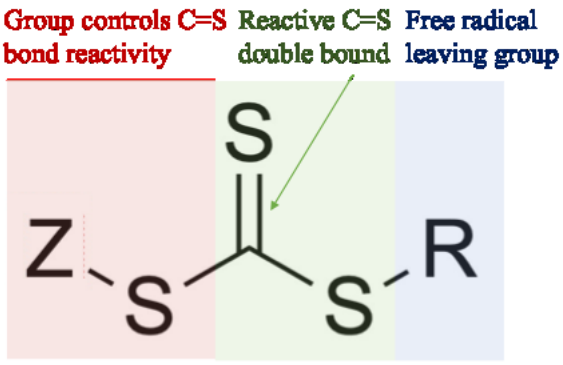

Figure 75. Structure of trithocarbonate RAFT agent.

Due to good control of polymer molecular weight with RAFT synthesis, *Eq.49.*, was used to calculate the theoretical molecular weight of polymer chain before polymerization. $[M]_0$ and $[CTA]_0$ are initial concentrations of monomer and RAFT agent (chain transfer agent), respectively, p is monomer conversion and M_M and M_{CTA} are molar masses of monomer and RAFT agent, respectively.[173]

$$M_{n,theo} = \frac{p[M]_0 M_M}{[CTA]_0} + M_{CTA} \qquad (Eq.49.)$$

5.2.1. Synthesis of Polystyrene (PS) core

Before polymerization, solvent (1,4-Dioxane) and monomer (styrene) were purified by distillation and transfer to glovebox where were stored. The reaction is air sensitive, thus reagents were prepared and placed to the flask in glovebox. The synthesis of polystyrene (PS) core was done with RAFT polymerization in 100 mL round-bottom flask with stirring bar. Monomer styrene (0.03 mol), RAFT agent DDMAT (1.1 mmol) and initiator AIBN (0.38 mmol) were dissolved in solvent 1,4-Dioxane (6 mL). Next, flask with reagents was transfer to vacuum line where before reaction was started the solution was degassed and put to preheated to 65 °C oil bath and magnetic stirrer (stirring at 400 rpm). Temperature of 65 °C was kept for the whole synthesis. The reaction was started when solution reached temperature of 65 °C. After 20 h of stirring at 65 °C the reaction stopped by putting the flask with solution to ice water for 15 min and put to reach a room temperature. Final solution was thick thus was added small amount (4 mL) of THF. Next, product was precipitated in methanol, centrifuged, and again dissolved in THF. The precipitation and washing procedure were repeated twice. Final product was dried on vacuum line overnight and store in vacuum oven over a few days.

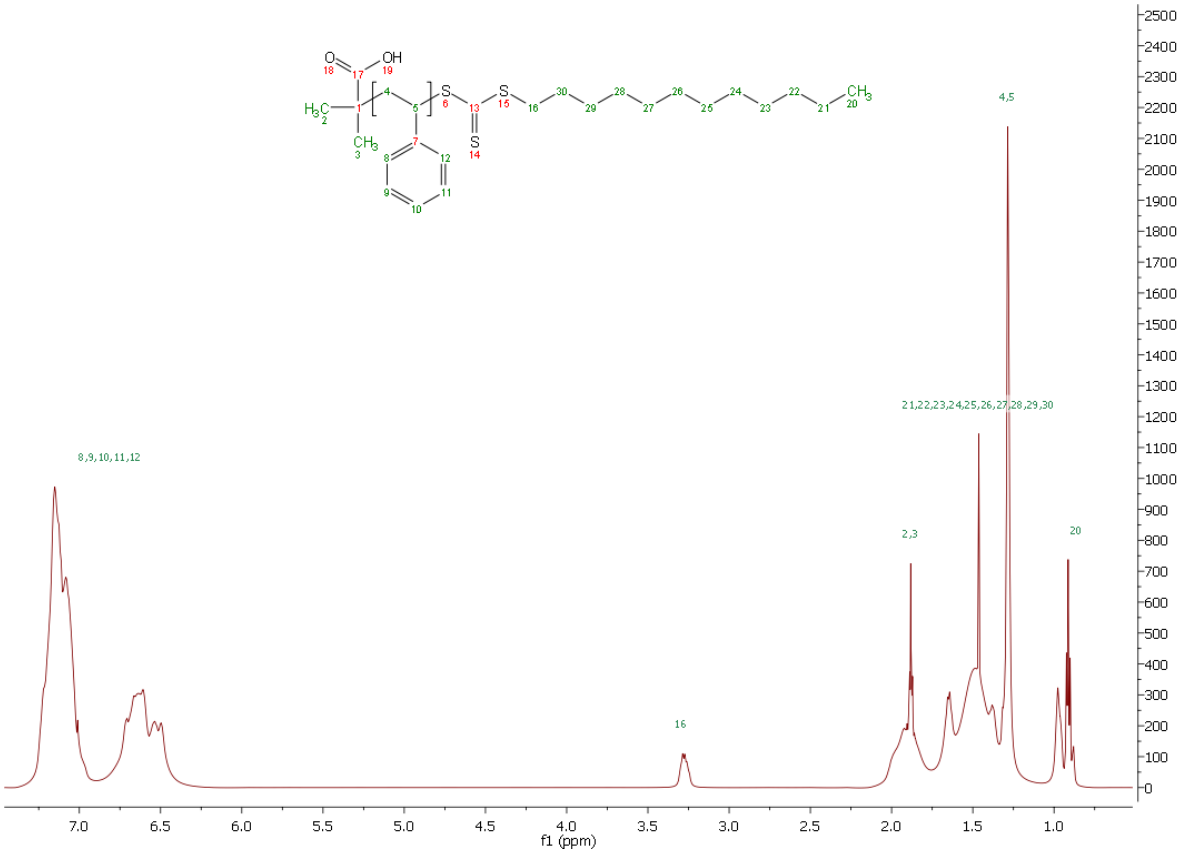

Figure 76. ^{1}H NMR spectrum of polystyrene (PS) polymer in $CDCl_3$.

5.2.2. Synthesis of Poly(N-isopropylacrylamide) (PNIPAM) shell

The PNIPAM shell of block copolymer PS-*b*-PNIPAM-C_{12} was synthesized with RAFT polymerization and macro-CTA as earlier polymerized PS with DDMAT RAFT agent (PS-TTC). Reagents were prepared and placed to 100-mL round-bottom flask with teflon stopper and stirring bar in glovebox. Monomer NIPAM (30 mmol), macro-CTA PS-TTC (0.156 mmol) and initiator AIBN (0.011 mmol) were dissolved in solvent 1,4-dioxane (8 mL). Flask with reagents were transfer to vacuum line where solution was degassed and put to preheated (to 65 °C) oil bath on magnetic stirrer (stirring at 400 rpm) and polymerization was started. Temperature of 65 °C was kept for the whole synthesis. After 3h reaction was stopped by putting the flask to ice water for 15 min. Final solution was yellowish. When solution reached room temperature, it was thick thus was added approx. 4 mL of THF to dissolve it and next product was precipitated in cold diethyl ether, centrifuged, and dissolved in THF again. The precipitation and washing procedure were repeated twice. Final product was dried on vacuum line overnight and store in vacuum oven over a few days. Completely dry product was store in the freezer.

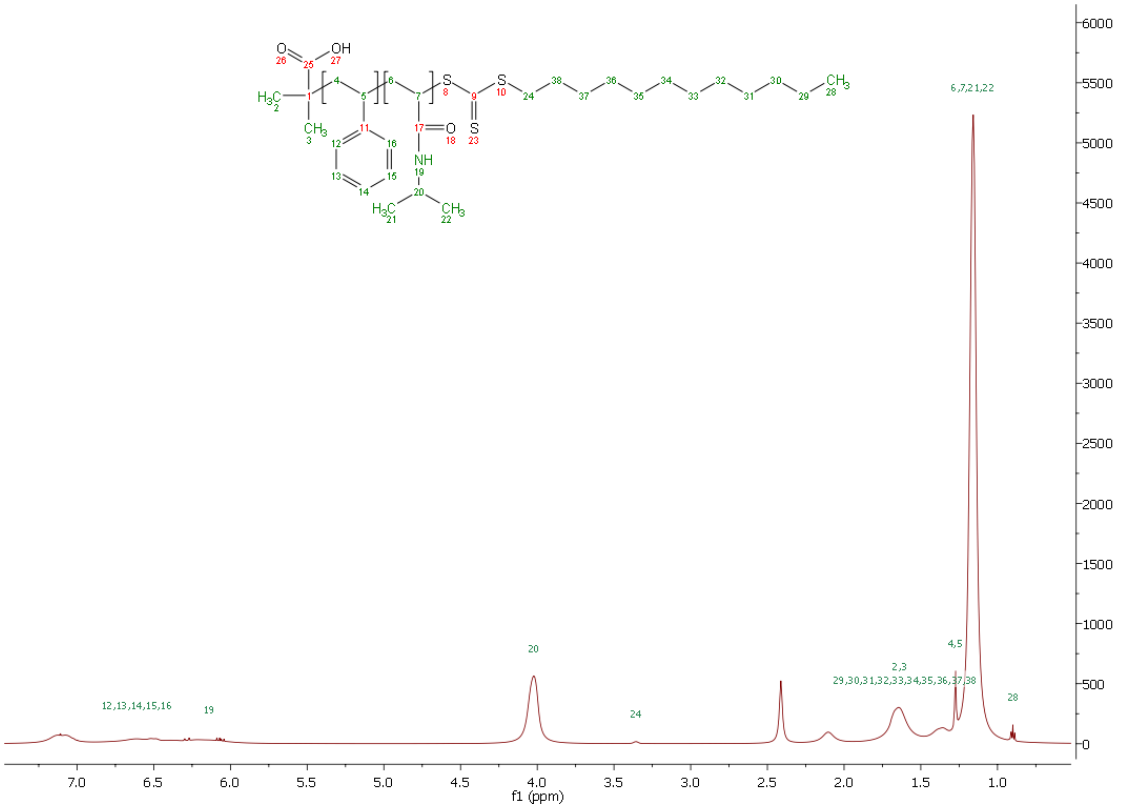

Figure 77. ^{1}H NMR spectrum of PS-b-PNIPAM-C_{12} polymer in $CDCl_3$.

5.2.3. End group modification in block copolymer PS-*b*-PNIPAM-C_{12}

Changing of end group in block copolymer PS-*b*-PNIPAM-C_{12} was done by aminolysis and Michael addition reaction. In the final product, the dodecyl end group was changed to a n-butyl acrylate. Dried polymer PS-*b*-PNIPAM-C_{12} was dissolved in THF (approx. 6 mL) in round-bottom flask (100 mL) and stirring bar. To block copolymer solution (0.03 mmol) was added N-hexylamine (1.30 mmol) and reducing agent TCEP (0.06 mmol). Mixture was stirred at 500 rpm for 2h under argon atmosphere and at stirring time solution color change from yellow to colorless. After 2h to the mixture was added n-butyl acrylate (1.8 mmol) and stirring under argon condition was continued for 20h in room temperature. Product was recovered and purified by three reprecipitation from THF to diethyl ether and centrifugation. Final product was dried overnight on vacuum line and next a few days in vacuum oven. Completely dry product was store in the freezer.

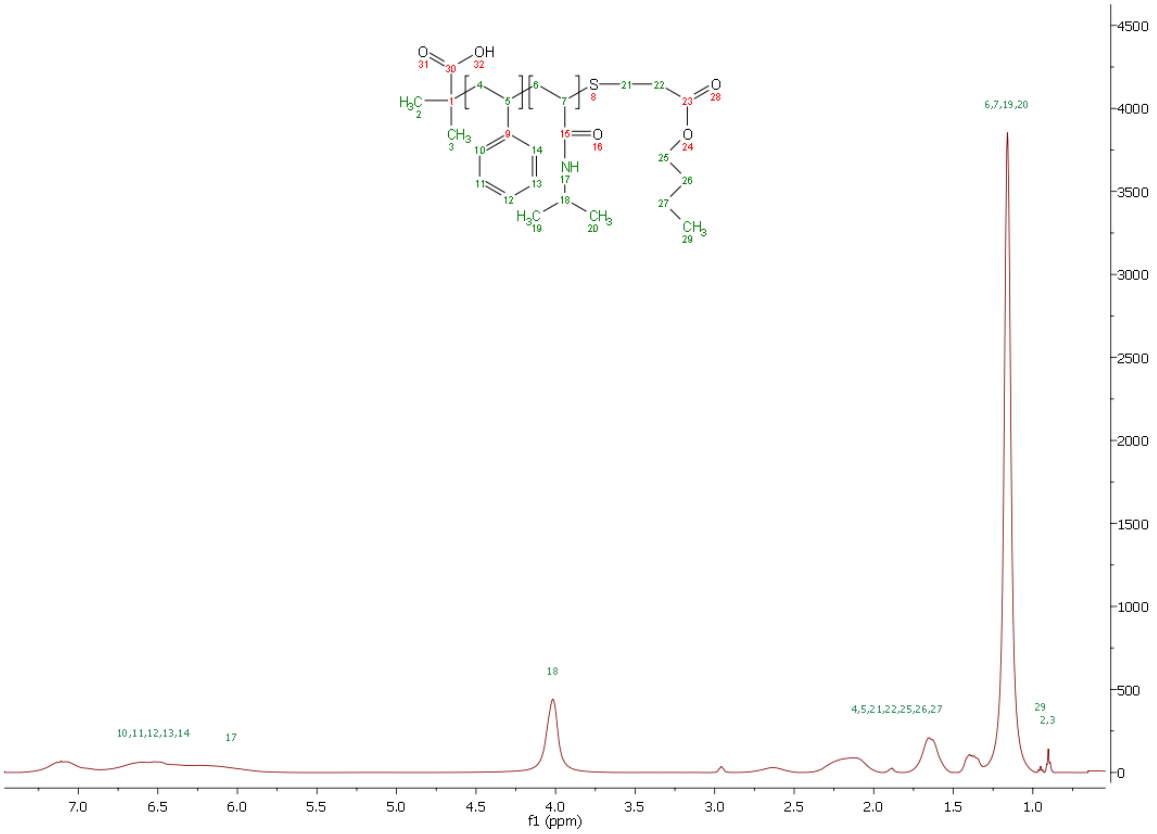

Figure 78. ^{1}H NMR spectrum of PS-b-PNIPAM-BA polymer after substitution with n-butyl acrylate as an end group in $CDCl_3$.

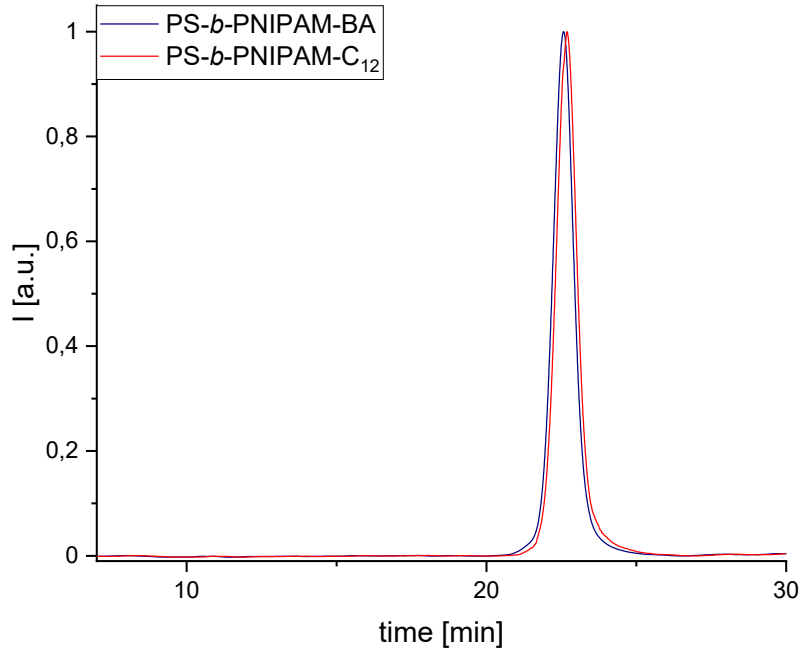

Figure 79. SEC trace of block copolymer PS-b-PNIPAM-BA.

Table 6. Molecular weight and polydispersity of linear block copolymers.

Name	PS-*b*-PNIPAM-C_{12}	PS-*b*-PNIPAM-BA
Molecular mass of PS-TTC block	1.99	1.99
Molecular weight [kg/mol]	17.0	17.0
RAFT agent	DDMAT	DDMAT
PDI	1.04	1.04

5.2.4. Synthesis of Poly(N-isopropylacryl amide) (PNIPAM) homopolymer

The homopolymer PNIPAM was synthesized with RAFT polymerization. The synthesis procedure is the same as for previous polymers. Reagents were placed to 100 mL round-bottom flask with teflon stopper and stirring bar in glovebox to avoid the oxygen contamination. Monomer NIPAM, RAFT agent CPDT/DDMAT and initiator AIBN were dissolved in solvent 1,4-dioxane (approx. 15 mL). Flask with mixture was transfer to vacuum line where solution was degassed, and polymerization was started by putting the flask to preheated (to 65 °C) oil bath on magnetic stirrer (stirring at 400 rpm). Temperature of 65 °C was kept for the whole synthesis. After 3h, polymerization was quenched by inserting the flask to ice water for 15 min and next it was left to reached room temperature. Solution was diluted by adding a few mL of THF. Product was precipitated in cold diethyl ether, centrifuged, and dissolved in THF again. The precipitation and washing procedure was repeated three times. Final product was dried on vacuum line overnight and store in vacuum oven over a few days.

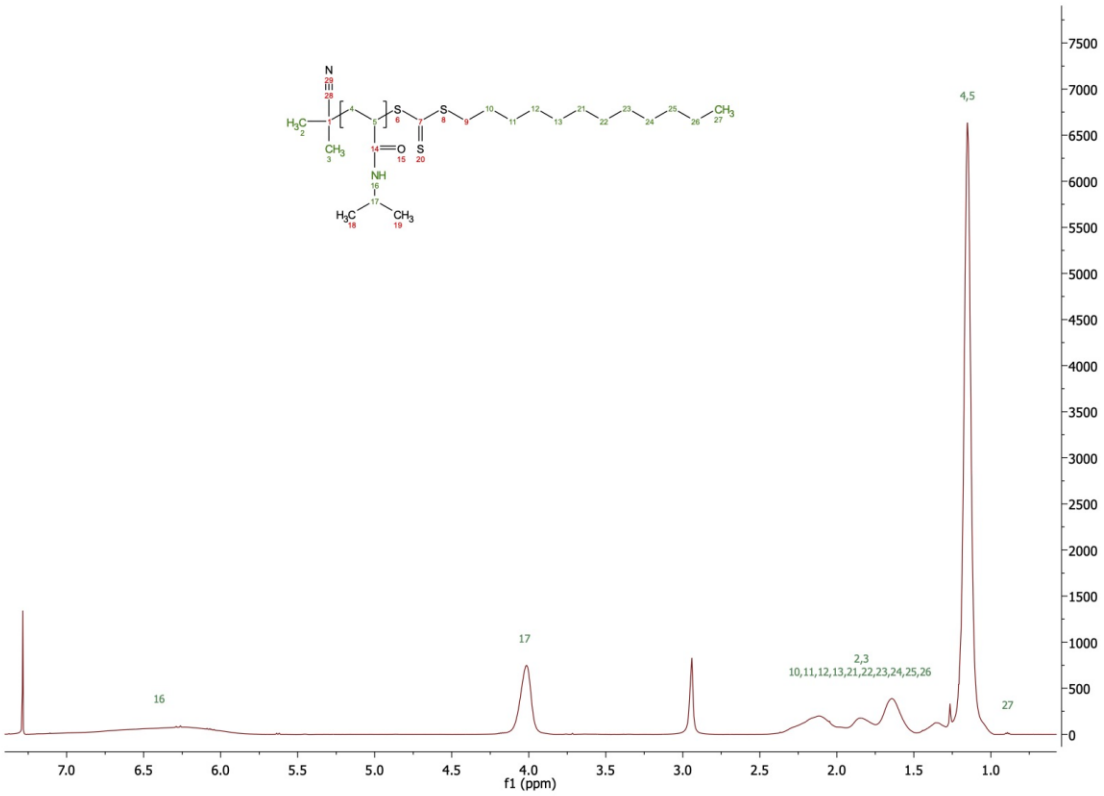

Figure 80. ^{1}H NMR spectrum of PNIPAM polymer in $CDCl_3$.

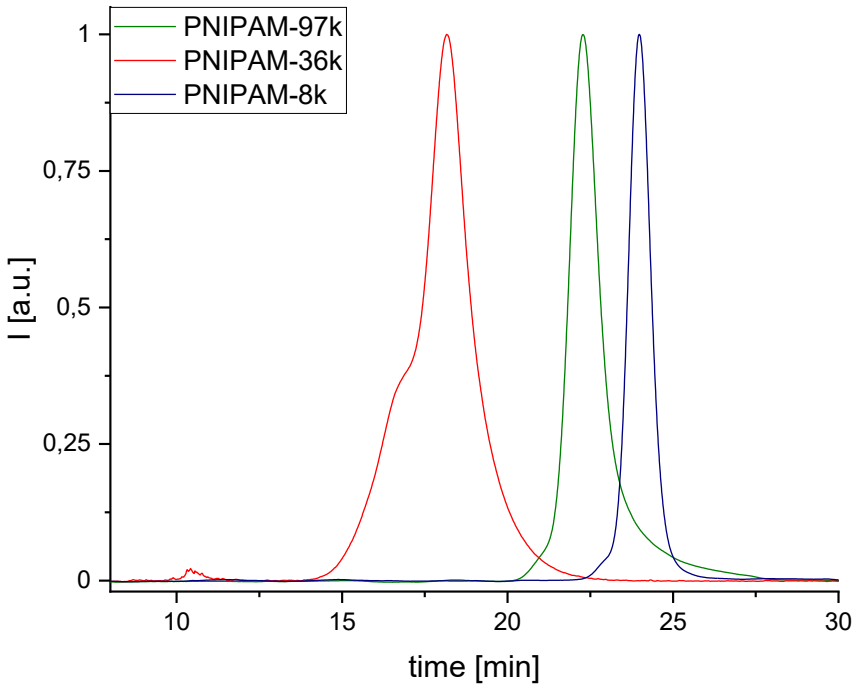

Figure 81. SEC trace of linear PNIPAM polymer with different molecular weight, red – M_w = 96.7 kg/mol, green – M_w =36.8 kg/mol and blue – M_w = 8.2 kg/mol.

Table 1. Molecular weight and polydispersity of linear PNIPAM polymers.

Name	PNIPAM-97	PNIPAM-95-TTC	PNIPAM-36	PNIPAM-8
Molecular weight [kg/mol]	96.70	95.60	36.80	8.20
RAFT agent	CPDT	DDMAT	CPDT	DDMAT
Conversion	57 %	88%	96%	100%

5.3.Sample preparation

Polymer solutions were prepared in MilliQ water, for neutron scattering experiment it was prepared in deuterated water, D_2O. Purified polymer powder was dissolved in water by mixing on magnetic stirrer for 7 days or 1 day in ice bath for block copolymer PS-*b*-PNIPAM or homopolymer PNIPAM, respectively. Samples were stored in fridge (+4 °C) over months and no changes was observed.

5.4.Characterization of the polymers

5.4.1. Nuclear magnetic resonance (NMR)

The structure of polymers after polymerization was characterized by nuclear magnetic resonance. The 1H NMR spectra were collected with a Bruker AC 250 (300 MHz) and a Bruker Avance III (600 MHz) spectrometer, which is equipped with a Prodigy cryoprobe. Samples were dissolved in chloroform-d3 and measured at 295 K.

5.4.2. Size Exclusion Chromatography (SEC)

The molecular weight (M_n) and molecular weight distribution ($^{M_w}/_{M_n}$) of the polymers were established by size exclusion chromatography. SEC measurements were done on Agilent 1260 Infinity GPC/SEC system, Shimadzu CTO-20AC column oven, three Agilent PlusPore GPC columns with a continuous pore size distribution, a differential refractive indext (Wyatt Optilab T-rEX) and light scattering detector (Wyatt DAWN Heleon-2). As the eluent was used mixture of tetrahydrofuran/*N,N*-dimethylacetamide (85/15) at 50 °C and with flow rate of 1 mL/min. The polymer solution for measurements was prepared by

dissolving of 3.5 mg of synthesis product in a 1.5 mL of solvent mixture THF/DMA/AcOH. For the data evaluation was used ASTRA 7.3. software.

5.4.3. Turbidity measurement

Could point and hysteresis range determination was carried out on UV-Vis spectrometers Perkin Elmer Lambda 40 with Luda RC6 thermostat and on FluoroMax spectrofluorometer (HORIBA) with thermostated chamber. Experiments were performed at the wavelength of 560 nm in UV Quart cuvettes with the path length of 1 mm and at temperature range of 20 °C – 40 °C for the heating - cooling cycle at rate of 1 °C/min. Spectra were recorded with HORIBA Jobin Yvon Fluorolog. The transition points were determined for the middle value of transmittance (%T) after abrupt decrease or increase of %T value.

5.4.4. Dynamic light scattering (DLS)

Systematic investigation of the hydrodynamic radii of PNIPAM coils and PS-*b*-PNIPAM-BA micelles, depending on the temperature, was done by dynamic light scattering. In this technique are measured the fluctuations of the scattering intensity in highly diluted samples are related to the Brownian motions of the particles due to interference of the scattered light waves depends on the particle position in relation to each other. Experimentally, the dynamic information of particles can be obtained from autocorrelation of intensity change. The exponential decay in related to the motion (diffusion coefficient) of particles in dilute solution. By the Siegert's relation (*Eq.50.*),[175] the translational diffusion coefficient (*D*) can be designated from decay of normalized intensity correlation function ($g^{(2)}(\tau)$). In the equation *Eq.50.*, q is a particular wave vector, τ is a delay time, I is an intensity and β is a correction factor of coherence and laser optics.

$$g^{(2)}(\tau) = \frac{\langle I(t)I(t+\tau)\rangle_t}{\langle I(t)\rangle^2} = 1 + \beta e^{-Dq^2\tau} \qquad \textit{(Eq.50.)}$$

Measurements were performed on a light scattering setup with ALV/CGS-3 goniometer system and ALV-7004 USB Multiple Tau Digital Correlator covering a range of scattering angle $20° \leq \theta \leq 151°$ (Figure 82). As laser Nd-YAG laser ($\lambda = 532\ nm$) was used. Samples were prepared in H_2O with a concentration of 0.1 mg/mL. Experiments were performed for temperature range 25.0 °C – 40.0 °C and temperature step of 2.0 °C – 1.0 °C, close to transition temperature the change step was 1.0 °C – 0.5 °C, repeated twice.

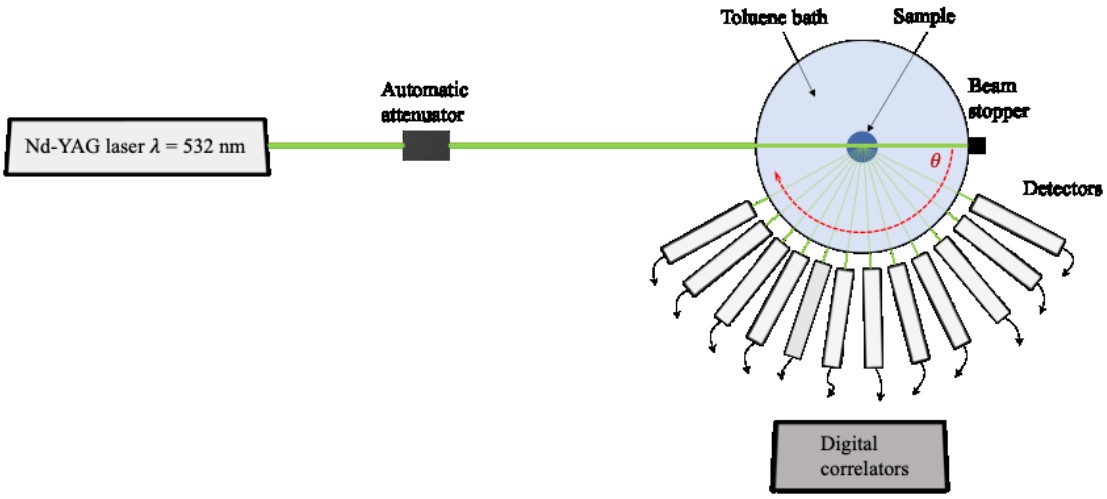

Figure 82. Experimental setup for dynamic light scattering.

For the data analysis CONTIN algorithm was used to obtain a decay rate (Γ), which is related to D, $\Gamma = -Dq^2$. With Stokes-Einstein equation (*Eq.51.*) the hydrodynamic radius was calculated, where k_B is a Boltzmann constant, T is absolute temperature and η is a solvent dynamic viscosity.[176]

$$R_H = \frac{k_B T}{6\pi\eta D} \qquad \textit{(Eq.51.)}$$

5.4.5. Cryogenic Transmission electron microscopy (cryo-TEM)

The morphology of polymers in "frozen-hydrated" state was investigated by transmission electron microscope JEOL JEM-F200 (200 kV). Samples of aqueous polymer solutions with concentration of 0.5/1 mg/mL for cryo-TEM were prepared on Vitrobot MK IV. For measurements were used TEM Quantifoil grids (hole shape R3.5-1, 200 mesh, Cu or MultiA, 200 mesh, Cu) and the samples were prepared in temperature range of 25.0 °C – 37.0 °C. In the climate chamber of Vitrobot, the grids and sample were thermostated approx. 7–10 min. before sample application. For blotting and vitrification were used the same conditions for all samples, 6 s of blotting time and -5 or 0 of blot force. The blotting process is immediately followed by rapid vitrification of the grid to liquid ethane. Prepared grids with thin layer of frozen polymer solution were stored in liquid nitrogen (LN_2) before measurement. For insertion the grid to microscope was used a cryo-transfer holder (Fischione Ins., model 2550). The images were recorded digitally by bottom mounted camera system TemCam-XF416 CMOS, TVIPS.

5.5. Structural changes across LCST

5.5.1. Small-angle X-ray scattering

Small-angle X-ray scattering was used to distinguish the sizes of core and shell in PS-*b*-PNIPAM-BA micelles in swollen state. Scattering patterns was recorded with the SAXS system "Ganesha-Air" from (SAXSLAB, Xenocs). The X-ray source of this laboratory-based system was a D2-MetalJet (Excillum) with a liquid-metal anode operating at 70 kV and 3.57 mA with Ga-Ka radiation (λ = 0.1341 nm) providing brilliant and small beam (<100 μm). The beam was focused with a focal length of 55 cm using a specially made X-ray optic (Xenocs) to provide small and intense beam at the sample position. Measurements were done in 2.1 mm boronsilicate glass capillaries (Hilgenberg) at T = 25.0 °C, and the transmitted intensity data were recorded by a position-sensitive detector (PILATUS 300 K, Dectris). To cover the range of scattering vectors between 0.026 nm^{-1} and 3 nm^{-1}, different detector positions were used. The circularly averaged data were normalized to incident beam, sample thickness, and measurement time before subtraction of the solvent. All measurements were put on an absolute scale by standard-less absolute intensity calibration.

5.5.2. Small-angle neutron scattering

5.5.2.1. Temperature variation

Small-angle neutron scattering static and kinetic measurements at different temperatures were performed on KWS-1[177] at the Heinz Maier-Leibnitz Zentrum (MLZ) in Garching, Germany (Figure 83). The measurements were performed with unpolarized, monochromatic incident beam with neutron wavelength of $\lambda = 4.93$ Å with $\Delta\lambda/\lambda = 10\%$ wavelength resolution and for three sample-to-detector distances (SDD) of 2.3 m, 8.0 m, and 20.0 m, and two collimation distances of 8 m and 20 m, to cover a q-range of 0.033 – 4 nm^{-1}. Polymers were prepared in deuterium oxide to provide a good contrast between water-rich and polymer-rich phases at the measurement. The samples were measured in quartz cells with a thickness of 2 mm for static and 1 mm for kinetics experiment. The intensities in all data were calibrated regarding to standard sample (Plexi glass), transmission, sample thickness, noise from a surrounding, empty cell, and solvent by QtiKWS software[178] to get data in absolute scale. They were analyzed by Jscatter progam[179] using Python.

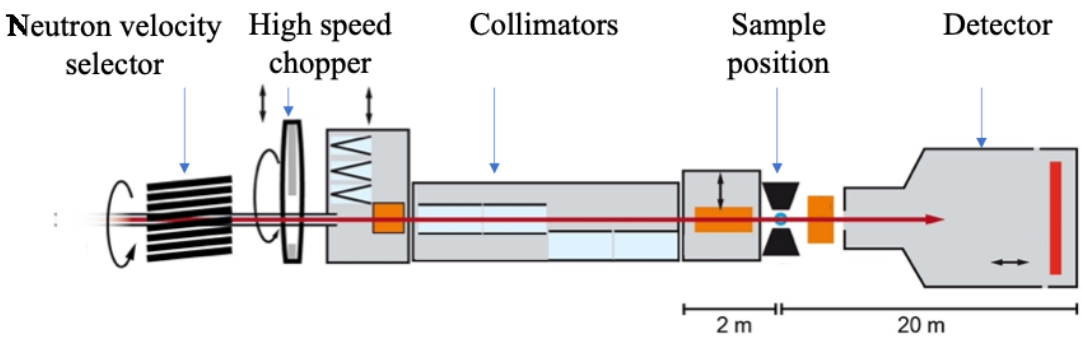

Figure 83. SANS instrument scheme of KWS-1[177] *in MLZ Garching.*

At the static measurement, cells were mounted in temperature-controlled sample holder, which had water circulating thermostat (Julabo GmbH, Germany). The measurements were done at T = 25.0 °C and T = 35.0 °C. The kinetics measurements were performed with stopped-flow device (detailed description below) to induce a temperature jump from 25.0 °C to 35.0 °C. Data were collected for different accumulation times, from 0.1 s and increased with a time factor of 1.05, during 15 min. For the first second was collected 10 frames, at the end of measurement was collected 125 frames for one jump. T-jumps were reaped three times for SDD of 2.3 m and 8 m, and five times for SDD of 20 m for the good statistic.

5.5.2.1.1. Stopped-flow device

Stopped-flow device with mT jump system (SFM-4000, BioLogic) was used for SANS experiment to induce the temperature jump in polymer solution in millisecond time range. Scheme of the device is presented in Figure 84. Temperature jump was performed by mixing the hot water with polymer solution in ration 1:1 with mixer localized directly under cell. The polymer solution was kept in capillary A with T = 25.0 °C and water was kept in capillary B with T = 45.0 °C, and both are placed between syringes and mixer. Temperature in capillaries was controlled by Peltier elements. Final temperature in observation cell is calculated from initial temperatures and mixing ration and controlled in thermostated cell holder. Injection of the solution to cell with deadtime (needed for mixing) approx. 10 ms triggered starting of SANS measurement. The volume of injected solution was approx. of each component. After every measurement, cuvette was washed by 2 mL of D_2O.

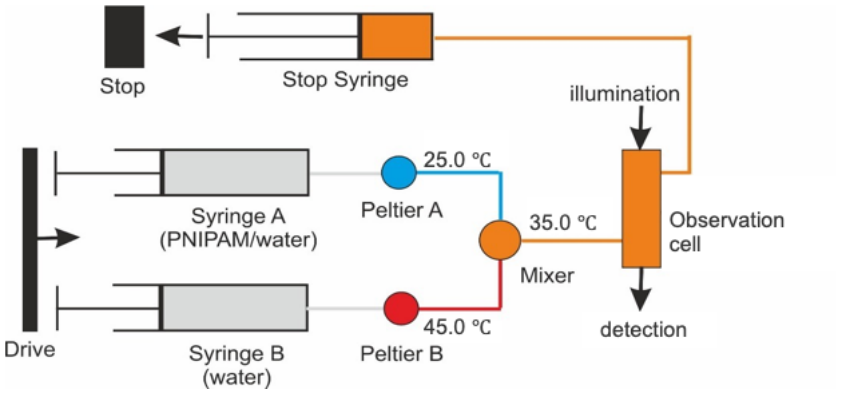

Figure 84. Scheme of stopped-flow device used for temperature jump experiment on SANS.

5.5.2.2. Pressure variation

Small-angle neutron scattering at different pressure was performed on D11[180] at Institute Laue-Langevin (ILL) in Grenoble, France. The measurements were performed with incident beam with neutron wavelength of $\lambda = 6.0$ Å with $\Delta\lambda/\lambda = 9$ % wavelength resolution and for three SDD of 3.0 m, 8.0 m, and 34.0 m to cover a q-range of 0.016 – 3.2 nm^{-1}. For the experiment was used a temperature–controlled custom-made copper-beryllium (CuBe) pressure cell. Sample was placed between two sapphire windows with thickness of 2 mm and was isolated from pressure transmitted medium by movable piston as a separator.[181] Pressure in cell was changed by pressure generator. The temperature of the cell was controlled by water circulating thermostat Julabo F12 and Pt100 resistance thermometer attached to the cell. The intensities of the data were subtracted by the empty pressure cell, solvent, and dark current measuring boron carbide to get data in absolute scale.

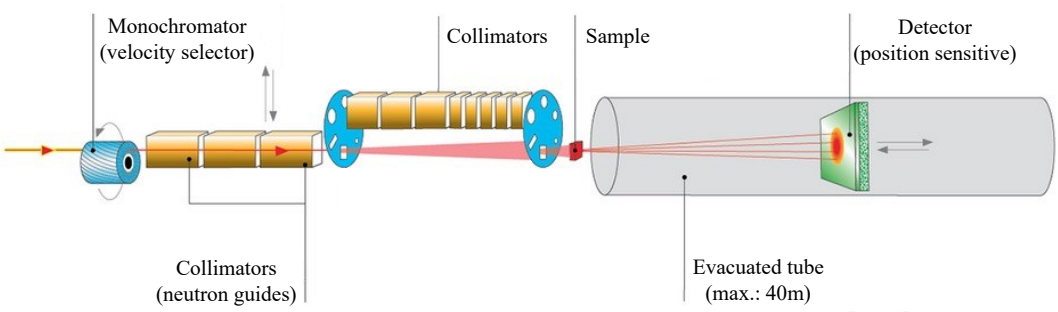

Figure 85. SANS instrument scheme of D11[180] in ILL Grenoble.

5.5.2.2.1. Turbidimetry

The temperature-pressure phase diagram for polymer solution was performed with pressure cell setup (described above) and 10 mW HeNe laser with wavelength λ= 633 nm and photodiode detector. Temperature of the cell was controlled by water circulating thermostat Julabo F12 and thermometer attached to the cell. On the phase diagram are presented points indicating the temperature and pressure for which transmittance decreased/increased significantly, which marked the phase transition. After temperature or pressure change, it was waited till value of transmittance was stable. The pressure was changes with step 25–50 bar and temperature with step 0.2 – 0.5 °C.

5.5.3. Fast temperature jump induced by Raman/Thulium laser setup

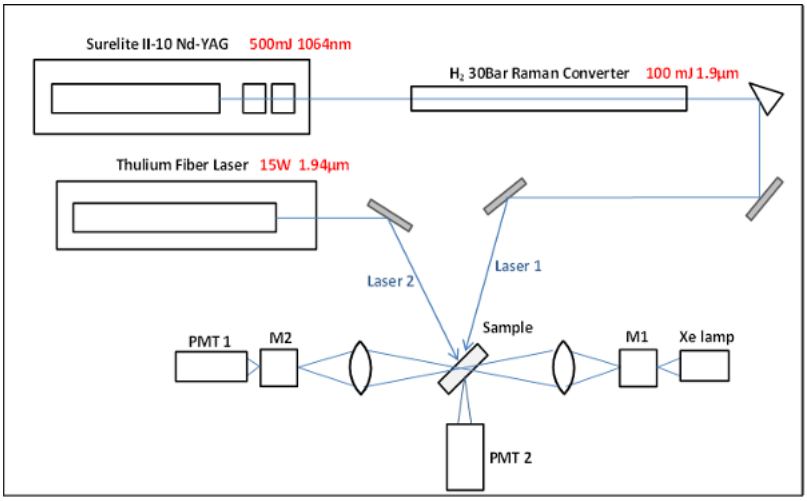

Figure 86. Optical layout of the NIR-laser jump experiment consisting of a Nd:YAG/H_2-Raman converter laser to induce 10 ns temperature jumps of up to 10 °C and a Th-fiber laser to keep the plateau temperature for up to several minutes.

Fast temperature jump induced by Raman/Thulium laser was performed in Institute of Biophysical Chemistry (Hannover Medical School) with dr Igor Chizhov. The setup for the NIR-laser temperature jump experiments is schematically shown in Figure 86. It consists of a Nd:YAG laser operating at a wavelength of λ = 1064 nm, which is shifted to a wavelength of λ = 1960 nm using a H_2-Raman converter. The laser setup induces 10 ns temperature jumps of up of 10 °C due to the high absorption coefficient of water in the NIR-region. Thermal diffusion will lead to a noticeable temperature decrease in the illuminated volume after ca. 10 ms, which is compensated by a thulium-fiber laser (TLR-15-1940; IPG Laser GmbH) operating at a wavelength of λ = 1940 nm to keep the temperature at a steady value for up to several minutes.

The detection system is also schematically shown in Figure 86. It consists of a Xe-lamp with a monochromator, a photomultiplier tube PMT1 with a monochromator for the transmission experiments M1, and a photomultiplier PMT2 with a cut-off filter for the scattering and fluorescence experiments. The time resolution of the photomultipliers allows following changes in the transmission, scattering and fluorescence signal over time scales from 100 ns to 1000 s.

5.5.4. Temperature jump induced by Thulium laser setup

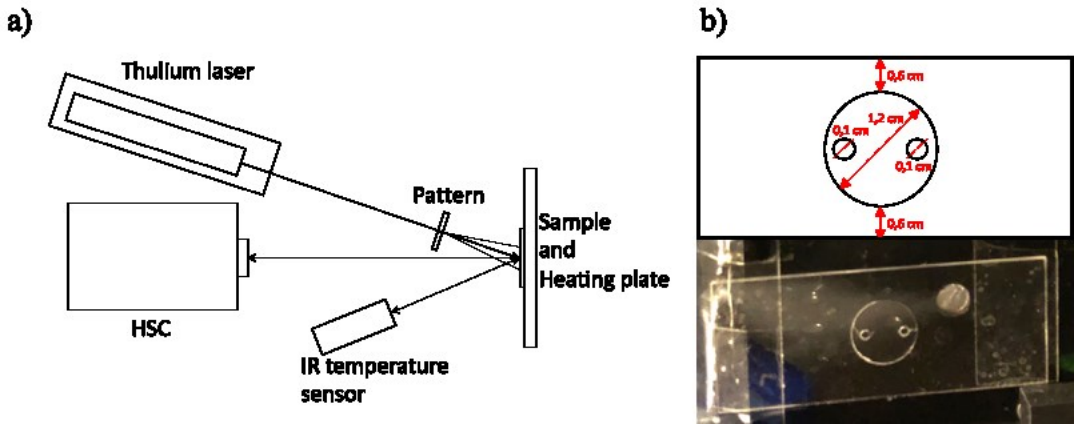

Figure 87. Scheme of the Thulium laser setup to induce the temperature jump in polymer solution. Changes in optical

Another laser setup (Figure 87) to induce the fast T-jump across LCST (in sub-millisecond range) in polymer solution was constructed by dr. Stephan Hauschild from Forschungszentrum Jülich. To induce a T-jump at this setup (Figure 87a), a thulium laser was used ($P_{max} = 50\,W$, $\lambda = 2\,\mu m$, spot size= 5 mm) and the evaluation in time of micelles aggregation was followed by Phantom V1616 high-speed camera (HSC, Vision Research, Ametek Inc.) for a few seconds with 1000/2000 fps. The pictures were collected and managed by Panthon CineView software and analyzed by ImageJ software. Laser time exposure was controlled by software. The temperature of cuvette (Figure 87b) was placed on the heating plate, where we control the temperature of solution. At illuminated spot in solution, the temperature increases above the transition temperature (ΔT = 1.5 °C – 8 °C).

List of tables

TABLE 1. THE MOLECULAR WEIGHT OF POLYMERS. 33
TABLE 2. FIT RESULTS FROM HAWLEY'S EQUATION (EQ.3). 59
TABLE 3. VALUES OF APPARENT ACTIVATION ENERGY FOR CLUSTERS FORMATION AND AGGREGATION OBTAINED FROM ARRHENIUS FUNCTION. 85
TABLE 4. CONDITIONS OF LASER PULSE AND SAMPLE THICKNESS FOR FIGURE 52. 87
TABLE 5. EVOLUTION OF SPOT SIZE MADE BY LASER PULSE ON PS-B-PNIPAM-BA SOLUTION AT TIME FUNCTION DEPENDS ON ENERGY OF LASER PULSE, THICKNESS OF THE SAMPLE AND FOCUSING OF BEAM BY LENS. POLYMER SOLUTION WAS KEPT AT THE INITIAL TEMPERATURE OF $T^* = 30.0$ °C. 89
TABLE 6. MOLECULAR WEIGHT AND POLYDISPERSITY OF LINEAR BLOCK COPOLYMERS. 104

List of figures

FIGURE 1. SCHEMATIC ILLUSTRATION OF THE LITERATURE RESULTS FOR THE CHARACTERISTIC TIME SCALES OF TEMPERATURE-INDUCED COIL COLLAPSE AND AGGREGATION PROCESSES FOR PNIPAM-HOMOPOLYMERS, -MICELLES, AND -MICROGELS. DIFFERENT EXPERIMENTAL METHODS WERE USED, WHERE DIFFERENT RELAXATIONS WERE DISTINGUISHED, WHICH CAN BE ATTRIBUTED TO DIFFERENT COIL COLLAPSE PROCESSES. 2

FIGURE 2. PHASE DIAGRAM FOR A BINARY POLYMER-SOLVENT MIXTURE INCLUDING LCST AND UCST BEHAVIOR. 4

FIGURE 3. COIL-TO-GLOBULE TRANSITION IN POLYMERS WITH LCST BEHAVIOR. 5

FIGURE 4. A) SCHEME OF A MAGNETIC HYSTERESIS LOOP WITH MAGNETIZATION, M, AND APPLIED MAGNETIC FIELD STRENGTH, H, FOR A TYPICAL FERROMAGNETIC MATERIAL. H_C IS COERCIVE MAGNETIC FIELD STRENGTHS, M_R IS THE REMANENT MAGNETIZATION, AND ΔH IS THE WIDTH OF HYSTERESIS WINDOW. (B) SCHEME OF A THERMAL HYSTERESIS LOOP WITH THE OPTICAL TRANSMISSION, RT, AND TEMPERATURE, T, FOR A THERMO-RESPONSIVE POLYMER. T_C REPRESENTS COERCIVITY TEMPERATURES, TR_R IS THE REMANENT OPTICAL TRANSMISSION, AND ΔT IS THE WIDTH OF THERMAL HYSTERESIS WINDOW.[62] 7

FIGURE 5. SCHEME OF POLYMER CHAIN ARRANGEMENT IN SOLVENT AT DIFFERENT CONCENTRATIONS: IN DILUTE SOLUTION (LEFT), IN OVERLAP CONCENTRATION (CENTER) AND IN SEMI-DILUTE CONCENTRATION (RIGHT). 8

FIGURE 6. PNIPAM STRUCTURE. 12

FIGURE 7. SCHEME OF AB BLOCK COPOLYMER MICELLES DEPENDS ON THE LENGTH OF INDIVIDUAL BLOCKS IN POLYMER CHAIN. 14

FIGURE 8. SCHEME OF THE SMALL ANGLE SCATTERING EXPERIMENT. 15

FIGURE 9.A) SIMULATED SAS PROFILE AND B) GUINIER PLOT FOR PARTICLE WITH $R_G = 50$ *A* AND POROD EXPONENT D = 4. 19

FIGURE 10. SIMULATED FORM FACTOR FOR A SPHERICAL PARTICLE WITH RADIUS R = 60 *A*. 20

FIGURE 11. ON THE LEFT SIDE, THE SIMULATED SAS CURVE OF CORE-SHELL SPHERE WITH RADIUS OF THE CORE $R_{CORE} = 60$ *A* AND SHELL THICKNESS $R_{SHELL} = 150$ *A*. ON THE RIGHT SIDE IS A MODEL OF CORE-SHELL MICELLE WITH MARKED FORM FACTOR PARAMETERS. ON THE RIGHT SIDE, THE SCHEME OF CORE-SHELL MICELLE IS PRESENTED WITH MARKED SIZE OF THE MICELLE, CORE, AND SHELL, AS WELL AS SLDS OF EVERY COMPONENT. .21

FIGURE 12. SIMULATED STRUCTURE FACTOR FOR SYSTEM WITH R_{HS} = 60$\AA$ AND THREE DIFFERENT VOLUME FRACTIONS ϕ= 0.01 (BLUE LINE), ϕ= 0.2 (RED LINE) AND ϕ= 0.4 (GREEN LINE). 24

FIGURE 13. SIMULATED SCATTERING CURVE FOR HOMOGENOUS SPHERE AND R = 60$\AA$ WITH DIFFERENT STANDARD DEVIATION OF THE SIZE: σ = 0.0 (GREEN LINE), σ = 0.05 (RED LINE) AND σ = 0.3 (BLUE LINE)....26

FIGURE 14. SIMULATED SCATTERING INTENSITY PLOTTED AS A KRATKY PLOT, $I(Q)Q^2$ VS. Q, FOR SWOLLEN POLYMER (BLUE LINE), GAUSSIAN POLYMER CHAIN (PURPLE LINE) AND DENSE POLYMER STRUCTURE (RED LINE). 27

FIGURE 15. SIMULATED SCATTERING INTENSITY PLOTTED AS THE KRATKY PLOT FOR HOMOGENOUS SPHERE (RED LINE) AND CORE-SHELL SPHERE (BLUE LINE). 27

FIGURE 16. SCHEMATIC DIAGRAM OF TRANSMISSION ELECTRON MICROSCOPE. THE ELECTRONS' BEAM PATH FROM ELECTRON SOURCE (ELECTRON GUN) THROUGH SAMPLE TO SCREEN (CCD CAMERA OR FLUORESCENT SCREEN), WHERE MAGNIFIED IMAGE CAN BE SEEN. 28

FIGURE 17. SCHEME OF PNIPAM SYNTHESIS BY RAFT POLYMERIZATION WITH A) 2-CYANO-2-PROPYL DODECYL TRITHOCARBONATE (CPDT) OR B) 2-(DODECYLTHIOCARBONOTHOYLTHIO)-2-METHYLPROPIONIC ACID (DDMAT). 31

FIGURE 18. SCHEME OF BLOCK COPOLYMER PS-B-PNIPAM-C_{12} SYNTHESIS IN TWO STEPS BY RAFT POLYMERIZATION....32

FIGURE 19. SCHEME OF SUBSTITUTION REACTIONS IN POLYMER END GROUP BY AMYLOLYSIS AND MICHAEL ADDITION REACTION. 33

FIGURE 20. OPTICAL TRANSMISSION CHANGES AS A FUNCTION OF TEMPERATURE FOR LINEAR PNIPAM POLYMERS WITH MOLECULAR WEIGHT (GREEN) 8.2 KG/MOL, (BLUE) 36,0 KG/MOL AND (VIOLET) 96.7 KG/MOL FOR HEATING AND COOLING PROCESS. 34

FIGURE 21. OPTICAL TRANSMISSION CHANGES AS A FUNCTION OF TEMPERATURE FOR LINEAR PNIPAM COPOLYMERS (RED) PS-B-PNIPAM AND (BLUE) PS-B-PNIPAM-BA FOR HEATING AND COOLING PROCESS. 35

FIGURE 22. CHANGES OF HYDRODYNAMIC RADII AS A FUNCTION OF TEMPERATURE FOR LINEAR PNIPAM POLYMERS WITH MOLECULAR WEIGHT (PURPLE) 96.7 KG/MOL AND (BLUE) 36.0 KG/MOL. 36

FIGURE 23. A) CHANGES OF HYDRODYNAMIC RADII AS A FUNCTION OF TEMPERATURE FOR LINEAR COPOLYMER PS-B-PNIPAM-BA FOR TEMPERATURE RANGE (BLUE) 25.0 °C – 34.0 °C AND (ORANGE) 25.0 °C – 31.0 °C. B) CHANGES OF HYDRODYNAMIC RADII IN TIME FOR LINEAR COPOLYMER PS-B-PNIPAM-BA KEPT AT 30.9 °C (DARK RED POINTS) AND 30.4 °C (GREEN POINTS). 37

FIGURE 24. CHANGES OF HYDRODYNAMIC RADII AS A FUNCTION OF TEMPERATURE FOR LINEAR COPOLYMER PS-B-PNIPAM-C_{12}. 38

FIGURE 25. CRYO-TEM IMAGES OF PS-B-PNIPAM-BA SOLUTION AT ONE PHASE REGION (A), TWO-PHASE REGION (B) AND AT THE HYSTERESIS RANGE (C). 39
FIGURE 26. CRYO-TEM IMAGES OF PS-B-PNIPAM-C_{12} SOLUTION AT ONE-PHASE REGION (LEFT) AND AT THE TWO-PHASE REGION (RIGHT). 39
FIGURE 27. CRYO-TEM IMAGES OF LINEAR PNIPAM HOMOPOLYMER SOLUTION (PNIPAM-97) AT 37.0 °C (ABOVE LCST).....40
FIGURE 28. OPTICAL TRANSMISSION MEASUREMENT TO SHOW THE REMANENCE OF THE ONE-PHASE STATE (BLUE) AND THE TWO-PHASE STATE (RED) AT THE TEMPERATURE IN THE HYSTERESIS LOOP, T = 32 °C FOR LINEAR PNIPAM-97 (A) AND T = 30 °C THE PS-B-PNIPAM-BA BLOCK COPOLYMERS (B). 42
FIGURE 29. MICELLAR SIZE DEPENDENCE ON TEMPERATURE MONITORED BY DYNAMIC LIGHT SCATTERING AND CRYO-TEM IMAGING. THE MEASUREMENTS WERE DONE ACROSS LCST WITH SMALL STEPS OF TEMPERATURE CHANGING IN THE HYSTERESIS RANGE. .44
FIGURE 30. A) SCHEME OF THE THIN LAYER BACKSCATTERING DEVICE (TLBS-DEVICE) USED FOR THERMALLY WRITE AND READ INFORMATION BY LASER OR A METAL TIP. PELTIER ELEMENT KEPT THE POLYMER SOLUTION AT T*. IN THE INITIALLY BRIGHT AND DARK STATES (B, C) OF SOLUTIONS OF THE LINEAR PNIPAM-97 HOMOPOLYMER (LEFT IMAGES) AND THE PS-B-PNIPAM-BA BLOCK COPOLYMER (RIGHT IMAGES) DARK ARROWS IN A WHITE MATRIX ARE WRITTEN USING A COLD METAL TIP, AND WHITE ARROWS ARE WRITTEN INTO A DARK MATRIX USING A HOT METAL TIP (C, D).....45
FIGURE 31. WRITING EXPERIMENT WITH LONG TIME OBSERVATION FOR LINEAR-PNIPAM-97 POLYMER. OBSERVATION WAS PERFORMED FOR 24 H, AT $T^* = 32$ °C. SOLUTION HALF TURBID-HALF TRANSPARENT WERE KEPT 5 DAYS ON THE PELTIER ELEMENT TO CHECK STABILITY OF BOTH STAGES FOR LONGER TIME. 47
FIGURE 32. WRITING EXPERIMENT WITH LONG TIME OBSERVATION FOR PS-B-PNIPAM-BA COPOLYMER. OBSERVATION WAS PERFORMED FOR 72 H AT $T^* = 30.0$ °C.....47
FIGURE 33. TEMPORAL EVOLUTION OF A HEXAGONAL SPOT PATTERN WRITTEN INTO THE BACKSCATTERING DISPLAY USING A 5 MS PULSE (250 MJ) OF AN NIR-LASER AT TIMES OF 0, 75, 100, 300, AND 1000 MS AFTER THE PULSE FOR THE A) LINEAR PNIPAM-97 HOMOPOLYMER SOLUTION AND THE B) PS-B-PNIPAM-BA BLOCK COPOLYMER SOLUTION. INDIVIDUAL SPOTS HAVE AN INITIAL DIAMETER OF 1 MM. BY REDUCTION OF THE PULSE DURATION (0.5 MS) AND THE PULSE ENERGY (7.5 MJ) THE DISPLAY SPOT SIZE CAN BE CONFINED TO THE 1 MM LASER SPOT SIZE (C) FOR PNIPAM-97 SOLUTION.....48
FIGURE 34. UNUSUAL INVISIBLE REMANENCE OF THE ENCODED INFORMATION 'HI!'. THE INFORMATION IS WRITTEN ON PNIPAM-97 SOLUTION AT $T^* = 32.0$ °C (A) AND BECOMES INVISIBLE WHEN HEATING TO T = 40 °C, ABOVE THE COERCIVE TEMPERATURE (B). SURPRISINGLY, THE INFORMATION REAPPEARS AFTER COOLING BACK TO T^* (C – WHEN THE $T>\Delta T^*$, D – AFTER REACHING T^* AND EQUILIBRATE).....50

FIGURE 35. PS-B-PNIPAM-BA SOLUTION AT THE BISTABILITY TEMPERATURE IN TWO-PHASE STATE (A). THE INFORMATION "☺" IS WRITTEN AT $T^* = 30.0$ °C (B) AND BECOMES INVISIBLE WHEN HEATING TO T = 37.0 °C, ABOVE THE COERCIVE TEMPERATURE (B). SURPRISINGLY, THE INFORMATION REAPPEARS AFTER COOLING BACK TO T* (D – WHEN $T = T^*$, E – AFTER REACHING T^* AND EQUILIBRATE). 51

FIGURE 36. AND LOGIC GATE FUNCTIONALITY WITH IMAGES OF THE DEVICE BRIGHTNESS FOR DIFFERENT TEMPERATURE AND PH INPUT STATES (LEFT) AND THE CORRESPONDING TABLE (RIGHT). FOR THE INPUT STATES $T > T_{VPT}$ (1) AND pH < 7 (1) THE DEVICE IS IN ITS BRIGHT STATE (1) WITH A BRIGHT BACK SCATTERING SIGNAL I_{BS} AT THE TEMPERATURE T*, IN OTHER CASES THE DEVICE IS IN DARK STATE (0). 52

FIGURE 37. SAXS CURVE OF PS-B-PNIPAM-BA SOLUTION (BLUE DOTS) WITH CONCENTRATION OF 10 MG/ML AT ROOM TEMPERATURE (T = 25.0 °C) WITH ITS BEST FIT (BLACK LINE). 53

FIGURE 38. A) SANS CURVES OF PS-B-PNIPAM-BA SOLUTION IN D_2O WITH CONCENTRATION OF 5 MG/ML IN THE TEMPERATURE RANGE OF 25.0 °C – 35.0 °C AND B) WITH THEIR BEST FITS (BLACK LINES), CURVES ARE SHIFTED VERTICALLY TO SEPARATE THE CURVES. 54

FIGURE 39. KRATKY PLOT, $I(Q)Q^2$ VS Q OF THE SANS DATA FOR AQUEOUS PS-B-PNIPAM-BA SOLUTION AT TEMPERATURE RANGE 25.0 °C – 35.0 °C ALL COMPILED (A) AND AT B) T = 25.0 °C, C) T = 30.8 °C, D) T = 32.5 °C AND E) T = 35.0 °C. 55

FIGURE 40. RESULTS OBTAINED FROM FIT MODELS OF THE SANS DATA AS A FUNCTION OF TEMPERATURE. THE TEMPERATURE RANGE WAS DIVIDED TO 3 PARTS, BELOW LCST (BLUE BACKGROUND), SLIGHTLY ABOVE LCST (ORANGE BACKGROUND) AND ABOVE LCST (RED BACKGROUND). THE PS-CORE RADIUS WAS FIXED AT FITTING AND R_{CORE}=5.3 NM. 57

FIGURE 41. SCATTERING LENGTH DENSITY DIFFERENCE OF PNIPAM-SHELL AND SOLVENT ON DISTANCE FROM PS-CORE TO THE EDGE OF PNIPAM CORONA AT 25.0 °C (BLUE), 30.8 °C (GREEN) AND 32.5 °C (RED). 58

FIGURE 42. TEMPERATURE-PRESSURE PHASE DIAGRAM OF PS-B-PNIPAM-BA AQUEOUS SOLUTION (C = 5 MG/ML) MEASURED BY TURBIDIMETRY. 59

FIGURE 43. A) SANS CURVES OF PS-B-PNIPAM-BA IN D_2O AT PRESSURE RANGE 100 – 1000 BAR COMPARED WITH CURVE MEASURED AT ATMOSPHERIC PRESSURE FOR TEMPERATURE OF T_1 = 32.5 °C. B) CURVES ARE SHIFTED VERTICALLY WITH THEIR BEST FIT AS A BLACK LINE. 61

FIGURE 44. A) FIT RESULTS OBTAINED FROM SANS DATA FOR PS-B-PNIPAM-BA SOLUTION AS A FUNCTION OF PRESSURE AT T_1 = 32.5 °C. THE BLACK DOTS REPRESENT THE RADIUS OF THE MICELLAR CORE, RED DOTS – MICELLAR SHELL THICKNESS, PURPLE DOTS – RADIUS OF THE CLUSTER AND GREEN DOTS THE HALF-DISTANCE BETWEEN CORRELATED COLLAPSED MICELLES IN THE CLUSTER. B) CHANGES OF A FRACTAL DIMENSION, D_F, AND

DECAY PARAMETER OF SHELL-SLD PROFILE, α, AS A FUNCTION OF PRESSURE AT T_1 =32.5 °C. 62

FIGURE 45. A) SANS CURVES OF PS-B-PNIPAM-BA IN D_2O AT PRESSURE RANGE 100 – 400 BAR COMPARED WITH CURVE MEASURED AT ATMOSPHERIC PRESSURE FOR TEMPERATURE OF T = 33.0 °C. B) CURVES ARE SHIFTED VERTICALLY WITH THEIR BEST FIT AS A BLACK LINE. 62

FIGURE 46.A) FIT RESULTS OBTAINED FROM SANS DATA FOR PS-B-PNIPAM-BA SOLUTION AS A FUNCTION OF PRESSURE AT T_2 = 33.0 °C. THE BLACK DOTS REPRESENT THE RADIUS OF THE MICELLAR CORE, RED DOTS – MICELLAR SHELL THICKNESS, PURPLE DOTS – RADIUS OF THE CLUSTER AND GREEN DOTS THE HALF-DISTANCE BETWEEN CORRELATED COLLAPSED MICELLES IN THE CLUSTER. B) CHANGES OF A FRACTAL DIMENSION, D_F, AND DECAY PARAMETER OF SHELL-SLD PROFILE, α, AS A FUNCTION OF PRESSURE AT T_2 = 33.0 °C. 63

FIGURE 47. SANS CURVES WITH THEIR FITS FOR PRESSURE SCAN AT A) T = 33.2 °C AND D) T = 33.5 °C. FIT RESULTS ARE PRESENTED IN CASE OF RADII CHANGES: THICKNESS OF THE MICELLAR CORONA (R_{SHELL}, RED DOTS), SIZE OF THE CLUSTERS ($R_{CLUSTER}$, PURPLE DOTS), DISTANCE BETWEEN CORRELATED MICELLES IN AGGREGATE (R_{HS}, GREEN DOTS), BLACK SQUARES REPRESENT SIZE OF THE MICELLAR CORE, R_{CORE}, AT B) T_3 AND E) T_4. PARAMETERS OF SWELL DEGREE ARE SHOWN IN C) AND F) FOR BOTH TEMPERATURES AS WELL. 64

FIGURE 48. CHANGE OF THE PNIPAM- SHELL THICKNESS IN PRESSURE AT TEMPERATURE OF T_1 = 32.5 °C (DARK BLUE DOTS), T_2 = 33.0 °C (LIGHT BLUE DOTS), T_3 = 33.2 °C (ORANGE DOTS) AND T_4 = 33.5 °C (RED DOTS). 65

FIGURE 49. SCHEME OF THE PS-B-PNIPAM-BA MICELLES BEHAVIOR AS A FUNCTION OF TEMPERATURE. 66

FIGURE 50. SANS CURVES OF PS-B-PNIPAM SOLUTION IN D_2O WITH CONCENTRATION 1 MG/ML (LIGHTER DOTS) AND 5 MG/ML (DARKER DOTS) MEASURED AT TEMPERATURES T_I = 25.0 °C (BLUE) AND T_F = 35.0 °C (RED). CURVES REPRESENT MEASUREMENT AT HIGH TEMPERATURE ARE VERTICALLY SHIFTED BY A FACTOR OF 1000. 67

FIGURE 51. A) 3D-GRAPH OF SANS CURVES AFTER T-JUMP FOR PS-B-PNIPAM-BA SOLUTION WITH FINAL CONCENTRATION OF 1 MG/ML AND SANS CURVE MEASURED AT INITIAL TEMPERATURE OF THE POLYMER SOLUTION (RED DOTS); B) REPRESENTATIVE CURVES FROM KINETICS MEASUREMENT, DIRECTLY AFTER INJECTION SOLUTION TO THE CUVETTE (T = 0.32 S, BLUE DOTS), AFTER CLUSTER FORMATION (T = 4.14 S, LIGHT BLUE DOTS) AND AT THE END OF MEASUREMENT (T = 888.9 S, RED DOTS), COMPARED WITH STATIC RESULTS AT T_I = 25.0 °C (BLUE TRIANGLES) AND T_F = 35.0 °C (RED TRIANGLES), CURVES ARE VERTICALLY SHIFTED TO EACH OTHER. 68

FIGURE 52. FIT RESULTS OBTAINED FROM SANS DATA FOR PS-B-PNIPAM-BA SOLUTION AS A FUNCTION OF TIME. THE MODEL PARAMETERS ARE PRESENTED TO DESCRIBE THE

EVOLUTION OF PARTICLES SIZE BY PNIPAM SHELL THICKNESS (R_{SHELL}, RED DOTS), THE CLUSTER SIZE ($R_{CLUSTER}$, PURPLE DOTS), DISTANCE BETWEEN 5MICELLES IN LARGE DOMAINS (R_{HS}, GREEN DOTS), AND PNIPAM SWELL DEGREE BY SLD-CONTRAST PROFILE (α, ORANGE DOTS) AND MASS FRACTAL DIMENSION (D_F, BLUE DOTS) PARAMETERS.....69

FIGURE 53. A) 3D-GRAPH OF SANS CURVES FOR PS-B-PNIPAM-BA SOLUTION WITH FINAL CONCENTRATION OF 5 MG/ML REPRESENTATIVE CURVES FROM KINETICS MEASUREMENT, DIRECTLY AFTER INJECTION SOLUTION TO THE CUVETTE (T = 0.32 S, BLUE DOTS), AFTER CLUSTER FORMATION (T = 8.01 S, YELLOW DOTS) AND AT THE END OF MEASUREMENT (T = 888.9 S, RED DOTS), COMPARED WITH STATIC RESULTS AT T_I = 25.0 °C (DARK BLUE TRIANGLES) AND T_F = 35.0 °C (DARK RED TRIANGLES), CURVES ARE VERTICALLY SHIFTED TO EACH OTHER. 70

FIGURE 54. FIT RESULTS OBTAINED FROM SANS DATA FOR PS-B-PNIPAM-BA SOLUTION AS A FUNCTION OF TIME. THE MODEL PARAMETERS PRESENT THE COLLAPSING OF THE PNIPAM-SHELL (R_{SHELL}, RED DOTS), CLUSTER GROWTH ($R_{CLUSTER}$, PURPLE DOTS) THE EVOLUTION OF DISTANCE BETWEEN MICELLES IN LARGE DOMAINS (R_{HS}, GREEN DOTS), SIZE OF THE COLLAPSED MICELLES (R_S, DARK RED DOTS), MASS FRACTAL DIMENSION (D_F, BLUE DOTS), SURFACE FRACTAL DIMENSION (D, LIGHT GREEN DOTS) AND DECAY PARAMETER OF SLD CONTRAST BETWEEN SHELL AND SOLVENT (α, ORANGE DOTS). .71

FIGURE 55. THE AGGREGATION KINETICS OF CLUSTERS IN PS-B-PNIPAM-BA SOLUTION WITH CONCENTRATION A) c_1 = 1 MG/ML AND B) c_2 = 5 MG/ML. IN THE CASE OF THE LOWER CONCENTRATION, ONLY DLCA KINETICS WAS OBSERVED, HOWEVER, FOR HIGHER CONCENTRATION 72

FIGURE 56. PROFILE OF TEMPERATURE JUMP INDUCED BY RAMAN LASER (RED LINE), BY THULIUM LASER (BLUE LINE) AND BY RAMAN-THULIUM LASERS SIMULTANEOUSLY (MAGENTA LINE). THE PROFILE WAS DONE FOR TRANSIENT ADSORPTION OF PHENOL RED AT λ = 560 NM, WHERE POINTS ARE MEASUREMENT AND LINES ARE FIT.[161] 73

FIGURE 57. THE SCHEME OF MICELLES BEHAVIOR AFTER T-JUMP ABOVE PHASE TRANSITION TEMPERATURE INDUCED BY RAMAN LASER PULSE. 74

FIGURE 58. THE SCHEME OF MICELLES BEHAVIOR AFTER T-JUMP ABOVE PHASE TRANSITION TEMPERATURE INDUCED BY RAMAN-THULIUM LASER PULSES. 75

FIGURE 59. SCHEME OF T-JUMP ACROSS LCST FOR DIFFERENT $T_{INITIAL}$. DUE TO THE ΔT IS CONSTANT FOR EVERY JUMP, THE SHALLOW OR DEEP TEMPERATURE JUMP ABOVE TRANSITION POINT CAN BE PERFORMED. 76

FIGURE 60. A) REPRESENTATIVE CURVES IN TIME FUNCTION OF THE OPTICAL DENSITY CHANGES FOR PS-B- PNIPAM-BA AFTER T-JUMP (ΔT = +8 °C) INDUCED BY RAMAN LASER PULSE (BLACK LINE) AND B) CHARACTERISTIC RELAXATION TIMES OF CLUSTER FORMING AND SWELLING IN AQUEOUS PS-B-PNIPAM-BA SOLUTION FOR DIFFERENT INITIAL TEMPERATURES. 78

List of figures

FIGURE 61. A) REPRESENTATIVE CURVES OF TIME DEPENDENCE OF THE OPTICAL DENSITY CHANGES FOR LINEAR PNIPAM-36 AFTER T-JUMP (ΔT= +8 °C) INDUCED BY RAMAN LASER PULSE (BLACK LINE) AND B) CHARACTERISTIC TIMES OF CLUSTER FORMATION AND SWELLING AT DIFFERENT INITIAL TEMPERATURES. 78

FIGURE 62. A) REPRESENTATIVE CURVES OF TIME DEPENDENCE OF THE OPTICAL DENSITY CHANGES FOR LINEAR PNIPAM AFTER T-JUMP (ΔT= +8 °C) INDUCED BY RAMAN LASER PULSE (BLACK LINE) AND B) CHARACTERISTIC TIMES OF PROCESSES OF AQUEOUS PS-PNIPAM-C_{12} SOLUTION FOR DIFFERENT INITIAL TEMPERATURE. 79

FIGURE 63. A) REPRESENTATIVE CURVES OF THE OPTICAL DENSITY CHANGES AFTER TEMPERATURE JUMP (ΔT = +10 °C) INDUCED BY RAMAN AND THULIUM LASER PULSES WITH THEIR FITS (BLACK LINE) AND B) CHARACTERISTIC TIMES OF PROCESSES OF AQUEOUS PS-B-PNIPAM-BA SOLUTION FOR DIFFERENT INITIAL TEMPERATURES WHEN SOLUTION WAS KEPT IN HIGHER TEMPERATURE ~9S). 80

FIGURE 64. A) REPRESENTATIVE CURVES OF THE OPTICAL DENSITY CHANGES AFTER TEMPERATURE JUMP (ΔT = +10 °C) INDUCED BY RAMAN AND THULIUM LASER PULSES (BLACK LINE) AND B) CHARACTERISTIC TIMES OF PROCESSES OF AQUEOUS LINEAR PNIPAM SOLUTION FOR DIFFERENT INITIAL TEMPERATURES WHEN SOLUTION WAS KEPT IN T_{MAX} ~10S. 81

FIGURE 65. A) REPRESENTATIVE CURVES OF THE OPTICAL DENSITY CHANGES AFTER TEMPERATURE JUMP (ΔT = +10 °C) INDUCED BY RAMAN AND THULIUM LASER PULSES WITH THEIR BEST FITS (BLACK LINE) AND B) CHARACTERISTIC TIMES OF PROCESSES OF AQUEOUS PS-B-PNIPAM-C_{12} SOLUTION FOR DIFFERENT INITIAL TEMPERATURES WHEN SOLUTION WAS KEPT IN HIGHER TEMPERATURE ~9 S. 82

FIGURE 66. SCHEME OF MULTISTEP KINETICS MECHANISM ACROSS TRANSITION TEMPERATURE IN RAMAN-THULIUM LASER EXPERIMENT. 83

FIGURE 67. TRANSITION TIME FOR POLYMERS EXAMINED IN A) RL AND B) RTL EXPERIMENTS AS A FUNCTION OF TEMPERATURE JUMP DEPTH ABOVE LCST. 84

FIGURE 68. ARRHENIUS PLOT OF CLUSTER FORMATION FOR A) PS-B-PNIPAM-BA, B) PNIPAM-36 AND C) PS-B-PNIPAM-C_{12} TO DETERMINE THE ACTIVATION ENERGY OF THE PROCESS. 85

FIGURE 69. SNAPSHOTS OF PHASE-TRANSITION EVOLUTION IN TIME AFTER LASER PULSE FOR PS-B-PNIPAM-BA SOLUTION WITH PULSE ENERGY OF $E_{LASER\ PULSE}$ = 500 MJ, ILLUMINATION TIME OF $T_{LASER\ PULSE}$ = 10 MS, SAMPLE THICKNESS OF 0.6 MM AND LASER BEAM DIAMETER OF 5 MM. 86

FIGURE 70. DIFFERENCE OF SPOT SIZE WRITTEN ON THE PS-B-PNIPAM-BA SOLUTION BY NIR-LASER AT 100 MS AFTER LASER-PULSE DEPENDING ON THE TIME AND ENERGY OF THE LASER-PULSE. 87

FIGURE 71. SNAPSHOTS OF PHASE-TRANSITION EVOLUTION IN TIME AFTER LASER PULSE, WITH BEAM DIAMETER OF 5 MM, FOR PS-B-PNIPAM-BA SOLUTION WITH

ILLUMINATION TIME OF $T_{LASER\ PULSE}$ = 0.5 MS, SAMPLE THICKNESS OF 0.2 MM AND PULSE ENERGY OF $E_{LASER\ PULSE}$ = 25 MJ (UP) AND $E_{LASER\ PULSE}$ = 10 MJ (BOTTOM). 88

FIGURE 72. CURVES OBTAINED FROM EXPERIMENT WHERE T-JUMP WAS INDUCED BY THULIUM LASER WITH FIXED ILLUMINATION TIME, $T_{LASER\ PULSE}$ = 0.5 MS, AND DIFFERENT LASER PULSE ENERGY, A) 25 MJ, B) 12.5 MJ, C) 10 MJ, D) 7.5 MJ AND E) 5 MJ. THEY WERE FITTED BY KWW STRETCHED AND COMPRESSED EXPONENTIAL FUNCTION AND OBTAINED RESULTS OF CHARACTERISTIC TIMES ARE PRESENTED IN F). INITIAL TEMPERATURE OF THE POLYMER SOLUTION WAS FIXED, T^* = 30.0 °C, FOR EVERY MEASUREMENT. 91

FIGURE 73. EXPERIMENTAL CURVES FOR LINEAR PNIPAM-97 OBTAINED FROM T-JUMP INDUCED BY THULIUM LASER WITH PULSE TIME OF $T_{LASER\ PULSE}$ = 0.5 MS AND ENERGY $E_{LASER\ PULSE}$ = 7.5 MJ BUT WITH DIFFERENT INITIAL TEMPERATURE, $T_{INITIAL}$ = 30.0 °C LIGHT GREEN, AND $T_{INITIAL}$ = 32.0 °C GREEN. CHANGES OF THE MEAN GRAY VALUE (MGV) WERE TRACED BY A) HSC AND B) WEBCAM TO RECORD CHANGES AT LONGER TIME. 92

FIGURE 74. SCHEME OF PHASE TRANSITION ACROSS LCST FOR LINEAR PNIPAM POLYMER. 95

FIGURE 75. STRUCTURE OF TRITHOCARBONATE RAFT AGENT. 100

FIGURE 76. ^{1}H NMR SPECTRUM OF POLYSTYRENE (PS) POLYMER IN $CDCL_3$. 101

FIGURE 77. ^{1}H NMR SPECTRUM OF PS-B-PNIPAM-C_{12} POLYMER IN $CDCL_3$. 102

FIGURE 78. ^{1}H NMR SPECTRUM OF PS-B-PNIPAM-BA POLYMER AFTER SUBSTITUTION WITH N-BUTYL ACRYLATE AS AN END GROUP IN $CDCL_3$. 103

FIGURE 79. SEC TRACE OF BLOCK COPOLYMER PS-B-PNIPAM-BA. 103

FIGURE 80. ^{1}H NMR SPECTRUM OF PNIPAM POLYMER IN $CDCL_3$. 105

FIGURE 81. SEC TRACE OF LINEAR PNIPAM POLYMER WITH DIFFERENT MOLECULAR WEIGHT, RED – M_W = 97.6 KG/MOL, GREEN – M_W =36.8 KG/MOL AND BLUE – M_W = 8.2 KG/MOL. 105

FIGURE 82. EXPERIMENTAL SETUP FOR DYNAMIC LIGHT SCATTERING. 108

FIGURE 83. SANS INSTRUMENT SCHEME OF KWS-1[176] IN MLZ GARCHING. 110

FIGURE 84. SCHEME OF STOPPED-FLOW DEVICE USED FOR TEMPERATURE JUMP EXPERIMENT ON SANS. 111

FIGURE 85. SANS INSTRUMENT SCHEME OF D11[179] IN ILL GRENOBLE. 111

FIGURE 86. OPTICAL LAYOUT OF THE NIR-LASER JUMP EXPERIMENT CONSISTING OF A ND:YAG/H_2-RAMAN CONVERTER LASER TO INDUCE 10 NS TEMPERATURE JUMPS OF UP TO 10 °C AND A TH-FIBER LASER TO KEEP THE PLATEAU TEMPERATURE FOR UP TO SEVERAL MINUTES. 112

FIGURE 87. SCHEME OF THE THULIUM LASER SETUP TO INDUCE THE TEMPERATURE JUMP IN POLYMER SOLUTION. CHANGES IN OPTICAL 113

Bibliography:

1. SCHMALJOHANN, D. Thermo- and pH-responsive polymers in drug delivery☆. *Adv. Drug Deliv. Rev.* **58**, 1655–1670 (2006).
2. Hogan, K. J. & Mikos, A. G. Biodegradable thermoresponsive polymers: Applications in drug delivery and tissue engineering. *Polymer (Guildf).* (2020) doi:10.1016/j.polymer.2020.123063.
3. Liu, F. & Urban, M. W. Recent advances and challenges in designing stimuli-responsive polymers. *Progress in Polymer Science (Oxford)* (2010) doi:10.1016/j.progpolymsci.2009.10.002.
4. Halperin, A., Kröger, M. & Winnik, F. M. Poly(N -isopropylacrylamide) Phase Diagrams: Fifty Years of Research. *Angew. Chemie Int. Ed.* **54**, 15342–15367 (2015).
5. Doberenz, F., Zeng, K., Willems, C., Zhang, K. & Groth, T. Thermoresponsive polymers and their biomedical application in tissue engineering – a review. *J. Mater. Chem. B* **8**, 607–628 (2020).
6. Heskins, M. & Guillet, J. E. Solution Properties of Poly(N-isopropylacrylamide). *J. Macromol. Sci. Part A - Chem.* (1968) doi:10.1080/10601326808051910.
7. Gan, D. & Lyon, L. A. Tunable Swelling Kinetics in Core−Shell Hydrogel Nanoparticles. *J. Am. Chem. Soc.* **123**, 7511–7517 (2001).
8. Wu, C. A comparison between the `coil-to-globule' transition of linear chains and the "volume phase transition" of spherical microgels1Dedicated to the 80th birthday of Professor Renyuan Qian.1. *Polymer (Guildf).* **39**, 4609–4619 (1998).
9. Eliassaf, J. Aqueous solutions of poly(N-isopropylacrylamide). *J. Appl. Polym. Sci.* **22**, 873–874 (1978).
10. Ye, X. *et al.* How Many Stages in the Coil-to-Globule Transition of Linear Homopolymer Chains in a Dilute Solution? *Macromolecules* **40**, 4750–4752 (2007).
11. Tang, Y. & Liu, X. Collapse kinetics for individual poly(N-isopropylmethacrylamide) chains. *Polymer (Guildf).* **51**, 897–901 (2010).
12. Wu, T.-Y., Zrimsek, A. B., Bykov, S. V., Jakubek, R. S. & Asher, S. A. Hydrophobic Collapse Initiates the Poly(N -isopropylacrylamide) Volume Phase Transition Reaction Coordinate. *J. Phys. Chem. B* **122**, 3008–3014 (2018).
13. Tsuboi, Y., Yoshida, Y., Okada, K. & Kitamura, N. Phase Separation Dynamics of Aqueous Solutions of Thermoresponsive Polymers Studied by a Laser T-Jump Technique. *J. Phys. Chem. B* **112**, 2562–2565 (2008).
14. Inoue, H., Kuwahara, S. & Katayama, K. The whole process of phase transition and relaxation of poly(N-isopropylacrylamide) aqueous solution. *Phys. Chem. Chem. Phys.* **15**, 3814 (2013).
15. Wang, J., Gan, D., Lyon, L. A. & El-Sayed, M. A. Temperature-Jump Investigations of the Kinetics of Hydrogel Nanoparticle Volume Phase Transitions. *J. Am. Chem. Soc.* **123**, 11284–11289 (2001).
16. Ahmed, Z., Gooding, E. A., Pimenov, K. V., Wang, L. & Asher, S. A. UV Resonance Raman Determination of Molecular Mechanism of Poly(N -isopropylacrylamide) Volume Phase Transition. *J. Phys. Chem. B* **113**, 4248–4256 (2009).
17. Reese, C. E., Mikhonin, A. V., Kamenjicki, M., Tikhonov, A. & Asher, S. A. Nanogel Nanosecond Photonic Crystal Optical Switching. *J. Am. Chem. Soc.* **126**, 1493–1496 (2004).

Bibliography:

18. Adelsberger, J. *et al.* Thermoresponsive PS- b -PNIPAM- b -PS Micelles: Aggregation Behavior, Segmental Dynamics, and Thermal Response. *Macromolecules* **43**, 2490–2501 (2010).
19. Adelsberger, J. *et al.* Kinetics of Collapse Transition and Cluster Formation in a Thermoresponsive Micellar Solution of P(S-b-NIPAM-b-S) Induced by a Temperature Jump. *Macromol. Rapid Commun.* **33**, 254–259 (2012).
20. Hirose, H. & Shibayama, M. Kinetics of Volume Phase Transition in Poly(N -isopropylacrylamide- co -acrylic acid) Gels. *Macromolecules* **31**, 5336–5342 (1998).
21. Chu, L.-Y., Kim, J.-W., Shah, R. K. & Weitz, D. A. Monodisperse Thermoresponsive Microgels with Tunable Volume-Phase Transition Kinetics. *Adv. Funct. Mater.* **17**, 3499–3504 (2007).
22. Wei, M., Gao, Y., Li, X. & Serpe, M. J. Stimuli-responsive polymers and their applications. *Polymer Chemistry* (2017) doi:10.1039/c6py01585a.
23. Hoffman, A. S. "intelligent" polymers in medicine and biotechnology. *Macromol. Symp.* (1995) doi:10.1002/masy.19950980156.
24. Theato, P. Synthesis of well-defined polymeric activated esters. *J. Polym. Sci. Part A Polym. Chem.* (2008) doi:10.1002/pola.22994.
25. Doberenz, F., Zeng, K., Willems, C., Zhang, K. & Groth, T. Thermoresponsive polymers and their biomedical application in tissue engineering-A review. *Journal of Materials Chemistry B* (2020) doi:10.1039/c9tb02052g.
26. De La Rosa, V. R., Woisel, P. & Hoogenboom, R. Supramolecular control over thermoresponsive polymers. *Materials Today* (2016) doi:10.1016/j.mattod.2015.06.013.
27. Jochum, F. D. & Theato, P. Temperature- and light-responsive smart polymer materials. *Chem. Soc. Rev.* (2013) doi:10.1039/c2cs35191a.
28. Dai, S., Ravi, P. & Tam, K. C. pH-Responsive polymers: Synthesis, properties and applications. *Soft Matter* (2008) doi:10.1039/b714741d.
29. Bertrand, O. & Gohy, J. F. Photo-responsive polymers: Synthesis and applications. *Polymer Chemistry* (2017) doi:10.1039/c6py01082b.
30. Wang, X., Zhang, S., Xu, Y., Zhao, X. & Guo, X. Ionic Strength-Responsive Binding between Nanoparticles and Proteins. *Langmuir* (2018) doi:10.1021/acs.langmuir.8b00944.
31. Xu, Y. & Hickey, R. J. Solvent-Responsive and Reversible Structural Coloration in Nanostructured Block Polymer Films. *Macromolecules* (2020) doi:10.1021/acs.macromol.0c00639.
32. Scherzinger, C., Schwarz, A., Bardow, A., Leonhard, K. & Richtering, W. Cononsolvency of poly-N-isopropyl acrylamide (PNIPAM): Microgels versus linear chains and macrogels. *Current Opinion in Colloid and Interface Science* (2014) doi:10.1016/j.cocis.2014.03.011.
33. Tanaka, T., Nishio, I., Sun, S. T. & Ueno-Nishio, S. Collapse of gels in an electric field. *Science (80-.).* (1982) doi:10.1126/science.218.4571.467.
34. Seuring, J. & Agarwal, S. Polymers with upper critical solution temperature in aqueous solution: Unexpected properties from known building blocks. *ACS Macro Lett.* (2013) doi:10.1021/mz400227y.
35. Seuring, J., Bayer, F. M., Huber, K. & Agarwal, S. Upper critical solution temperature of poly(N -acryloyl glycinamide) in water: A concealed property. *Macromolecules* (2012) doi:10.1021/ma202059t.
36. Meiswinkel, G. & Ritter, H. A new type of thermoresponsive copolymer with UCST-type transitions in water: Poly(N-vinylimidazole-co-1-vinyl-2-

(hydroxymethyl)imidazole). *Macromol. Rapid Commun.* (2013) doi:10.1002/marc.201300213.

37. Shimada, N. *et al.* Ureido-derivatized polymers based on both poly(allylurea) and poly(l -citrulline) exhibit UCST-type phase transition behavior under physiologically relevant conditions. *Biomacromolecules* (2011) doi:10.1021/bm2010752.
38. Charlet, G. & Delmas, G. Thermodynamic properties of polyolefin solutions at high temperature: 1. Lower critical solubility temperatures of polyethylene, polypropylene and ethylene-propylene copolymers in hydrocarbon solvents. *Polymer (Guildf).* (1981) doi:10.1016/0032-3861(81)90130-0.
39. Schild, H. G. Poly(N-isopropylacrylamide): experiment, theory and application. *Prog. Polym. Sci.* **17**, 163–249 (1992).
40. Song, Z., Wang, K., Gao, C., Wang, S. & Zhang, W. A New Thermo-, pH-, and CO 2 -Responsive Homopolymer of Poly[N -[2-(diethylamino)ethyl]acrylamide]: Is the Diethylamino Group Underestimated? *Macromolecules* **49**, 162–171 (2016).
41. Cao, Y., Zhu, X. X., Luo, J. & Liu, H. Effects of substitution groups on the RAFT polymerization of N-alkylacrylamides in the preparation of thermosensitive block copolymers. *Macromolecules* (2007) doi:10.1021/ma0628230.
42. Lee, M. F. X., Chan, E. S., Tam, K. C. & Tey, B. T. Thermo-responsive adsorbent for size-selective protein adsorption. *J. Chromatogr. A* (2015) doi:10.1016/j.chroma.2015.03.034.
43. Roth, P. J., Jochum, F. D., Forst, F. R., Zentel, R. & Theato, P. Influence of End Groups on the Stimulus-Responsive Behavior of Poly[oligo(ethylene glycol) methacrylate] in Water. *Macromolecules* **43**, 4638–4645 (2010).
44. Bütün, V., Armes, S. P. & Billingham, N. C. Synthesis and aqueous solution properties of near-monodisperse tertiary amine methacrylate homopolymers and diblock copolymers. *Polymer (Guildf).* (2001) doi:10.1016/S0032-3861(01)00066-0.
45. Steinhauer, W., Hoogenboom, R., Keul, H. & Moeller, M. Block and gradient copolymers of 2-hydroxyethyl acrylate and 2-methoxyethyl acrylate via RAFT: Polymerization kinetics, thermoresponsive properties, and micellization. *Macromolecules* (2013) doi:10.1021/ma302606x.
46. De Oliveira, T. E., Mukherji, D., Kremer, K. & Netz, P. A. Effects of stereochemistry and copolymerization on the LCST of PNIPAm. *J. Chem. Phys.* (2017) doi:10.1063/1.4974165.
47. Ebara, M. *et al.* Copolymerization of 2-carboxyisopropylacrylamide with N-isopropylacrylamide accelerates cell detachment from grafted surfaces by reducing temperature. *Biomacromolecules* (2003) doi:10.1021/bm025692t.
48. Jochum, F. D., Borg, L. Zur, Roth, P. J. & Theato, P. Thermo- and light-responsive polymers containing photoswitchable azobenzene end groups. *Macromolecules* (2009) doi:10.1021/ma901295f.
49. Hoogenboom, R. *et al.* Tuning the LCST of poly(2-oxazoline)s by varying composition and molecular weight: Alternatives to poly(N-isopropylacrylamide)? *Chem. Commun.* (2008) doi:10.1039/b813140f.
50. Zhang, Y., Furyk, S., Bergbreiter, D. E. & Cremer, P. S. Specific Ion Effects on the Water Solubility of Macromolecules: PNIPAM and the Hofmeister Series. *J. Am. Chem. Soc.* **127**, 14505–14510 (2005).
51. Meeussen, F. *et al.* Phase behaviour of poly(N -vinyl caprolactam) in water. *Polymer (Guildf).* **41**, 8597–8602 (2000).
52. Van Durme, K., Van Assche, G. & Van Mele, B. Kinetics of Demixing and

Remixing in Poly(N -isopropylacrylamide)/Water Studied by Modulated Temperature DSC. *Macromolecules* **37**, 9596–9605 (2004).
53. Zheng, Q. & Pan, C. Preparation and characterization of dendrimer-star PNIPAAM using dithiobenzoate-terminated PPI dendrimer via RAFT polymerization. *Eur. Polym. J.* **42**, 807–814 (2006).
54. Jain, K., Vedarajan, R., Watanabe, M., Ishikiriyama, M. & Matsumi, N. Tunable LCST behavior of poly(N-isopropylacrylamide/ionic liquid) copolymers. *Polym. Chem.* **6**, 6819–6825 (2015).
55. Plummer, R., Hill, D. J. T. & Whittaker, A. K. Solution Properties of Star and Linear Poly(N -isopropylacrylamide). *Macromolecules* **39**, 8379–8388 (2006).
56. Luo, S., Xu, J., Zhu, Z., Wu, C. & Liu, S. Phase Transition Behavior of Unimolecular Micelles with Thermoresponsive Poly(N -isopropylacrylamide) Coronas. *J. Phys. Chem. B* **110**, 9132–9139 (2006).
57. Schäfer-Soenen, H. *et al.* Zero and Off-Zero Critical Concentrations in Systems Containing Polydisperse Polymers with Very High Molar Masses. 2. The System Water−Poly(vinyl methyl ether). *Macromolecules* **30**, 410–416 (1997).
58. Swier, S., Van Durme, K. & Van Mele, B. Modulated-temperature differential scanning calorimetry study of temperature-induced mixing and demixing in poly(vinylmethylether)/water. *J. Polym. Sci. Part B Polym. Phys.* **41**, 1824–1836 (2003).
59. Venkataramani, S. *et al.* Magnetic Bistability of Molecules in Homogeneous Solution at Room Temperature. *Science (80-.).* **331**, 445–448 (2011).
60. Ortín, J. & Delaey, L. Hysteresis in shape-memory alloys. *Int. J. Non. Linear. Mech.* **37**, 1275–1281 (2002).
61. Harres, A. *et al.* Criteria for saturated magnetization loop. *J. Magn. Magn. Mater.* **402**, 76–82 (2016).
62. Michalska-Walkowiak, J., Förster, B., Hauschild, S. & Förster, S. Bistability, Remanence, Read/write-memory and Logic Gate Function via A Stimuli Responsive Polymer. *Adv. Mater.* 2108833 (2022) doi:10.1002/adma.202108833.
63. Wu, C. & Wang, X. Globule-to-Coil Transition of a Single Homopolymer Chain in Solution. *Phys. Rev. Lett.* **80**, 4092–4094 (1998).
64. Maeda, Y., Nakamura, T. & Ikeda, I. Changes in the Hydration States of Poly(N -n -propylmethacrylamide) and Poly(N -isopropylmethacrylamide) during Their Phase Transitions in Water Observed by FTIR Spectroscopy. *Macromolecules* **34**, 8246–8251 (2001).
65. Cheng, H., Shen, L. & Wu, C. LLS and FTIR Studies on the Hysteresis in Association and Dissociation of Poly(N- isopropylacrylamide) Chains in Water. *Macromolecules* **39**, 2325–2329 (2006).
66. Hamamura, K., Watanabe, K., Sanada, Y., Tanaka, F. & Katsumoto, Y. Relationship between the phase diagram and hysteresis in demixing and remixing for atactic and meso-rich Poly(N-isopropylacrylamide)s in water. *Polymer (Guildf).* **161**, 92–100 (2019).
67. Lu, Y., Zhou, K., Ding, Y., Zhang, G. & Wu, C. Origin of hysteresis observed in association and dissociation of polymer chains in water. *Phys. Chem. Chem. Phys.* (2010) doi:10.1039/b918969f.
68. Hamley, I. W. *Introduction to Soft Matter– Revised Edition*. *Introduction to Soft Matter: Synthetic and Biological Self-Assembling Materials* (John Wiley & Sons, Ltd, 2007). doi:10.1002/9780470517338.
69. Fetters, L. J., Hadjichristidis, N., Lindner, J. S. & Mays, J. W. Molecular Weight Dependence of Hydrodynamic and Thermodynamic Properties for Well-Defined

Linear Polymers in Solution. *J. Phys. Chem. Ref. Data* **23**, 619–640 (1994).
70. Ying, Q. & Chu, B. Overlap concentration of macromolecules in solution. *Macromolecules* **20**, 362–366 (1987).
71. Verwey, E. J. W. Theory of the Stability of Lyophobic Colloids. *J. Phys. Colloid Chem.* **51**, 631–636 (1947).
72. Lin, M. Y. *et al.* Universal diffusion-limited colloid aggregation. *J. Phys. Condens. Matter* **2**, 3093–3113 (1990).
73. von Smoluchowski, M. Theorie der Brownschen Molekular bewegungund der Suspensionen. *Ann. Phys* 21:756-780 (1916).
74. Galina, H; Lechowicz, B. Mean-Field Kinetic Modeling of Polymerization: The Smoluchowski Coagulation Equation. in *Advances in Polymer Science* (eds. Dugek, C. K. et al.) 135–172 (1998).
75. Vyazovkin, S. Activation Energies and Temperature Dependencies of the Rates of Crystallization and Melting of Polymers. *Polymers (Basel).* **12**, 1070 (2020).
76. Tauer, K., Gau, D., Schulze, S. & Hernandez, H. Transient-thermal and isothermal studies of thermo-sensitive polymer solution with ultrasound resonator technology. *Polymer (Guildf).* **49**, 5452–5457 (2008).
77. Mao, Z. & Campbell, C. T. Apparent Activation Energies in Complex Reaction Mechanisms: A Simple Relationship via Degrees of Rate Control. *ACS Catal.* **9**, 9465–9473 (2019).
78. Burnham, A. K., Weese, R. K. & Weeks, B. L. A Distributed Activation Energy Model of Thermodynamically Inhibited Nucleation and Growth Reactions and Its Application to the β−δ Phase Transition of HMX. *J. Phys. Chem. B* **108**, 19432–19441 (2004).
79. Pham, Q.-T., Yao, Z.-H., Chang, Y.-T., Wang, F.-M. & Chern, C.-S. LCST phase transition kinetics of aqueous poly(N-isopropylacrylamide) solution. *J. Taiwan Inst. Chem. Eng.* **93**, 63–69 (2018).
80. Liu, W. & Li, G. Non-isothermal kinetic analysis of the thermal denaturation of type I collagen in solution using isoconversional and multivariate non-linear regression methods. *Polym. Degrad. Stab.* **95**, 2233–2240 (2010).
81. Halperin, A., Kröger, M. & Winnik, F. M. Poly(N -isopropylacrylamide) Phase Diagrams: Fifty Years of Research. *Angew. Chemie Int. Ed.* **54**, 15342–15367 (2015).
82. Lanzalaco, S. & Armelin, E. Poly(N-isopropylacrylamide) and Copolymers: A Review on Recent Progresses in Biomedical Applications. *Gels* **3**, 36 (2017).
83. Plamper, F. A. & Richtering, W. Functional Microgels and Microgel Systems. *Acc. Chem. Res.* **50**, 131–140 (2017).
84. Costa, R. O. R. & Freitas, R. F. S. Phase behavior of poly(N-isopropylacrylamide) in binary aqueous solutions. *Polymer (Guildf).* **43**, 5879–5885 (2002).
85. Tokarev, I. & Minko, S. Stimuli-responsive hydrogel thin films. *Soft Matter* **5**, 511–524 (2009).
86. Chu, L.-Y., Niitsuma, T., Yamaguchi, T. & Nakao, S. Thermoresponsive transport through porous membranes with grafted PNIPAM gates. *AIChE J.* **49**, 896–909 (2003).
87. Young, R. E. *et al.* Optimizing the alignment of thermoresponsive poly(N-isopropyl acrylamide) electrospun nanofibers for tissue engineering applications: A factorial design of experiments approach. *PLoS One* **14**, e0219254 (2019).
88. Crassous, J. J., Ballauff, M., Drechsler, M., Schmidt, J. & Talmon, Y. Imaging the Volume Transition in Thermosensitive Core−Shell Particles by Cryo-Transmission Electron Microscopy. *Langmuir* **22**, 2403–2406 (2006).

Bibliography:

89. Nagase, K., Kobayashi, J. & Okano, T. Temperature-responsive intelligent interfaces for biomolecular separation and cell sheet engineering. *Journal of the Royal Society Interface* (2009) doi:10.1098/rsif.2008.0499.focus.
90. Hoffman, A. S. & Stayton, P. S. Conjugates of stimuli-responsive polymers and proteins. *Progress in Polymer Science (Oxford)* (2007) doi:10.1016/j.progpolymsci.2007.05.005.
91. Maeda, Y., Nakamura, T. & Ikeda, I. Changes in the Hydration States of Poly(N -alkylacrylamide)s during Their Phase Transitions in Water Observed by FTIR Spectroscopy. *Macromolecules* **34**, 1391–1399 (2001).
92. Pelton, R. Poly(N-isopropylacrylamide) (PNIPAM) is never hydrophobic. *J. Colloid Interface Sci.* **348**, 673–674 (2010).
93. Niebuur, B.-J. *et al.* Kinetics of Mesoglobule Formation and Growth in Aqueous Poly(N -isopropylacrylamide) Solutions: Pressure Jumps at Low and at High Pressure. *Macromolecules* **52**, 6416–6427 (2019).
94. Gao, X. *et al.* pH- and thermo-responsive poly(N-isopropylacrylamide-co-acrylic acid derivative) copolymers and hydrogels with LCST dependent on pH and alkyl side groups. *J. Mater. Chem. B* **1**, 5578 (2013).
95. Winnik, F. M., Ringsdorf, H. & Venzmer, J. Methanol-water as a co-nonsolvent system for poly(N-isopropylacrylamide). *Macromolecules* **23**, 2415–2416 (1990).
96. Kyriakos, K. *et al.* Cononsolvency of Water/Methanol Mixtures for PNIPAM and PS- b -PNIPAM: Pathway of Aggregate Formation Investigated Using Time-Resolved SANS. *Macromolecules* **47**, 6867–6879 (2014).
97. Grigera, J. R. & McCarthy, A. N. The Behavior of the Hydrophobic Effect under Pressure and Protein Denaturation. *Biophys. J.* **98**, 1626–1631 (2010).
98. Rzaev, Z. M. O., Dinçer, S. & Pişkin, E. Functional copolymers of N-isopropylacrylamide for bioengineering applications. *Prog. Polym. Sci.* **32**, 534–595 (2007).
99. Otake, K., Inomata, H., Konno, M. & Saito, S. Thermal Analysis of the Volume Phase Transition with N-Isopropylacrylamide Gels. *Macromolecules* (1990) doi:10.1021/ma00203a049.
100. Chen, G. & Hoffman, A. S. Graft copolymers that exhibit temperature-induced phase transitions over a wide range of pH. *Nature* (1995) doi:10.1038/373049a0.
101. Yoshida, R., Sakai, K., Okano, T. & Sakurai, Y. Modulating the phase transition temperature and thermosensitivity in N-isopropylacrylamide copolymer gels. *J. Biomater. Sci. Polym. Ed.* **6**, 585–598 (1995).
102. Riess, G. Micellization of block copolymers. *Prog. Polym. Sci.* **28**, 1107–1170 (2003).
103. Sant, S. B. Physics and Chemistry of Interfaces. *Mater. Manuf. Process.* **28**, 1379–1380 (2013).
104. Daoud, M. & Cotton, J. P. Star shaped polymers : a model for the conformation and its concentration dependence. *J. Phys.* **43**, 531–538 (1982).
105. Anitas, E. M. & Slyamov, A. M. Small-angle scattering from deterministic mass and surface fractal systems. *Proc. Rom. Acad. Ser. A - Math. Phys. Tech. Sci. Inf. Sci.* **19**, 135–142 (2018).
106. Brückel T. Laboratory Course Neutron Scattering. *Forschungszentrum Jülich GmbH Zentrallbibliothek* **172**, 2.1-2.34 (2018).
107. Svergun, D. I. & Koch, M. H. J. Small-angle scattering studies of biological macromolecules in solution. *Reports Prog. Phys.* **66**, 1735–1782 (2003).
108. Hammouda, B. A new Guinier–Porod model. *J. Appl. Crystallogr.* **43**, 716–719 (2010).

109. Hammouda, B. Analysis of the Beaucage model. *J. Appl. Crystallogr.* **43**, 1474–1478 (2010).
110. Sinha, S. K., Sirota, E. B., Garoff, S. & Stanley, H. B. X-ray and neutron scattering from rough surfaces. *Phys. Rev. B* **38**, 2297–2311 (1988).
111. Guinier, André, Gérard Fournet, and K. L. Y. Small-angle scattering of X-rays. *Prog. Cryst. Growth Charact.* (1955).
112. Vogiatzis, G. G. & Theodorou, D. N. Structure of Polymer Layers Grafted to Nanoparticles in Silica–Polystyrene Nanocomposites. *Macromolecules* **46**, 4670–4683 (2013).
113. Grünewald, T. A. *et al.* Core–Shell Structure of Monodisperse Poly(ethylene glycol)-Grafted Iron Oxide Nanoparticles Studied by Small-Angle X-ray Scattering. *Chem. Mater.* **27**, 4763–4771 (2015).
114. Willner, L. *et al.* Micellization of amphiphilic diblock copolymers: Corona shape and mean-field to scaling crossover. *Europhys. Lett.* **51**, 628–634 (2000).
115. Mhanna, R., Lefort, R., Noirez, L. & Morineau, D. Microstructure and concentration fluctuations in alcohol–Toluene and alcohol-Cyclohexane binary liquids: A small angle neutron scattering study. *J. Mol. Liq.* **218**, 198–207 (2016).
116. Ornstein, L. & Zernike, F. Accidental deviations of density and opalescence at the critical point of a single substance. *Proc. Akad. Sci.(Amsterdam)* **XVII**, 793–806 (1914).
117. Fisher, M. E. Correlation Functions and the Critical Region of Simple Fluids. *J. Math. Phys.* **5**, 944–962 (1964).
118. Tardieu, A. *et al.* Proteins in solution:from X-ray scattering intensities to interaction potentials. *J. Cryst. Growth* **196**, 193–203 (1999).
119. Baxter, R. J. Percus–Yevick Equation for Hard Spheres with Surface Adhesion. *J. Chem. Phys.* **49**, 2770–2774 (1968).
120. Percus, J. K. & Yevick, G. J. Analysis of Classical Statistical Mechanics by Means of Collective Coordinates. *Phys. Rev.* **110**, 1–13 (1958).
121. Wertheim, M. S. Exact Solution of the Percus-Yevick Integral Equation for Hard Spheres. *Phys. Rev. Lett.* **10**, 321–323 (1963).
122. Teixeira, J. Small-angle scattering by fractal systems. *J. Appl. Crystallogr.* **21**, 781–785 (1988).
123. Putnam, C. D., Hammel, M., Hura, G. L. & Tainer, J. A. X-ray solution scattering (SAXS) combined with crystallography and computation: defining accurate macromolecular structures, conformations and assemblies in solution. *Q. Rev. Biophys.* **40**, 191–285 (2007).
124. Receveur-Brechot, V. & Durand, D. How Random are Intrinsically Disordered Proteins? A Small Angle Scattering Perspective. *Curr. Protein Pept. Sci.* **13**, 55–75 (2012).
125. Quan, B. D. & Sone, E. D. Cryo-TEM Analysis of Collagen Fibrillar Structure. in *Methods in Enzymology* vol. 532 189–205 (Elsevier Inc., 2013).
126. Yip, K. M., Fischer, N., Paknia, E., Chari, A. & Stark, H. Atomic-resolution protein structure determination by cryo-EM. *Nature* **587**, 157–161 (2020).
127. Koifman, N., Biran, I., Aharon, A., Brenner, B. & Talmon, Y. A direct-imaging cryo-EM study of shedding extracellular vesicles from leukemic monocytes. *J. Struct. Biol.* **198**, 177–185 (2017).
128. Contreras-Cáceres, R. *et al.* Effect of the Cross-Linking Density on the Thermoresponsive Behavior of Hollow PNIPAM Microgels. *Langmuir* **31**, 1142–1149 (2015).
129. Gelissen, A. P. H. *et al.* 3D Structures of Responsive Nanocompartmentalized

Microgels. *Nano Lett.* **16**, 7295–7301 (2016).
130. Nickel, A. C. *et al.* Anisotropic Hollow Microgels That Can Adapt Their Size, Shape, and Softness. *Nano Lett.* **19**, 8161–8170 (2019).
131. Zheng, Y. *et al.* Directly Resolved Core-Corona Structure of Block Copolymer Micelles by Cryo-Transmission Electron Microscopy. *J. Phys. Chem. B* **103**, 10331–10334 (1999).
132. Shimoni, K. & Danino, D. Imperfect Dissolution in Nonionic Block Copolymer and Surfactant Mixtures. *Langmuir* **25**, 2736–2742 (2009).
133. Kochovski, Z., Chen, G., Yuan, J. & Lu, Y. Cryo-Electron microscopy for the study of self-assembled poly(ionic liquid) nanoparticles and protein supramolecular structures. *Colloid Polym. Sci.* **298**, 707–717 (2020).
134. Egerton, R. F. *Physical Principles of Electron Microscopy*. (Springer International Publishing, 2016). doi:10.1007/978-3-319-39877-8.
135. Ling, Q. D. *et al.* Polymer memories: Bistable electrical switching and device performance. *Polymer* (2007) doi:10.1016/j.polymer.2007.06.025.
136. Cetintas, M. *et al.* Free-standing thermo-responsive nanoporous membranes from high molecular weight PS-PNIPAM block copolymers synthesized via RAFT polymerization. *Polym. Chem.* (2017) doi:10.1039/c7py00023e.
137. Moad, G., Rizzardo, E. & Thang, S. H. Radical addition–fragmentation chemistry in polymer synthesis. *Polymer (Guildf).* **49**, 1079–1131 (2008).
138. Nuopponen, M., Ojala, J. & Tenhu, H. Aggregation behaviour of well defined amphiphilic diblock copolymers with poly(N-isopropylacrylamide) and hydrophobic blocks. *Polymer (Guildf).* **45**, 3643–3650 (2004).
139. Qiu, X.-P. & Winnik, F. M. Facile and Efficient One-Pot Transformation of RAFT Polymer End Groups via a Mild Aminolysis/Michael Addition Sequence. *Macromol. Rapid Commun.* **27**, 1648–1653 (2006).
140. Sanjeevi Prasath, S. *et al.* Optical and rheological studies on weak gel-sol transition in aqueous solutions of poly(N-isopropylacrylamide)-block-polystyrene. *Express Polym. Lett.* **11**, 589–599 (2017).
141. Cao, Z., Ziener, U. & Landfester, K. Synthesis of Narrowly Size-Distributed Thermosensitive Poly(N -isopropylacrylamide) Nanocapsules in Inverse Miniemulsion. *Macromolecules* **43**, 6353–6360 (2010).
142. Glatter, O. A new method for the evaluation of small-angle scattering data. *J. Appl. Crystallogr.* **10**, 415–421 (1977).
143. Encinas, A., Demand, M., Vila, L., Piraux, L. & Huynen, I. Tunable remanent state resonance frequency in arrays of magnetic nanowires. *Appl. Phys. Lett.* **81**, 2032–2034 (2002).
144. Jaafar, M. F. Magnetic hysteresis modeling and numerical simulation for ferromagnetic materials. in *2013 International Conference on Control, Decision and Information Technologies (CoDIT)* 516–523 (IEEE, 2013). doi:10.1109/CoDIT.2013.6689598.
145. Jiles, D. C. & Atherton, D. L. Theory of ferromagnetic hysteresis. *J. Magn. Magn. Mater.* **61**, 48–60 (1986).
146. Pope, R. M. & Fry, E. S. Absorption spectrum (380–700 nm) of pure water II Integrating cavity measurements. *Appl. Opt.* **36**, 8710 (1997).
147. Beć, K. B. & Huck, C. W. Breakthrough Potential in Near-Infrared Spectroscopy: Spectra Simulation. A Review of Recent Developments. *Front. Chem.* **7**, (2019).
148. Engineering ToolBox. Water - Thermal Diffusivity vs. Temperature and Pressure. [online]. (2018).
149. Rubinstein, M. & Colby, R. H. *Polymer physics. Oxford University Press* (2003).

150. Howell, S. T., Grushina, A., Holzner, F. & Brugger, J. Thermal scanning probe lithography—a review. *Microsystems Nanoeng.* **6**, 21 (2020).
151. Hammouda, B. *PROBING NANOSCALE STRUCTURES – THE SANS TOOLBOX*. http://www.ncnr.nist.gov/staff/hammouda/the_SANS_toolbox.pdf (2016).
152. Stieger, M., Pedersen, J. S., Lindner, P. & Richtering, W. Are Thermoresponsive Microgels Model Systems for Concentrated Colloidal Suspensions? A Rheology and Small-Angle Neutron Scattering Study. *Langmuir* **20**, 7283–7292 (2004).
153. Ko, C. H. *et al.* Self-Assembled Micelles from Thermoresponsive Poly(methyl methacrylate)- b-poly(N-isopropylacrylamide) Diblock Copolymers in Aqueous Solution. *Macromolecules* **54**, 384–397 (2021).
154. Hawley, S. A. Reversible pressure-temperature denaturation of chymotrypsinogen. *Biochemistry* **10**, 2436–2442 (1971).
155. Lassalle, M. W., Yamada, H. & Akasaka, K. The pressure-temperature free energy-landscape of staphylococcal nuclease monitored by 1H NMR. *J. Mol. Biol.* **298**, 293–302 (2000).
156. Niebuur, B.-J. *et al.* Formation and Growth of Mesoglobules in Aqueous Poly(N -isopropylacrylamide) Solutions Revealed with Kinetic Small-Angle Neutron Scattering and Fast Pressure Jumps. *ACS Macro Lett.* **7**, 1155–1160 (2018).
157. Kunugi, S., Yamazaki, Y., Takano, K., Tanaka, N. & Akashi, M. Effects of Ionic Additives and Ionic Comonomers on the Temperature and Pressure Responsive Behavior of Thermoresponsive Polymers in Aqueous Solutions. *Langmuir* **15**, 4056–4061 (1999).
158. Shibayama, M., Isono, K., Okabe, S., Karino, T. & Nagao, M. SANS Study on Pressure-Induced Phase Separation of Poly(N -isopropylacrylamide) Aqueous Solutions and Gels. *Macromolecules* **37**, 2909–2918 (2004).
159. Solution, P. N. *et al.* Molecular Motion and ’ H NMR Relaxation of Aqueous. 963–968.
160. Kato, E. Thermodynamic study of a pressure-temperature phase diagram for poly(N-isopropylacrylamide) gels. *J. Appl. Polym. Sci.* **97**, 405–412 (2005).
161. Lin, M. Y. *et al.* Universality in colloid aggregation. *Nature* **339**, 360–362 (1989).
162. Chizhov, I. Ultra-fast and extra-long: a novel laser T-jump apparatus for time-resolved spectroscopy of conformational dynamics of proteins. *Institute for Biophysical Chemistry, Hannover Medical School* https://www.mhh.de/en/bpc/scientific-workgroups/time-resolved-laserspectroscopy/methods.
163. Elton, D. C. Stretched Exponential Relaxation. 1–9 (2018).
164. Wu, Z. W., Kob, W., Wang, W.-H. & Xu, L. Stretched and compressed exponentials in the relaxation dynamics of a metallic glass-forming melt. *Nat. Commun.* **9**, 5334 (2018).
165. Li, Q., Peng, X. & McKenna, G. B. Physical aging and compressed exponential behaviors in a model soft colloidal system. *Soft Matter* **15**, 2336–2347 (2019).
166. Philippe, A.-M. *et al.* Glass transition of soft colloids. *Phys. Rev. E* **97**, 040601 (2018).
167. Ren, S. Z., Shi, W. F., Zhang, W. B. & Sorensen, C. M. Anomalous diffusion in aqueous solutions of gelatin. *Phys. Rev. A* **45**, 2416–2422 (1992).
168. Ebini, R. H. & Sorensen, C. M. Light scattering studies of the sol-to-gel transition in particulate systems. *J. Colloid Interface Sci.* **556**, 577–583 (2019).
169. Sandkühler, P., Sefcik, J. & Morbidelli, M. Scaling of the Kinetics of Slow Aggregation and Gel Formation for a Fluorinated Polymer Colloid. *Langmuir* **21**, 2062–2077 (2005).

Bibliography:

170. Liao, W., Zhang, Y., Guan, Y. & Zhu, X. X. Gelation Kinetics of Thermosensitive PNIPAM Microgel Dispersions. *Macromol. Chem. Phys.* **212**, 2052–2060 (2011).
171. Johansson, A., Kollman, P., Rothenberg, S. & McKelvey, J. Hydrogen bonding ability of the amide group. *J. Am. Chem. Soc.* **96**, 3794–3800 (1974).
172. Schneider, C. A., Rasband, W. S. & Eliceiri, K. W. NIH Image to ImageJ: 25 years of image analysis. *Nat. Methods* **9**, 671–675 (2012).
173. Perrier, S. 50th Anniversary Perspective : RAFT Polymerization—A User Guide. *Macromolecules* **50**, 7433–7447 (2017).
174. Moad, G., Rizzardo, E. & Thang, S. H. Radical Addition–Fragmentation Chemistry and RAFT Polymerization. in *Polymer Science: A Comprehensive Reference* 181–226 (Elsevier, 2012). doi:10.1016/B978-0-444-53349-4.00066-2.
175. Berne, B. J. & Pecora, R. *Dynamic light scattering: with applications to chemistry, biology, and physics.* (Dover Publications, INC., 2000).
176. Stetefeld, J., McKenna, S. A. & Patel, T. R. Dynamic light scattering: a practical guide and applications in biomedical sciences. *Biophys. Rev.* **8**, 409–427 (2016).
177. Feoktystov, A. V. *et al.* KWS-1 high-resolution small-angle neutron scattering instrument at JCNS: current state. *J. Appl. Crystallogr.* **48**, 61–70 (2015).
178. Pipich, V. QtiSAS: user-friendly program for reduction, visualization, analysis and fit of SA(N)S data. https://www.qtisas.com (2020).
179. Biehl, R. Jscatter, a program for evaluation and analysis of experimental data. *PLoS One* **14**, e0218789 (2019).
180. Lindner, P. & Schweins, R. The D11 Small-Angle Scattering Instrument: A New Benchmark for SANS. *Neutron News* **21**, 15–18 (2010).
181. Liquid Pressure Cell 21PL30AO2. https://www.ill.eu/users/support-labs-infrastructure/sample-environment/equipment/high-pressures/liquid-pressure-cells/liquid-pressure-cell-21pl30ao2 (2021).

Bibliography:

Acknowledgements

I would like to thank all those who supported and helped me successfully finish my PhD.

Prof. Dr. Stephan Förster for the opportunity to work at JCNS on an interesting and challenging topic. For the support, discussions, and a lot of suggestions during my time in Forschungszentrum Jülich. I am very grateful for the trust and showing how to be a good scientist.

I want to thank Prof. Dr. Joachim Mayer for the co-supervision of this thesis.

Dr. Jürgen Allgaier for help with the polymer synthesis and characterization. Marlies Hintzen and Dr. Lutz Willner for SEC measurements and evaluations.

I am very grateful to Dr. Martin Dulle for the introduction to the small-angle scattering and helping during my experiments and with any programming problems.

Dr. Beate Förster for an introduction to electron microscopy and for guiding and assisting me in the experiments that were performed for the project. I learned a lot, thank you very much.

I am thankful to Dr. Stephan Hauschild for help with fast temperature jump lasers experiments, scientific discussions, and measurements performing.

I want to also thank Dr. Igor Chizhov from Medizinische Hochschule Hannover for introducing and helping perform the measurements with time-resolved laser spectroscopy.

For support during the SANS beamtimes, many thanks to the team from MLZ Garching: Dr. Henrich Frielinghaus and Dr. Vitaliy Pipich, and from ILL Grenoble: Leonardo Chiappisi. In addition, the people who helped me during measurements: Prof. Dr. Christina Papadakis, Dr. Martin Dulle, Pablo Alvarez Herrera, Feifei Zheng, Johannes Allwang.

I would like to say many thanks for the great working time as well as outside of the work to my colleauges from JCNS-1 and JCNS-2 groups, especially to Dr. Annika Stellhorn, Dr. Tanvi Bhatnagar-Schöffmann, Dr. Patrick Schöffmann, Mathias Strothmann, Bharti Parashar, Dr. Paul Zakalek, Dr. Lisa Fruhner, Dr. Santanu Maiti, Dr. Lingsam Tea, Ekaterina Kostyurina, Ekaterina Buvalaia, Igor Graf von Westarp, Vladislava Fokina and Luman Haris.

Finally, I would like to thank my closest family for their support and patience. To my parents and brother for emotional support, especially during stressful times. Additionally, the special thanks I would like to address to my husband for his understanding and help at the writing time. Thank you very much.

Project was funded by the German Research Foundation (DFG, Deutsche Forschungsgemeinschaft) within Collaborative Research Centre SFB 985 “Functional Microgels and Microgel Systems” (subproject B9).









Curriculum Vitae

Personal Data

Name	Joanna Michalska-Walkowiak
Date of Birth	20.06.1991
Place of Birth	Sieradz, Poland

Education

2017-2022	PhD Physical Chemistry Jülich Centre for Neutron Science (JCNS-1/IBI-8) Forschungszentrum Jülich, and RWTH Aachen University, Germany
2014-2015	M.Sc. Eng. Chemistry of organic compounds and polymer Wroclaw University of Technology, Wrocław, Poland
2010-2014	B.Sc. Eng. Chemistry Wroclaw University of Technology, Wrocław, Poland
2007-2010	High School No. 1 in Sieradz, Poland

Declaration of Authorship

I, Joanna Michalska-Walkowiak declare that this thesis and the work presented in it are my own and has been generated by me as the result of my own original research.

I do solemnly swear that:

1. This work was done wholly or mainly while in candidature for the doctoral degree at this faculty and university.

2. Where any part of this thesis has previously been submitted for a degree or any other qualification at this university or any other institution, this has been clearly stated.

3. Where I have consulted the published work of others or myself, this is always clearly attributed.

4. Where I have quoted from the work of others or myself, the source is always given. This thesis is entirely my own work, with the exception of such quotations.

5. I have acknowledged all major sources of assistance.

6. Where the thesis is based on work done by myself jointly with others, I have made clear exactly what was done by others and what I have contributed myself.

7. None of this work has been published before submission, or parts of this work have been published before as: Michalska-Walkowiak, J., Förster, B., Hauschild, S. & Förster, S. *Bistability, Remanence, Read/write-memory and Logic Gate Function via A Stimuli Responsive Polymer*. Adv. Mater. 2108833 (**2022**).

Date Signature